Copyright © 2005, by the author(s).
All rights reserved.

Permission to make digital or hard copies of all or part of this work for personal or classroom use is granted without fee provided that copies are not made or distributed for profit or commercial advantage and that copies bear this notice and the full citation on the first page. To copy otherwise, to republish, to post on servers or to redistribute to lists, requires prior specific permission.

APPLYING DROP-ON-DEMAND INKJET PRINTING METHOD TO MASKLESS LITHOGRAPHY

by

Yan Wang

Memorandum No. UCB/ERL M05/17

18 May 2005

APPLYING DROP-ON-DEMAND INKJET PRINTING METHOD TO MASKLESS LITHOGRAPHY

by

Yan Wang

Memorandum No. UCB/ERL M05/17

18 May 2005

ELECTRONICS RESEARCH LABORATORY

College of Engineering
University of California, Berkeley
94720

Applying Drop-On-Demand Inkjet Printing Method to Maskless Lithography

by

Yan Wang

B.S. (Beijing University, Beijing, China) 1997

A dissertation submitted in partial satisfaction of the requirements
for the degree of

Doctor of Philosophy

in

Engineering — Electrical Engineering and Computer Sciences

in the

GRADUATE DIVISION

of the

UNIVERSITY of CALIFORNIA at BERKELEY

Committee in charge:
Professor Jeffrey Bokor, Chair
Professor William G. Oldham
Professor Liwei Lin

Spring 2005

The dissertation of Yan Wang is approved:

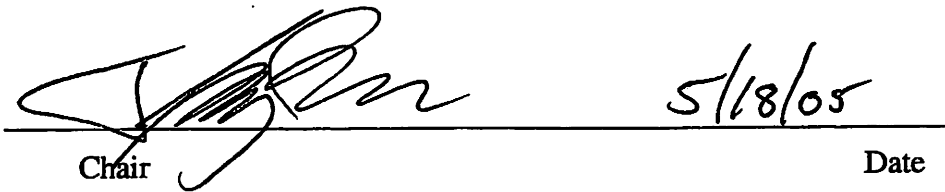

Chair Date

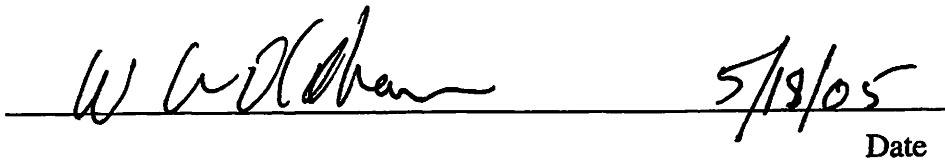

Date

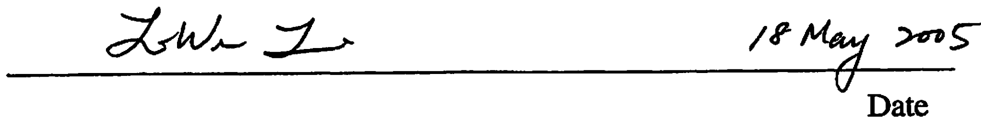

Date

University of California at Berkeley

Spring 2005

Applying Drop-On-Demand Inkjet Printing Method to Maskless Lithography

Copyright © 2005

by

Yan Wang

All rights reserved

Abstract

Applying Drop-On-Demand Inkjet Printing Method to Maskless Lithography

By

Yan Wang

Doctor of Philosophy in Engineering, Electrical Engineering and Computer Sciences

University of California at Berkeley

Professor Jeffrey Bokor, Chair

Writing patterns directly on a substrate with liquid droplets generated by Drop-On-Demand (DOD) inkjet devices on a print head provides a maskless, non-contact, low temperature, flexible, and data driven patterning approach. All current ink-jet printing systems are designed specifically for commercial printers and have relatively large droplets and limited numbers of inkjet devices. Therefore, this research focused on building a monolithic inkjet printhead with high resolution and high throughput for maskless lithography applications.

In this thesis, we will first present our theoretical study of the droplet generation conditions on the micron to sub-micron scale. We found that the required actuation pressure increases almost to an inverse proportion to the targeted droplet radius. Using thinner inkjet nozzles, liquids with lower surface tension, and appropriate pressure pulse shapes could make the droplet generation process easier.

Based on our theoretical study and thermal bubble inkjet printing technology, we have

designed an inkjet printhead with micron scale droplet resolution. The print head also has the advantages of high operation frequency, small device area, high droplet generation stability, low energy consumption, as well as robust structure.

We have also developed two processes, based on silicon micro-machining technology, to fabricate the designed inkjet print head, including a wafer-wafer bonding process and an original Ge sacrificial structure etching process. The second process is more mature and is capable of forming monolithic print heads with large arrays of inkjet devices and high yield.

The test chips have been observed to generate droplets as small as 2.8μm using a high resolution video imaging system. These droplets are 5 times smaller than those produced by typical inkjet cartridges. We also found that the droplet generation process is stable, with a small droplet trajectory distribution at short droplet flying distance; the micron scale device also has a large operation window for single droplet formation.

Suspensions of gold nano-particles have been used as printing materials for our inkjet device. We have printed Au lines as small as 8μm, the smallest features that have ever been reported by inkjet printing fabrication methods. Installing our printhead into an automatic patterning system allows us to investigate many pattern-formation related issues. Our printhead can also use aqueous nanotube suspensions to realize direct deposition of carbon nano-tubes.

The print head technology developed in our research can then form the basis of a high-throughput maskless lithography system for building micro scale electronic circuits and MEMS devices. In addition, we propose using thin film PZT material and d_{33} mode

actuator to build a piezoelectric inkjet print head, as well as utilizing liquid droplet evaporation to further reduce the droplet size, allowing sub-micron to even deep-submicron scale pattering applications.

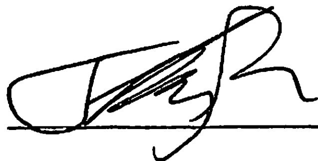

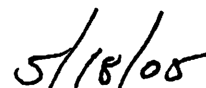

Professor Jeffrey Bokor, Chair　　　　Date

To my family

TABLE OF CONTENTS

1. INTRODUCTION 1

1.1 Motivation 1

1.2 Inkjet printing background 3

1.3 The idea of performing maskless lithography using drop-on-demand inkjet printing method 5

1.4 Challenges in building an inkjet printing maskless lithography system 7

1.5 Thesis content layout 10

Reference 11

2. THEORETICAL BACKGROUND 13

2.1 Droplet formation process of DOD inkjet devices 13

2.2 Droplet generation conditions of DOD inkjet devices 14

2.2.1 Scaling analysis 15

2.2.2 Numerical simulation results 19

2.2.2.1 Droplet generation conditions 20

2.2.2.1 Influence of the pressure profile, nozzle shape and fluid properties 24

Reference 29

3. PRINT HEAD DESIGN 30

3.1 Actuation mechanism 30

3.1.1 DOD inkjet device comparison 30

3.1.2 Thermal bubble Inkjet operation mechanism 31

3.1.3 Pressure characteristic and droplet size limit 33

3.2 Design of thermal bubble inkjet print head for maskless lithography purpose: 37

3.2.1 The design issues 37

3.2.2 The overall print head structure 38

3.2.3 The device structure 39

3.2.4 Heater design 40

3.2.4.1: Heater structure 40

3.2.4.2: One-dimensional heater operation simulation results 42
3.2.5 Nozzle design 47
3.2.6 Refilling channel design 49
3.2.7 Design of the inkjet chambers 53
3.3 Summary 55
Reference 56

4. PRINT HEAD FABRICATION 58
4.1 Wafer-wafer bonding processes 59
4.2 Ge sacrificial structure process 65
4.2.1 Detailed process flow of the single wafer print head fabrication process 67
4.2.2 Test chip structure 81
4.3.2 Focused Ion Beam drilled nozzles 86
4.3.3 Advantages of the Ge sacrificial etching process 87
Reference 88

5. EXPERIMENTAL REULTS OF BUBBLE FORMATION AND DROPLET GENERATION 91
5.1 Experimental system 91
5. 2 Bubble formation results 93
5.2.1 Influence of heating signal on bubble formation 94
5.2.2 Bubble formation in different materials 97
5.3 Droplet generation results 98
5.3.1 Minimum droplet dimensions 99
5.3.2 Influence of heating signal and heater size 103
5.3.3 Droplet velocity change and trajectory distribution 106
5.3.4 Droplet volume change 109
5.3.5 Frequency and power analysis 111
Reference 113

6. TEST PRINTING OF NANO-PARTICLE BASED MATERIALS AND CARBON NANOTUBES 114
6.1 Material requirements 114

6.2 Inkjet printing of suspensions of Au nano-particles 115
6.2.1 Droplet generation 115
6.2.2 Inkjet printed Au dots and lines 117
6.2.21 Inkjet printed Au dots 117
6.2.2.2 Inkjet printed Au lines 120
6.2.3 Printing arbitrary patterns using an automatic printing system 122
6.3 Direct deposition of carbon nano-tubes on pre-patterned electrodes 128
Reference 131

7. CONCLUSION 134
7.1 Summary 134
7.2 Future research directions 136
7.2.1 Further reducing droplet size 136
7.2.2: Building a piezoelectric actuation system 136
7.2.3: Utilize liquid evaporation 142
Reference 145

TABLE OF FIGURES

Chapter I

Figure 1.1: Schematic of an optical lithography system and the pattern transfer steps of current micro-fabrication process 2
Figure 1.2: Continuous and drop-on-demand mode inkjet device 4
Figure 1.3: Schematic diagram of an inkjet printing maskless lithography system 6
Figure 1.4: Illustration of pattern formation with droplets 7

Chapter II

Figure 2.1: Droplet formation sequence of a DOD inkjet device 14
Figure 2.2: Input pressure profile and the liquid meniscus shape at the end of liquid acceleration 16
Figure 2.3: Relative strength of the liquid viscosity over surface tension vs. nozzle diameter 18
Figure 2.4: Input pressure profile and the device shape for the numerical simulation 21
Figure 2.5: Simulated droplet generation sequences through a 400nm nozzle 22
Figure 2.6: Pressure and velocity distribution during droplet formation process 23
Figure 2.7: Droplet formation sequence with different pressure shape 25
Figure 2.8: Pressure distribution for nozzle with different shape and thickness. 26
Figure 2.9: Required actuation pressure vs. nozzle thickness 26
Figure 2.10: Pressure magnitude for generating a liquid droplet through a 200nm nozzle with different aspect ratios 27

Figure 2.11: Actuation pressure vs. liquid surface tension 28

Chapter III

Figure 3.1: The operation cycle of a thermal bubble inkjet device. 32

Figure 3.2: Bubble pressure profile of a thermal bubble inkjet device 34

Figure 3.3: Simulated droplet generation result for thermal bubble inkjet device 35

Figure 3.4: Simulated droplet generation result for 0.2μm nozzle 36

Figure 3.5: Schematic structure of inkjet print head designed for maskless lithography system 39

Figure 3.6: Thermal bubble inkjet device structures 40

Figure 3.7: Schematic diagram of our top-shooting thermal bubble inkjet device 40

Figure 3.8: Heater structure of a thermal bubble inkjet device 41

Figure 3.9: Temperature distribution in heater stack with different input signal 44

Figure 3.10: Heating voltage, heater temperature, fluid energy and the heating efficiency vs. the heating pulse width. 45

Figure 3.11: Heater cooling time and heating energy vs. heat barrier thickness. 45

Figure 3.12: Driving voltage and heater temperature vs. passivation thickness 46

Figure 3.13: Influence of un-balanced wetting or irregular nozzle shape on droplet generation stability 47

Figure 3.14: Schematic of the well-shaped nozzle in our print head 49

Figure 3.15: Schematic of laminar liquid flow during droplet ejection and chamber refilling stage 51

Figure 3.16: Required minimum channel length vs. the nozzle diameter 52

Figure 3.17: Inkjet refilling and meniscus damping behavior 53

Chapter IV

Figure 4.1: The process flow for print head fabrication using wafer bonding method 61

Figure 4.2: Final print head structure using the wafer bonding method 61

Figure 4.3: The epoxy stamping bonding method 63

Figure 4.4: Ni-Si eutectic bonding result 64

Figure 4.5: SEM pictures of print head formed by Ni-Si eutectic bonding method 64

Figure 4.6: Layout of a single inkjet device using Ge sacrificial etching process 66

Figure 4.7: Process flow of heater formation 67

Figure 4.8: Lift-off result of Pt heater and Cu interconnect lines. 70

Figure 4.9: Process flow of Ge sacrificial structure formation 71

Figure 4.10: Top view of Ge sacrifical structure 71

Figure 4.11: Process flow of inkjet chamber, nozzle and feeding holes formation 74

Figure 4.12: DRIE etched through wafer feeding holes 78

Figure 4.13: Process flow of opening inkjet chamber, refilling hole, bonding pads and nozzle membranes 78

Figure 4.14: Ge sacrificial etching result 80

Figure 4.15: Inkjet nozzles opened by plasma etching method 81

Figure 4.16: Test chip layout of the GE sacrificial etching process 82

Figure 4.17: Array of inkjet structures on a test chip 83

Figure 4.18: SEM picture of a single inkjet device with 4μm nozzle 83

Figure 4.19: The handling chip fabrication process 85

Figure 4.20: Schematic and micrographic image of the final test chip structure with plastic tubing and ceramic package 85

Figure 4.21: 1μm scale nozzle opened by photo resist reflow and plasma etching method 86

Figure 4.22: Focused ion beam drilled nozzle 87

Chapter V

Figure 5.1: Experimental system for observing bubble formation and droplet generation process 92

Figure 5.2: Optical setup in the experimental system 93

Figure 5.3: Bubble nucleation, growth and collapse sequence 94

Figure 5.4: Micrographic image of a broken heater 96

Figure 5.6: Reference length mark on the test chip surface 100

Figure 5.7: Single droplets formation sequence from a 7μm nozzle 101

Figure 5.8: Single droplets formation from a 2.5μm nozzle 101

Figure 5.9: A 2.8μm single water droplet generated from 1.5μm nozzle 103

Figure 5.10: Satellite droplet formation from a sub-2μm nozzles 104

Figure 5.11: Influence of driving electric signal on droplet generation with 10μm nozzle 104

Figure 5.12: Single droplet generation window for different nozzle size 106

Figure 5.13: Trajectory distribution of 3.5μm droplets 109

Chapter VI

Figure 6.1: Au nano-particle material and droplet generation 116

Figure 6.2: Au particle accumulation on the heater surface 117

Figure 6.3: AFM image of a donut shaped Au dot printed on oxide surface 118

Figure 6.4: Effect of substrate heating on printed dot size and shape 120

Figure 6.5: Droplet footprint vs. liquid contact angle.. 120

Figure 6.6: AFM image and cross section of an 8μm Au line 121

Figure 6.7: Au line printed with different operation conditions 122

Figure 6.8: The automatic patterning system set up 123

Figure 6.9: Lines and pads array printed with the automatic patterning system 125

Figure 6.10: Dots array formed with large droplet distances.. 125

Figure 6.11: Inkjet printed resistance measurement patterns.. 127

Figure 6.12: Oxide line etched using the inkjet printed pattern as mask 127

Figure 6.13: SEM pictures of Carbon nanotubes deposited by inkjet printing............... 130

Figure 6.14: Possible nanotube alignment using inkjet printing deposition combined with alternating current dielectrophoresis method 131

Chapter VII

Figure 7.1: Schematics of a bimorph piezoelectric actuator 139

Figure 7.2: The simulated volume displacement and pressure pulse shape of a PZT bi-membrane actuator 140

Figure 7.3: Schematics of a d_{33} mode piezoelectric actuator 140

Figure 7.4: The simulated volume displacement and pressure pulse shape of a PZT d33 actuator 142

Figure 7.5: Water vapor density vs. ambient temperature 143

TABLE OF TABLES

Table 1.1: Main features of the most advanced inkjet print head 9

Table 1.2: Required number of inkjet devices on a print head...................................... 9

Table 2.1 Summary of scaling analysis.. 19

Table 2.2 Summary of inkjet numerical simulation.. 24

Table 5.1: Bubble formation voltage vs. heater dimension and heating pulse width.... 95

Table 5.2: Observed heater breaking and bubble formation voltage vs. heating pulse width.. 96

Table 5.3: Calculated bubble nucleation temperature for different organic solvents ... 97

Table 5.4: Fluid properties of typical organic solvents at superheat temperature......... 98

Table 5.5: Observed minimum droplet size vs. nozzle diameter 100

Table 5.6: Calculated droplet flying distance and time vs. droplet size...................... 109

Table 5.7: Calculated water droplet lifetime vs. droplet diameter 111

Table 7.1: Comparison of the relative evaporation rate of organic solvents and water 143

ACKNOWLEDGEMENTS

I would like to express my deepest gratitude to my research advisor, Professor Jeffery Bokor, for his guidance and supervision. This thesis would have never been written without his support and encouragement. Furthermore, his way of solving complicated problems and hands-on approaches for research will have a lasting impact on my career in the future.

I would also like to thank Professor William Oldham and Professor Liwei Lin for serving on my thesis and qualifying exam committee. They have provided constructive comments during my qualifying exam, which directly influenced the writing of this thesis. I am also grateful to Professor Vivek Subramanian and Professor Andy Neureuther for their suggestions and support on my research. Thanks to Professor Roger Howe for being in my qualifying exam committee.

I had the privilege of working with exceptional colleagues in the department, including Michael Shumway, Yashesh Shroff, Yijian Chen, Peiqi Xuan, Mast Last, Xiying Shong, Yu-chin Tseng, Arthur Lee, and many others... They have all given me great help in the development of my research project. They are also my friends and made my grad school experience colorful and memorable. Special thanks go to Steven Molesa, who helped me in synthesizing the testing material and implementation of our print head into an automatic patterning system. He is a great partner to work with. Many thanks to the staffs and members of the Berkeley Microelectronics Laboratory, Katalin Voros, Bob Hamilton, Mathew Wasilik, Xiaofan Meng, Jimmy Chang, Kim Chan, Yang Zhao, Peter Huang, without them, we could not have developed a mature device fabrication process.

Many people outside the department have also helped a great deal with my research. Among them, Santipan Maity assisted our CoventorWare numerical inkjet simulations. Dr. Thomas Shenkel in LBL has trained me to fabricate small inkjet nozzles using a Focused Ion Beam system. Yi Cui from Material Science department was always helpful for me to understand better of the nano-particle materials. Dr. Alec Talin Xu from Sandia National Lab was very generous, providing us with nanotube suspensions. Locus Tsakalakosa helped us to develop a piezoelectric thin film device in the early research stage. Tyler Sims from ORNL provided many valuable suggestions in inkjet design.

Lastly, but most important, I thank my family--my husband Gang Zhou, my mother Fenlan Song and my father Jingzhang Li. I am extremely grateful for Gang's support over the past years. He brings me happiness and makes my life fruitful. My parents always believe in me and have done all they can to support my choices.

This research is jointly funded by DARPA grant MDA972-97-1-0010 and SRC contract 96-LC-460.

CHAPTER I

INTRODUCTION

1.1 Motivation

Today, microfabrication is widely used to manufacture integrated circuits (ICs), MEMS and optical devices for computation, communication, sensor, and actuator applications. Microfabrication relies on optical lithography to print desired features from a mask to a silicon substrate [1]. The schematic of an optical lithography system is shown in Figure 1.1. In such a system, light shines through a mask with open and opaque regions, passes through a set of refractive lens, and projects onto a wafer surface coated with a photosensitive resist. The minimum feature size that can be printed on the wafer is limited by the wavelength and the Numerical Aperture (NA) of the optical projection system and is in the deep submicron to tens of nano-meter range in current technology node [2].

However, optical lithography is an expensive and time consuming process, especially in the semiconductor industry, where transistor size is continuously scaled down for cheaper and faster chips. To print sub-wavelength features, the optics must be precisely machined, in order to achieve high NA, large field, aberration-free patterning capabilities, while the masks are written with electron beam system, and become increasingly expensive with large amounts of data and the introduction of resolution

enhancement techniques such as optical proximity correction (OPC) and phase shifting masks (PSM). Currently, optical lithography commands more than 30% of total IC fabrication expenses. Even for fabricating MEMS and optical devices, which have relatively large features, the huge tool costs and long mask preparation times are rapidly becoming barriers to technology innovation.

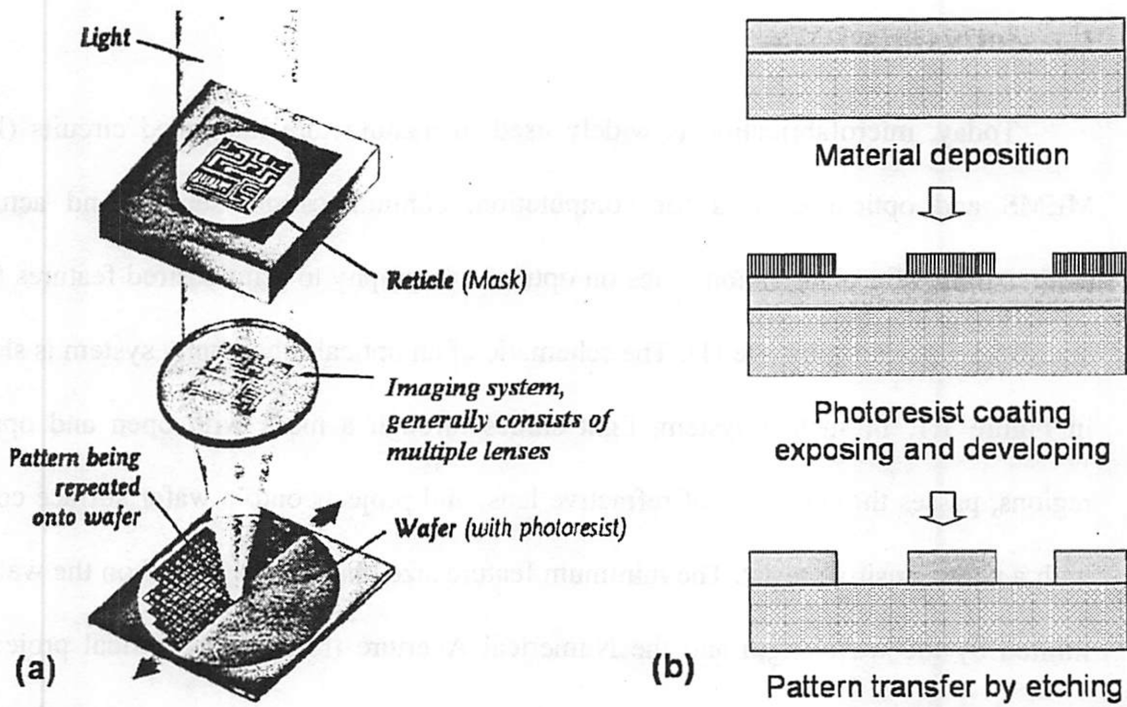

Figure 1.1: (a) Schematic of an optical lithography system [1]. (b) The pattern transfer steps of current microfabrication process

Moreover, the current process flow to build a transistor circuit on a wafer is subtractive in nature. Firstly, the material layer is deposited from precursors onto a substrate in a high temperature, high vacuum furnace (or using a sputtering system) in an ultra-clean environment. Then, a photoresist layer is spin-coated onto the wafer and optically exposed. After the photoresist is developed and the unexposed part is removed,

the left over resist is used as a mask to transfer the printed circuit patterns to a beneath material layer by dry or wet etching. These steps are repeated many times (more than 30 masks are used for current IC technology) until a 3-dimensional circuit structure is built up. With this process, most of deposited material and all the photoresist are actually wasted, which not only increases the cost of the final chips but also has a big impact in the environment, due to the huge amount of the energy consumed and the toxic byproducts of the material deposition process.

Developing an additive lithography system capable of building the device layers from the layouts without using masks and optics would avoid all the above issues. Ink-jet printing technology, which has enjoyed great success in today's paper document printing market, could be a good candidate for such a task, due to its low cost and high flexibility [3, 4]. Implementation of the inkjet printing technology in maskless lithography applications is then the main focus of this research.

1.2 Inkjet printing background

In an inkjet printer, a series of small apertures made on a print head eject ink droplets to a specified position on a piece of paper, forming an image. Many of today's inkjet ideas and systems were invented, developed, and produced commercially in the 1970s and 1980s. The inkjet devices on a print head have been implemented in many different designs. The earliest developed inkjet printers were continuous-mode [5]. In such inkjet devices, fluid is pressurized through an orifice to form a liquid jet. Surface tension acts to amplify the disturbance of a high frequency transducer down the stream, causing the jet to break up into uniform drops. An electrostatic field is applied to charge the droplets which are deflected to their desired printing location by another field, as

shown in Figure 1.2(a). This type of inkjet printing system is referred to as "continuous" because drops are continuously produced.

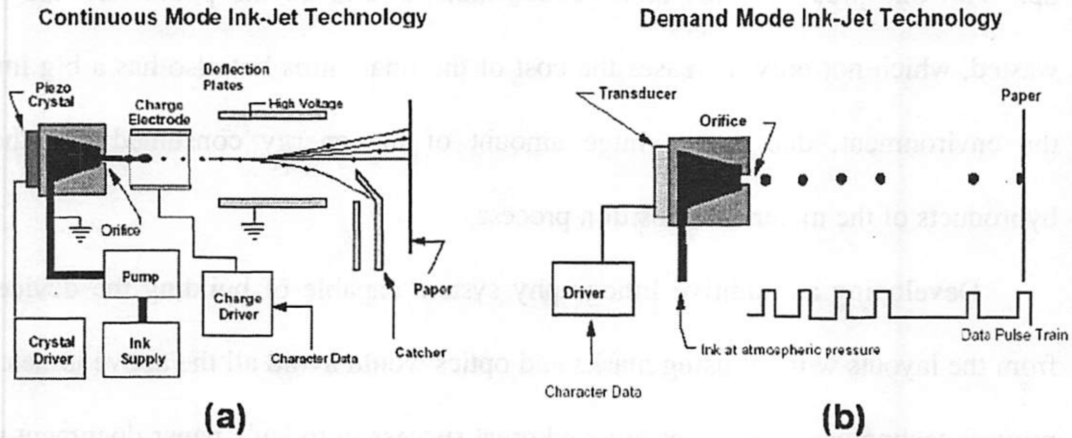

Figure 1.2: (a) Continuous mode inkjet device. (b) Drop-on-demand mode inkjet device [6]

Even though the continuous inkjet device operates at high frequencies and consumes little energy, the droplet deflection system is huge and the printed fluid requires re-collection. Therefore, today's inkjet printers more commonly use drop-on-demand (DOD) inkjet devices, which produce droplets only when required. In a drop-on-demand inkjet device, a transducer changes the volume of ink in a pressure chamber when an electric pulse is applied. This generates a pressure wave that propagates to a nozzle, forcing out an ink droplet [7], as illustrated in Figure 1.2(b). The droplet must be formed with sufficient pressure to expel the droplet toward a recording media. The mechanisms used in the droplet formation process can be categorized into four major types: thermal, piezoelectric, electrostatic, and acoustic. Most, if not all, of the drop-on-demand inkjet printers on the market today use either the thermal or piezoelectric principles. Both the electrostatic inkjet and acoustic inkjet methods are not mature and are

only available in a few commercial products. We will discuss the different DOD inkjet devices in detail in chapter III.

1.3 The idea of performing maskless lithography using drop-on-demand inkjet printing method

Applying drop-on-demand inkjet technology from paper document printing to electronic and mechanical device patterning is quite straightforward. The schematic of a proposed inkjet printing maskless lithography system (abbreviated as IPMLS from now on) is shown in Figure 1.3. Like an inkjet printer, the system consists primarily of a print head with integrated controlling circuits and a large array of DOD inkjet devices. A motion control system moves a stage-mounted wafer beneath the print head with fine steps (in horizontal directions). A circuit layout can be coded in a computer and then sent to the print head as electrical pulses. When a DOD inkjet device receives a signal, it expels a small fluid droplet of certain material toward the wafer. Aligned by the movement of the stage, the droplets land on the desired locations on the substrate as pixels. The adjacent droplets merge and the solvent dries to form arbitrarily shaped material patterns, as illustrated in Figure 1.4. The printed materials could be solvents, particulate suspensions, or polymers, any of which could possess physical properties allowing either the direct formation of device layers or the formation of reliable mask layers for pattern transfer processes.

Besides saving the cost of optics, masks and materials, the DOD IPMLS also has many other advantages as a patterning tool. Firstly, as a data driven process, the inkjet printing system could directly transfer CAD designs into device patterns, which would save the process development time and accommodate customization. Secondly, the

pattern quality is no longer limited by the depth of focus of the optics; since droplets can travel relatively long distances without significant trajectory change, patterning on non-planar surfaces, small objects or even deep trenches becomes possible. Thirdly, as a low temperature additive process, micro-fabrication could also be performed on non-traditional substrates such as paper or plastics, which is especially attractive for building low cost circuits for flat panel displays, identification tags and other disposable electronic devices. Lastly, inkjet printing lithography could handle a wide range of materials, including solution-based materials like organo-metallics, organo-semiconductors, polymers, suspended nano-particles, and exposure- or etching- sensitive materials [8]. Combined with the traditional silicon based materials, many original devices could then be fabricated.

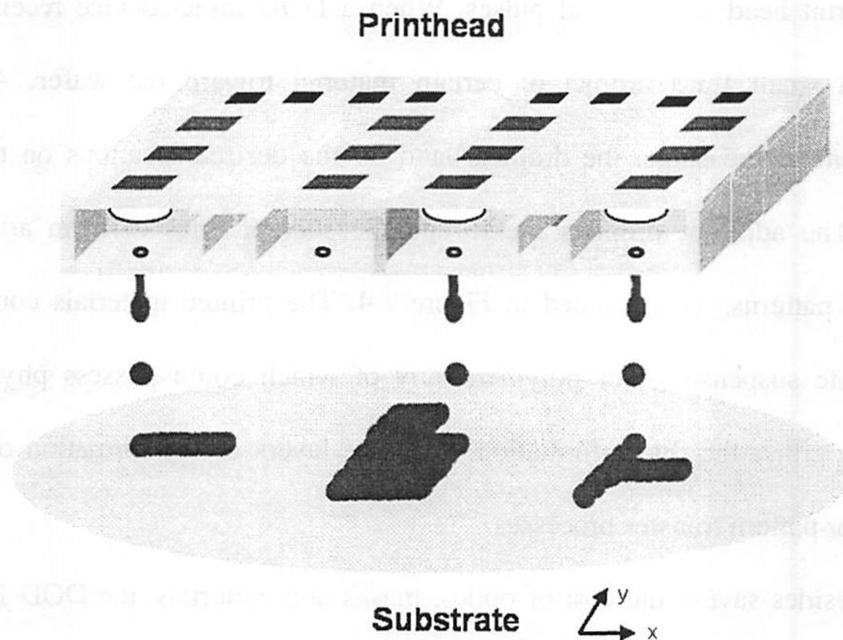

Figure 1.3: Schematic diagram of an inkjet printing maskless lithography system

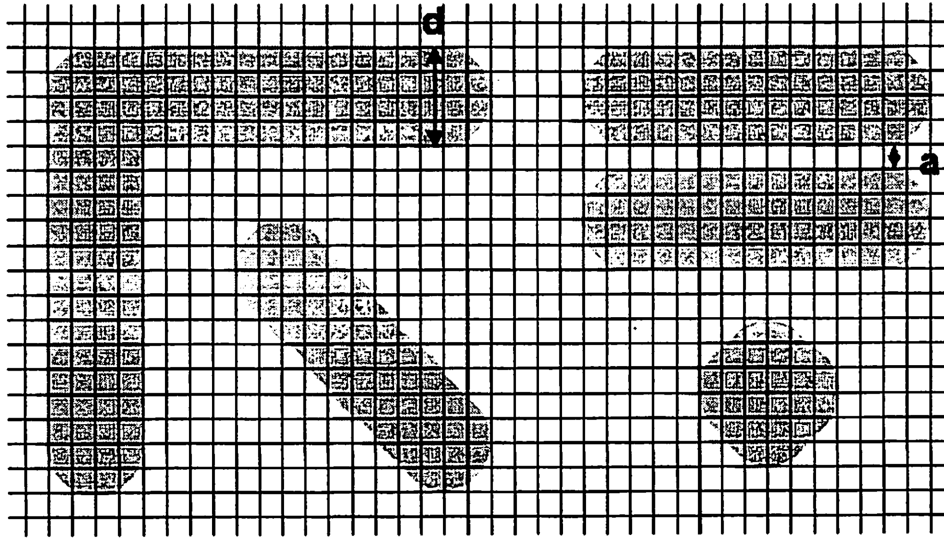

Figure 1.4: Illustration of pattern formation with material drops printed from IPMLS. The pixel size is one quarter of the footprints of the droplets.

1.4 Challenges in building an inkjet printing maskless lithography system

Because of its unique advantages, many research groups have already used direct deposition by inkjet printing methods to fabricate devices such as light emitting diodes [9], micro-lens arrays [6], MEMS [10], etc. Recent years have also seen growing interest in inkjet printing of organic transistor circuits for low cost display applications [11, 12]. A group in Cambridge has reported an organic transistor circuit built from conductive polymer materials [13] using inkjet printing and a selective wetting method. Similar work has also been done by Professor Vivek Subramanian's group at UC Berkeley [14]. However, all these devices are fabricated in research labs using simple, single-device printing setups. Their printed feature resolutions are bigger than 50μm, and the fabrication throughput is low. Applying inkjet printing technology to build a maskless

lithography system for fabrication of large scale electronic or mechanical structures, however, is not an easy task, due to limitations of the available inkjet print head technology.

In an inkjet patterning system, the minimum feature size is determined by the footprint of the smallest droplet that can be generated from the print head, as illustrated in Figure 1.4. The droplet footprint is a typically 1.5-3 times bigger than its original size when it impacts on a solid substrate. (We will discuss more about pattern formation related issues of IPMLS in chapter VI). Even though the inkjet printing industry has been developing DOD inkjet print heads towards smaller droplet sizes and hence higher resolutions, the state-of-the-art inkjet devices for patterning applications, including the most advanced commercial inkjet cartridges, can only deliver liquid droplets larger than 12μm in diameter, as summarized in Table 1.1. This droplet resolution is sufficient for paper document printing applications, but is two orders of magnitude bigger than the feature size required for fabricating semiconductor chips. (IC circuits on semiconductor chips have characteristic feature sizes around 0.4μm in the top metal level, and smaller than 0.1μm for the transistor gate in current technology node). For applications such as patterning low cost organic transistor circuits (typical channel length <5um for high performance devices) or MEMS devices, the droplets produced by current inkjet print heads are still too big and must be reduced.

Moreover, existing inkjet print head fabrication processes limit the number of inkjet devices on a print head to less than several thousands (Table 1.1). Since the patterning throughput is inversely proportional to the square of the droplet diameter, given a fixed number of devices and operation frequency (typically tens of kHz and hard

to increase without sacrificing printing stability), decreasing droplet sizes require much larger device arrays to provide sufficient throughput for large scale devices fabrication. In table 1.2, we list the required number of inkjet devices to pattern an 8 inch wafer in two minutes with inkjet operation frequency of 20kHz, which is the typical throughput requirement in IC industry. As shown in the table, reducing pixel size to 0.1μm would require as many as 200 thousand devices on a print head. Such a large device array would need integrated controlling circuits to increase the data transfer and handling speed. In addition, maskless lithography print heads need good chemical compatibility, to handle different materials, and stable droplet generation, to achieve high patterning quality. All of these impose tremendous challenges on the print head design and fabrication process.

Reference Device	Type	Diameter (Volume)	#Device/Head
HP Desk Jet 9680 [16]	Thermal	15.5μm (2pL)	1280
Canon ip8500, 9900 [16]	Thermal	15.5μm (2pL)	2048
Epson Stylus R800 [16]	Piezoelectric	14μm (1.5pL)	180
Tseng et. al [17]	Thermal	12μm (0.9pL)	Array
J. Chen et. Al [18]	Thermal	20μm (4pL)	16

Table1.1: Main features of the most advanced inkjet print head

Pixel size (μm)	2	0.5	0.2	0.1
Resolution (dpi)	12000	48000	120000	240000
# Inkjet device	6e3	1e5	6e5	2.4e6

Table1.2: Required number of inkjet devices on a print head for patterning an 8 inch wafer in two minutes with inkjet operation frequency of 20 kHz

1.5 Thesis content layout

The next chapter presents our research work in investigating the conditions for generating micron to sub-micron scale droplets from a DOD inkjet device. The results are based both on scaling analysis and numerical simulation through commercial computational fluid dynamics software.

Based on our theoretical study, we have designed a thermal bubble inkjet print head for high-resolution, high-throughput maskless lithography applications, which will be discussed in Chapter III. First, we will lay out the background of thermal bubble inkjet operation, as well as its advantages over other inkjet actuation mechanisms. Detailed design considerations then follow.

Chapter IV presents the two micro-machining processes we have developed to fabricate the thermal bubble inkjet print head designed in chapter III, including a wafer-wafer bonding process and an original Ge sacrificial structure etching process. The Ge sacrificial etching process is capable of forming monolithic inkjet print head with high device density and high yield. The detailed description of the process flow will be given.

In Chapter V, we use a high-resolution video imaging system to observe test chips of our print head and report experimental results of bubble formation and droplet generation. The droplet size limit, the optimum operation window, and the factors that will influence droplet generation stability and printing quality will all be discussed.

Chapter VI briefly discusses results from experiments with possible printing materials. Our thermal bubble inkjet print head can use Au nano-particle suspensions to form micron scale patterns. It can also use aqueous suspensions to deposit carbon nanotubes.

Chapter VII ends the thesis with a conclusion and also outlines future working directions that could further improve the print head resolution, based on the theoretical and experimental work presented in this dissertation.

Reference

1. J. Bokor, A. Neureuther, W. Oldham, "Advanced Lithography for ULSI", *IEEE Circuits and Devices Magazine*, pp.11-15, 1996

2. Semiconductor Industry Association, "International Technology Roadmap for Semiconductors", http://www.itrs.net/Common/2004Update/2004Update.htm

3. H. P. Le, ''Progress and trends in ink-jet printing technology,'' *J. Imaging, Sci. Technol.*, vol. 42, pp.49-53, 1998.

4. Smouse E., "Optimal design of desktop photo printing systems". *Imaging Sci. & Technol.* vol. 42, pp.91-5, 1998.

5. W.T. Pimbley, "Drop formation from a liquid jet: a linear one-dimensional analysis considering as a boundary value problem". *IBM J. Res. Dev.*, Vol. 29, pp.148, 1984

6. P.W. Cooley, D.B. Wallace, B.V. Antohe, "Application of ink-jet printing technology to BioMEMS and micro-fluidic systems," *Proceedings, SPIE Microfluidics and BioMEMS Conference,* vol.4560, pp177-88, 2001.

7. D. B. Bogy and F. E. Talke, "Experimental and theoretical study of wave propagation phenomena in drop-on-demand ink jet devices," *IBM J. Res. Dev.*, vol. 28, no. 3, pp. 314–321, May 1984.

8. Calvert, P, "Inkjet printing for materials and devices", *Chem. Mater.,* vol. 13, pp. 3299–3305, 2001.

Chapter VII ends the thesis with a conclusion and also outlines future working directions that could further improve the print head resolution, based on the theoretical and experimental work presented in this dissertation.

Reference

1. J. Bokor, A. Neureuther, W. Oldham, "Advanced Lithography for ULSI", *IEEE Circuits and Devices Magazine*, pp.11-15, 1996

2. Semiconductor Industry Association, "International Technology Roadmap for Semiconductors", http://www.itrs.net/Common/2004Update/2004Update.htm

3. H. P. Le, ''Progress and trends in ink-jet printing technology,'' *J. Imaging, Sci. Technol.*, vol. 42, pp.49-53, 1998.

4. Smouse E., "Optimal design of desktop photo printing systems". *Imaging Sci. & Technol.* vol. 42, pp.91-5, 1998.

5. W.T. Pimbley, "Drop formation from a liquid jet: a linear one-dimensional analysis considering as a boundary value problem". *IBM J. Res. Dev.*, Vol. 29, pp.148, 1984

6. P.W. Cooley, D.B. Wallace, B.V. Antohe, "Application of ink-jet printing technology to BioMEMS and micro-fluidic systems," *Proceedings, SPIE Microfluidics and BioMEMS Conference,* vol.4560, pp177-88, 2001.

7. D. B. Bogy and F. E. Talke, "Experimental and theoretical study of wave propagation phenomena in drop-on-demand ink jet devices," *IBM J. Res. Dev.*, vol. 28, no. 3, pp. 314–321, May 1984.

8. Calvert, P, "Inkjet printing for materials and devices", *Chem. Mater.,* vol. 13, pp. 3299–3305, 2001.

9. H. Klauk, B. D'Andrade, T. N. Jackson, "All-organic integrated emissive pixels", *in the 57th Annual Device Research Conference Digest, IEEE*, pp.162, 1999.

10. Fuller SB, Wilhelm EJ, Jacobson JM., "Ink-jet printed nanoparticle microelectromechanical systems", *Journal of Microelectromechanan. Sys.*, vol.11, pp.54-60, 2002

11. Samual J. Moore, "Just one world-plastic", *IEEE Spectrum*, pp55-59, 2002

12. Sirringhaus H., Kawase T. etc., "High-resolution inkjet printing of all-polymer transistor circuits", *Science*, vol.290, no.5499, pp.2123-6, 2000.

13. B. K. Crone, A. Dodabalapur, R. Sarpeshkar, R. W. Filas, Y.-Y. Lin, and Z. Bao, "Design and fabrication of organic complementary circuits", *J. Appl. Phys.*, vol.89, pp.5125, 2001.

14. S. Molesa, D. R. Redinger, D. C. Huang, V. Subramanian, "High-quality inkjet-printed multilevel interconnects and inductive components on plastic for ultra-low-cost RFID applications", *Mat. Res. Soc. Symp. Proc.*, vol. 769, ppH8.3.1-8.3.6, 2003.

15. J. Chen, K. D. Wise, "A high-resolution silicon monolithic nozzle array for inkjet printing," *IEEE Tran. Elec. Dev.*, vol. 44, no. 9, pp1401-09, 1997.

16. F.G. Tseng, C.J. Kim, and C.M. Ho, "A high-resolution hgh-frequency monolithic top-shooting microinjector free of satellite drops" *Journal of Microelectromechan. Sys.*, vol.11, pp.427-447, 2002.

CHAPTER II

THEORETICAL BACKGROUND

2.1 Droplet formation process of DOD inkjet devices

Designing a high resolution DOD inkjet print head for maskless lithography requires a thorough understanding of its droplet formation process. A DOD inkjet device ejects fluid droplets by suddenly increasing the volume of an actuator, which generates a high pressure wave inside the inkjet chamber. The pressure wave propagates to the orifice and pushes a fluid column out through the nozzle. When the desired volume of fluid extends beyond the orifice, the pressure is reversed or terminated, and the liquid at the nozzle accelerates in the opposite direction. If the kinetic energy of the fluid extending beyond the orifice is sufficiently high, the liquid head will continue to elongate, forming a thin neck at the nozzle due to uneven velocity distribution along the liquid column. The high fluidic pressure at the thin neck magnifies the surface deformation, which causes a liquid volume to break from the nozzle. Surface tension then forms the ejected liquid head into a spherical shape. After droplet generation, the capillary force of the liquid meniscus refills the inkjet chamber through a channel to a fluid reservoir. The whole process is illustrated in Figure. 2.1.

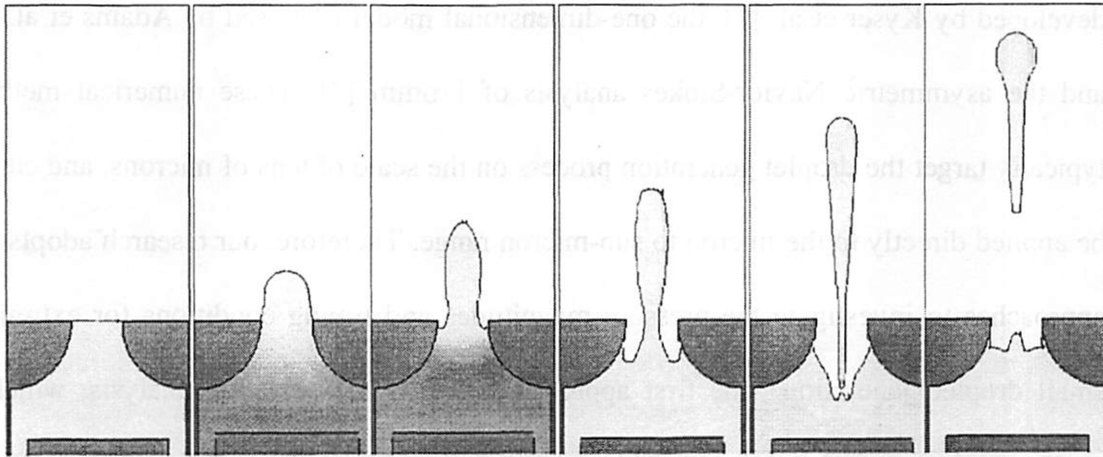

Figure 2.1: Droplet formation sequence of a DOD inkjet device

Since the liquid surface deformation plays an important role in droplet generation, the ejected liquid column is always longer than the nozzle diameter, and the final break-up droplet dimension is typically comparable to or larger than the nozzle size. Smaller nozzles generate smaller droplets. However, as nozzle size decreases, both the surface tension force and viscosity force increase, opposing the fluid acceleration; a higher actuation pressure is then necessary to push the liquid. Timing conditions of the pressure pulse are also important: a short pulse will not be able to push enough fluid volume through a nozzle with sufficient momentum, while a long pressure pulse will result in excessive droplet volume or satellite droplet formation. Our research has investigated the conditions for the generation of sub-micron to nano-meter scale droplets, which we will discuss in the following sections.

2.2 Droplet generation conditions of DOD inkjet devices

Many groups have used numerical simulation methods to study DOD inkjet operation processes. The reported approaches include the semi-empirical model

developed by Kyser et al. [1], the one-dimensional model proposed by Adams et al. [2], and the asymmetric Navior-Stokes analysis of Fromm [3]. These numerical methods typically target the droplet generation process on the scale of tens of microns, and cannot be applied directly to the micron to sub-micron range. Therefore, our research adopts two approaches to investigate the pressure magnitudes and timing conditions for extremely small droplet generation. The first approach simply scales existing analysis, which is quite straight-forward and can provide an intuitive understanding of the parameters that influence droplet resolution. The second approach is also based on numerical simulation, this time using a commercial fluidic computational tool, but specifically targets the droplet formation process on the micron and sub-micron scale.

2.2.1 Scaling analysis

Several forces will dominantly influence liquid flow in a micro-fluidic system, such as a drop-on-demand inkjet device, including hydrostatic pressure, liquid surface tension, liquid viscosity force, and fluid inertia. The force of gravity is typically negligible on the micron scale. For a liquid system with characteristic length L, characteristic velocity V, density ρ, surface tension σ, and viscosity μ, the relative strength of the these forces can be characterized by certain dimensionless constants, such as the Weber number and Reynolds number. The Weber number, $We=\rho \cdot V^2 \cdot L / \sigma$, can be interpreted as the relative strength between fluid inertia and surface tension force or energy, while the Reynolds number, $Re=\rho \cdot L \cdot V/\mu$, expresses the relative strength between the fluid inertia and viscous force.

Assume that a square-shaped hydrostatic pressure pulse with magnitude of Po and pulse width of t_o is applied to a nozzle with radius of R, as shown in Figure 2.2.

Here, we assume that the nozzle thickness is very small, so little viscous pressure will be lost inside the nozzle. We can divide the droplet ejection process into two stages: acceleration stage (before time t_o) and the droplet formation stage (after time t_o). At the end of the liquid acceleration stage, the pressure pulse forces a fluid head with volume Vol through the nozzle with average velocity V (Figure 2.2). To overcome the large liquid surface deformation that tends to reduce the fluid momentum and draw the fluid back to the nozzle during the droplet generation stage, the fluid head should have an inertial energy much larger than its surface tension energy at the end of liquid acceleration. Therefore, we use the Weber number of the fluid system:

$$We=\rho \cdot V^2 \cdot r/ \sigma \sim k>10 \qquad [2.1]$$

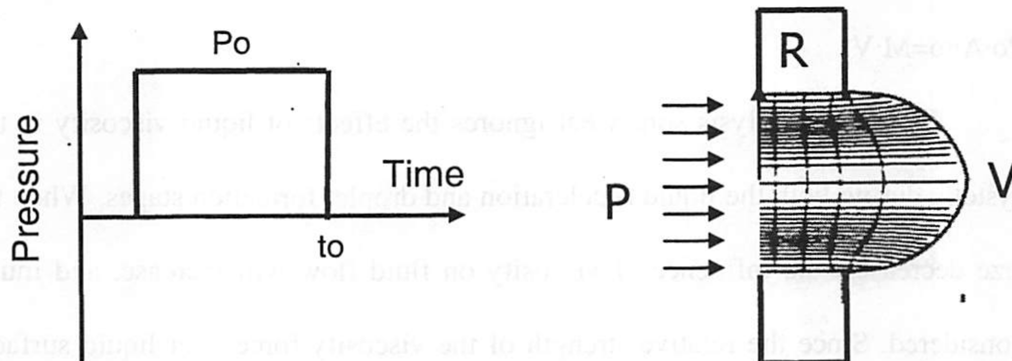

Figure 2.2: Input pressure profile and the liquid meniscus shape at the end of liquid acceleration

Here, the value of k is an arbitrarily chosen number, estimated from the possible surface energy increase during the droplet deformation stage (refer to Figure 2.1). The liquid velocity V at the end of fluid acceleration will scale as:

$$V\sim (k \cdot \sigma/\rho \cdot r)^{1/2} \qquad [2.2]$$

Since the fluid inertial energy comes from the work done by the hydrostatic pressure, from the work function:

$$(Po-\sigma/r)*Vol=MV^2/2 \qquad [2.3]$$

the minimum actuation pressure for single droplet generation should then scale as

$$Po \sim k/2 \cdot \sigma/r \qquad [2.4]$$

Here, we assume that $Po>>\sigma/r$, since $k>>1$. Since the generated liquid droplet size is typically comparable to or larger than the nozzle size, a volume of fluid more than $Vol=4/3 \cdot \pi \cdot r^3$ must flow through a nozzle with area $A=\pi \cdot r^2$ during the acceleration phase. Assuming that the velocity of the fluid increases linearly, the required pressure pulse width for a single droplet formation can be expressed as:

$$t_o \sim 2*Vol/V/\pi \cdot r^2 \sim 3*(\rho \cdot r^3/k\sigma)^{1/2} \qquad [2.5]$$

The same expression can also be obtained using a fluid momentum equation $Po \cdot A \cdot to=M \cdot V$.

The above analysis somewhat ignores the effects of liquid viscosity in the fluidic system, during both the liquid acceleration and droplet formation stages. When the nozzle size decreases, the influence of viscosity on fluid flow will increase, and must also be considered. Since the relative strength of the viscosity force over liquid surface tension force can be characterized as:

$$We/Re=\mu V/\sigma=(k\mu^2/\sigma \cdot \rho \cdot r)^{1/2} \qquad [2.6]$$

We could then adjust the coefficient k of all the above equations to:

$$k' =k \cdot (1+ We/Re) \qquad [2.7]$$

As shown in Figure 2.3, for pure water, the parameter We/Re is small when the nozzle radius is relatively big, and the value increases to about 1 when the nozzle radius is reduced to 100nm. The viscosity force becomes increasingly dominant as the nozzle size is further reduced to the scale of tens of nano-meters. For nozzles with dimensions

larger than 100nm, which produce droplets in the size range most interesting for maskless lithography applications, the surface-tension-based analysis combined with viscous effect adjustment factor We/Re should be valid.

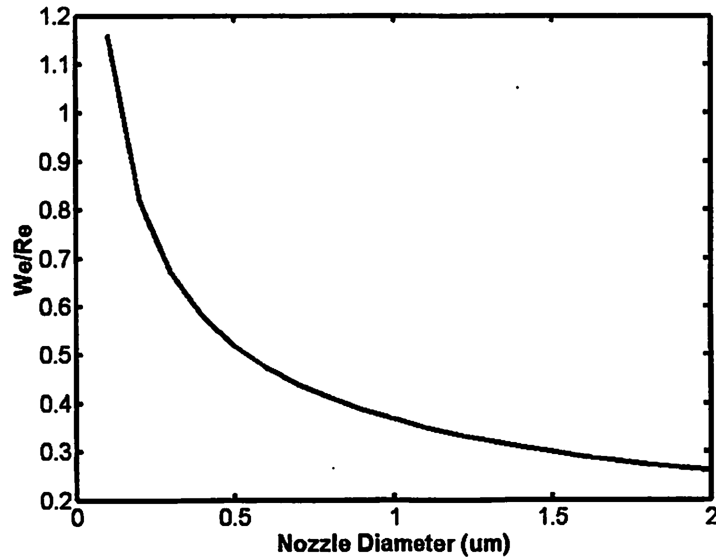

Figure 2.3: Relative strength of the liquid viscosity over liquid surface tension vs. nozzle diameter in a DOD inkjet device

Table 2.1 summarizes the above scaling analysis, with estimated values of actuation pressures P, characteristic liquid velocities V, and time constants t_o for water droplet generation with nozzle radii varying from 10um to 100nm. As with any scaling analysis, the actual value of the parameters may not be that meaningful, since there is an arbitrarily chosen number k in our analysis. However, the table does tell us that the scaling of the required pressure magnitude for droplet ejection is almost inversely proportional to the nozzle radius, and that the pressure pulse width falls as $r^{3/2}$ for single droplet formation. In order to generate a water droplet in well within the sub-micron scale, the pressure transducer in an inkjet chamber must create an actuation pressure

pulse several MPa in amplitude and tens of nano-seconds long. The liquid surface tension and viscosity coefficients are also important parameters influencing the droplet formation process. For typical organic solvents, which have surface tension values (~0.3N/m^2) about half that of the water (~0.74N/m^2), the required pressure magnitude also halves.

d (μm)	2r	10	2	0.4	0.1
Vol (pL)	$4\pi r^3/3$	0.52	4.2e-3	3.4e-5	5e-7
V_{max} (m/s)	$(k'\cdot\sigma/\rho\cdot r)^{1/2}$	9	22	54	126
to (s)	$3*(\rho\cdot r^3/k'\sigma)^{1/2}$	1.7e-6	1.4e-7	1.1e-8	1.2e-9
Po (MPa)	$k'\cdot\sigma/2r$	0.08	0.47	2.9	16

Table 2.1: Summary of droplet volume, maximum liquid velocity during fluid acceleration, pressure pulse width and minimum actuation pressure for single droplet generation with nozzle dimension in micron to submicron scale using the scaling analysis

2.2.2 Numerical simulation results

Although the scaling analysis can give us some intuitive idea of how the actuation pressure magnitude and timing conditions change with the target droplet radius, it uses a simplified model, and overlooks many parameters that could also influence droplet formation, including nozzle shape and thickness, the pressure pulse profile, inkjet chamber dimensions, etc. Designing an inkjet device to reach the highest droplet resolutions requires the study of these parameters and their effects, since the actuation condition is typically fixed for a certain type of inkjet device. Therefore, our research also uses a commercial computational fluid dynamic simulation tool—CoventorWare™ — to study the droplet formation process on the micron to sub-micron scale.

The core of the software is a Flow-3D engine, which solves 2-D and 3-D Navier-Stokes equations using a finite-element method, and utilizes a Volume of Fluid (VOF) method to treat large liquid-gas interface deformation during the droplet break up stage. It can also assign different boundary conditions and fluid properties to the inkjet device, providing a much more complete and accurate prediction of DOD inkjet operation behavior. Our version of the tool is limited in its inability to calculate a pressure transducer's generated pressure wave directly from an input electric signal, either for a piezoelectric type or a thermal bubble type device. An arbitrary pressure shape had to be used as an input. Also the software could only treat the fluid as an incompressible medium; the simulated results therefore overlook the acoustic effect of the pressure pulse inside the inkjet chamber and at the nozzle boundaries.

2.2.2.1 Droplet generation conditions

Figure 2.4 shows the droplet generation condition in a simulated ink jet device. The device has a converging-shaped nozzle of varying diameter. A converging-shaped nozzle is used because it requires the smallest droplet actuation pressure (this will be discussed in next section). A pressure source placed at the bottom of an inkjet chamber applies a dual-polarized, triangular-shaped pressure pulse with magnitude Po and width t_o to the inkjet device, as shown in Figure 2.4. The pressure shape is chosen because it is the optimum pressure profile for droplet ejection, and also is close to the pressure profile generated by a piezoelectric transducer in a short pulse width. The inkjet chamber is much larger in diameter than the nozzle, and its thickness is relatively small.

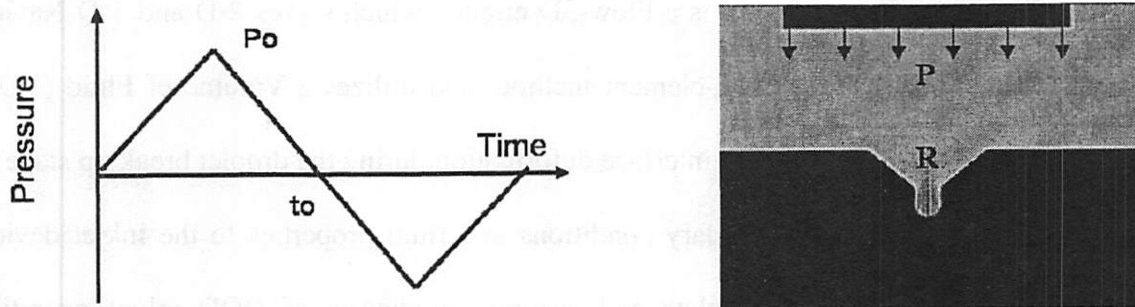

Figure 2.4: Input pressure profile and the device struature for the numerical simulation

Our simulation shows that fluid will only form a meniscus outside the nozzle, not a droplet, if the pressure magnitude is too low. Sustaining this pressure will only create a larger pile of fluid, since there is not enough liquid momentum for surface deformation. The droplet break-up happens only when the pressure magnitude reaches a certain value. At this value, if the pressure is not sustained for long enough, a small fluid column forms and undergoes slight surface deformation, but its net momentum becomes zero before break-up occurs, and the fluid is drawn back to the chamber, as shown in Figure 2.5(a). If the pressure pulse is long enough, a thin liquid neck forms at the nozzle, and single droplet generation can be observed. A simulated droplet generation sequence is shown in Figure 2.5(b). The generated droplet is almost the same size as the inkjet nozzle. If the pressure pulse further increases, the generated droplet increases in velocity and slightly in volume; multiple droplets form at even longer pulse widths or higher pressure magnitudes (Figure 2.5(c)). Under conditions for satellite droplet formation, the main droplet is typically larger than one produced under single-droplet conditions, but never exceeds twice the nozzle diameter in size.

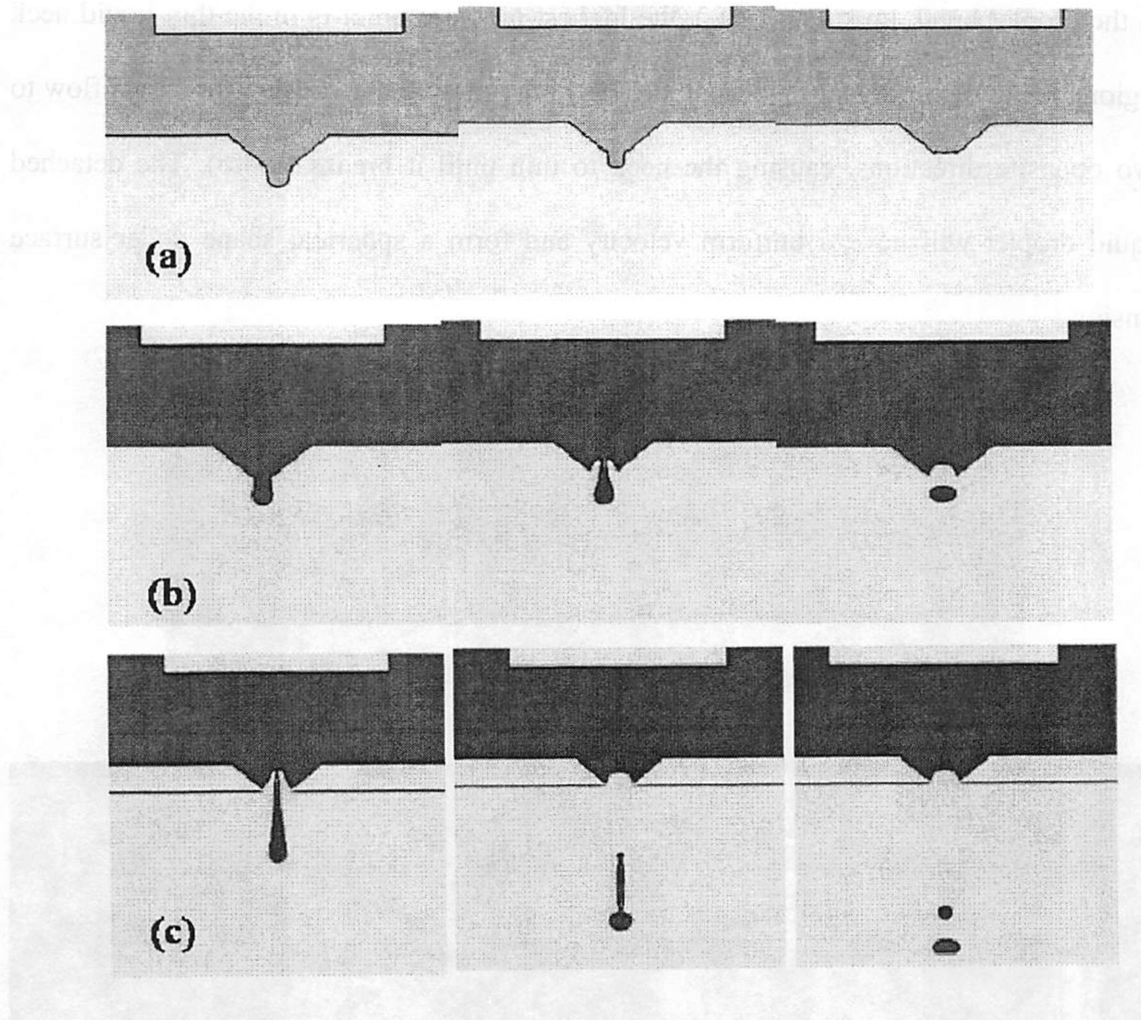

Figure 2.5: Simulated droplet generation sequence through a 400nm converging shaped nozzle. Top: actuation pressure Po=2MPa, to=1e-8s; center: actuation pressure Po=5.4MPa, to=1e-8s; bottom: actuation pressure Po=10MPa, to=1e-8s.

The fluid velocity and pressure distribution during the formation sequence for a single droplet is also shown in Figure 2.6. We can see that the viscous pressure drop inside the inkjet chamber is negligible throughout the droplet formation sequence, since the chamber is much larger than the nozzle and the average liquid velocity in the chamber is small. The pressure drops quickly at the nozzle region due to the high fluid acceleration. The liquid velocity is quite uniform in the liquid column at the end of the acceleration ($t=t_o$), and becomes non-uniform after a negative pressure is applied ($t=2t_o$).

In the droplet break up stage (t~$3t_o$), the highest pressure point is in the thin liquid neck region, due to the liquid surface tension. This high pressure then pushes the liquid flow to two opposite directions, causing the neck to thin until it breaks (t~4to). The detached liquid droplet will have a uniform velocity and form a spherical shape under surface tension.

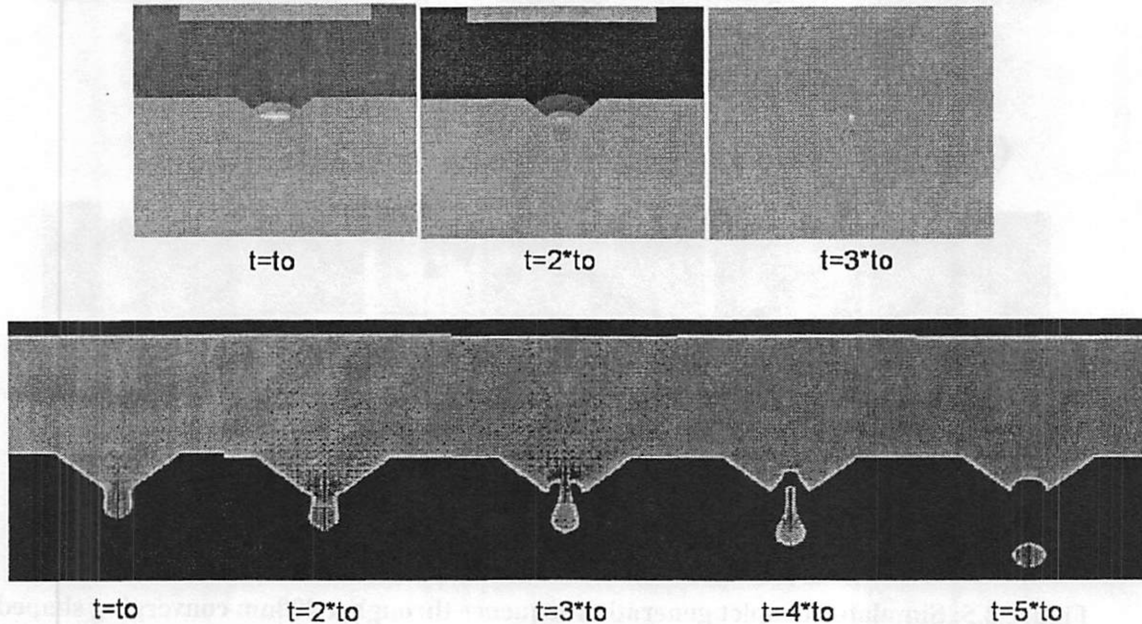

Figure 2.6: Top: hydraulic pressure distribution during droplet formation process. Bottom: liquid velocity distribution, the arrow length is proportional to the liquid velocity

The simulated minimum actuation pressure and the corresponding pressure pulse width for single-droplet generation are listed in Table 2.2, for nozzles varying in diameter from 10um to 100nm. This behavior scales almost identically with the results in Table 2.1, even though a different pressure profile is applied, which means that our simple scaling analysis does capture the main factors that influence droplet generation process in the micron to sub-micron scale.

d (μm)	10	2	0.4	0.1
Vol (pL)	0.52	4.2e-3	3.4e-5	5e-7
V_{max} (m/s)	9	19	42	84
to (s)	2e-6	1e-7	1e-8	2e-9
Po (MPa)	0.14	0.7	5.4	28.8

Table 2.2: Summary of droplet volume, maximum liquid velocity during fluid acceleration, pressure pulse width and minimum actuation pressure for single droplet generation with nozzle dimension in micron to submicron scale using the numerical simulation method

2.2.2.1 Influence of the pressure profile, nozzle shape and fluid properties

We have also studied the pressure profile shape's influence on the droplet generation process. Triangular and square-shaped pressure pulses with single or double polarities have been used for simulation, and the results compared. We find that the droplet generation is easier (less pressure is needed to maintain t_o) if the pressure becomes negative at the end of liquid acceleration. The negative pressure helps draw the fluid back into the nozzle while the liquid head continues forward, thereby increasing the velocity non-uniformity along the fluid column, causing easier surface deformation and breakup. This also moves the droplet breaking point closer to the nozzle (or inside the nozzle if the negative pressure is high), as shown in Figure 2.7. For a pressure pulse with excessive negative polarity (Pn>Po), a large amount of fluid will be drawn back to the chamber (Figure 2.7(c)), which increases the inkjet refilling time and reduces the ejected droplet velocity. A negative pressure magnitude of about half the positive magnitude may be optimum for inkjet operation. Our simulation also used square-shaped pressure pulses. A square pressure wave requires almost half the magnitude of a triangular wave, which is

reasonable, since it is the total work done by the actuation pressure that counts. The two pressure shapes show almost identical droplet generation processes. A real piezoelectric transducer may generate a pressure profile more like the triangular-shaped pressure profile, though it is likely somewhere between the two.

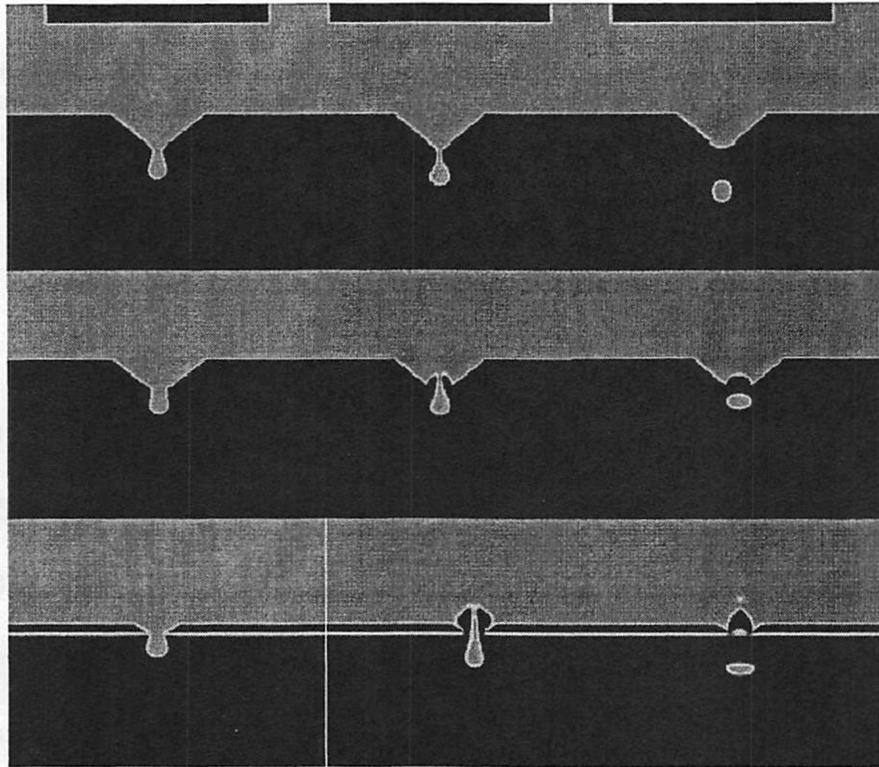

Figure 2.7: Droplet formation sequence with different pressure shape. Top: Pn=0, center: Pn=Po, bottom: Pn=2Po

We have also studied the impact of the nozzle shape on the droplet generation conditions. Our simulations study converging nozzles, diverging nozzles, and cylindrical nozzles with similar radii but different aspect ratios. Results show that a converging nozzle needs less pressure to generate a droplet than a cylindrical nozzle with the same nozzle radius (as shown in Figure 2.8). This is because that the viscosity force exerted by the nozzle wall is related to the liquid velocity variance along the nozzle radius

(F_viscous~μ∀.V), which, in a converging nozzle, is smaller on average, with a bigger flow area. A diverging nozzle requires even smaller pressure, since the actual nozzle thickness can be treated as infinitely small, but is typically not used in inkjet devices because of the droplet generation instability issues. Considering the acoustic behavior of the pressure pulses make converging nozzles even more favorable, since they also have less pressure reflectance from the nozzle boundaries.

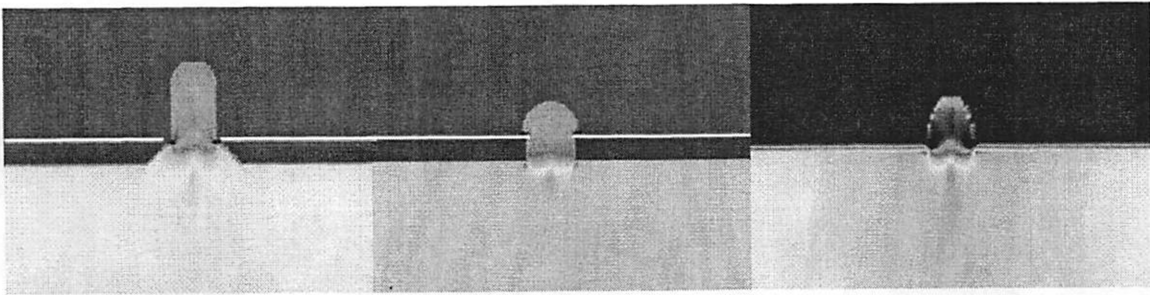

Figure 2.8: Pressure distribution during droplet generation for a converging-shaped nozzle and cylindrical nozzles with different thickness.

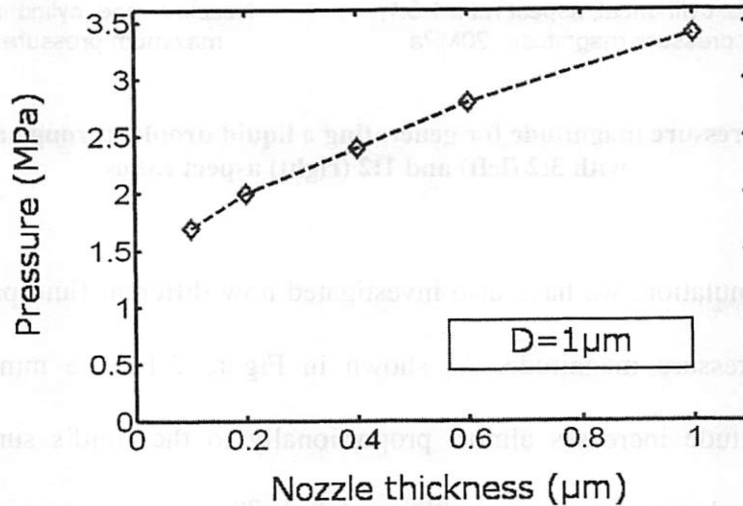

Figure 2.9: Required actuation pressure vs. nozzle thickness for single droplet generation with nozzle diameter of 1μm

Among the cylindrical nozzles, shorter nozzle lengths require lower pressure magnitudes for droplet generation, since they lose less viscous pressure along the nozzle (Figure 2.8). The required pressure magnitude vs. nozzle thickness for a nozzle with diameter 0.5um is plotted in Figure 2.9. The nozzle length effect is dominant for even smaller nozzles. For nozzles with diameter of 200nm, the required actuation pressure almost doubles if a nozzle with aspect ratio of 3:2 is used compared with a nozzle with aspect ratios of 1:2 (Figure 2.10).

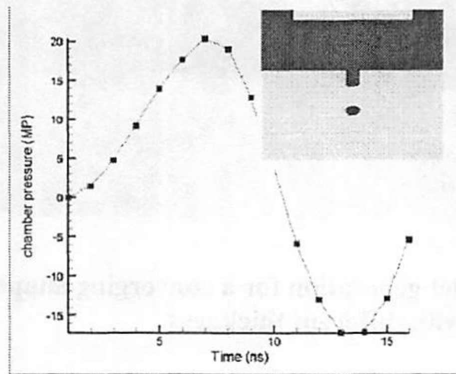

Nozzle shape: cylindrical, aspect ratio:1.5:1, maximum pressure magnitude: 20MPa

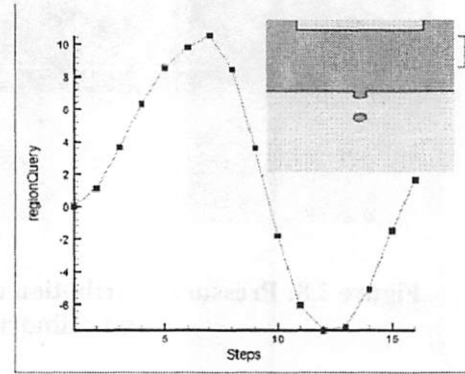

Nozzle shape: cylindrical, aspect ratio:0.5:1, maximum pressure magnitude: 11Mpa

Figure 2.10: Pressure magnitude for generating a liquid droplet through a 200nm nozzle with 3:2 (left) and 1:2 (right) aspect ratios

In our simulation, we have also investigated how different fluid propeıties change the required pressure magnitude. As shown in Figure 2.11, the minimum actuation pressure magnitude increases almost proportionally to the fluid's surface tension, if nozzle shape and pressure pulse width are fixed. This is consistent with our scaling analysis. The influence of liquid viscosity over pressure magnitude, however, is not studied, because the simulation did not support changing the appropriate parameter.

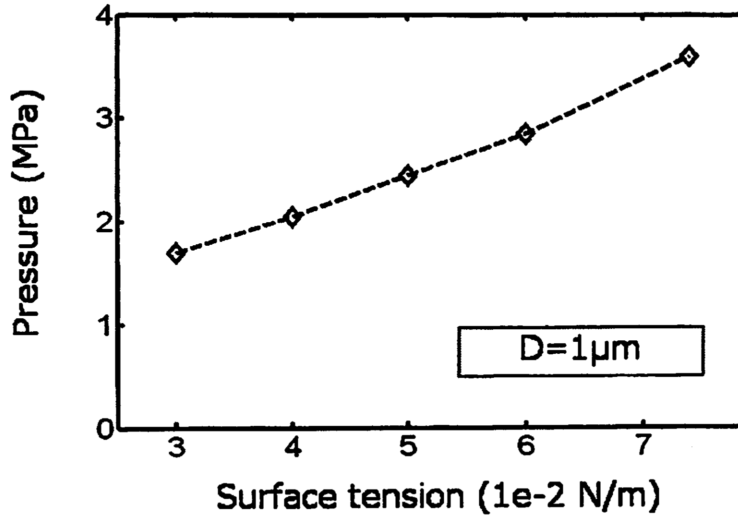

Figure 2.11: Actuation pressure vs. liquid surface tension for single droplet generation with nozzle diameter of 1μm

In summary, in order to develop an inkjet printing maskless lithography system, we investigated micron to submicron scale droplet generation conditions for a DOD inkjet device, using both scaling analysis and numerical simulation methods. The predicted actuation pressure increases in an almost inverse proportion to the nozzle radius, and the time constant changes as $r^{3/2}$. According to our study, ejecting a liquid droplet on the 100nm scale would require a pressure pulse with magnitude as high as 20MPa and a pulse width in the 1ns range to be generated inside an inkjet chamber. Using a dual polarized pressure pulse, a converging nozzle, smaller nozzle thicknesses and fluid with lower surface tension and viscosity coefficients should make the droplet formation process easier.

Reference

1. E. L. Kyser, L.F. Collins, N. Herbert, "Design of an Impulse Inkjet Jet", *Journal of Applied Photographic Engineering,* Vol, 7, pp73-75, 1981.

2. Adams, R. L.; Roy, J. "A one dimentional numerical model of a drop-on-demand ink jet", *Journal of Applied Mechanics*, vol. 53, pp. 193-7, 1986.

3. J.E. Fromm, "Numerical Calculation of Fluid Dynamics of Drop-on-Demand Jets". *IBM J. Res. Develop.*, Vol. 28, 322-33, 1984.

CHAPTER III

PRINT HEAD DESIGN

3.1 Actuation mechanism

3.1.1 DOD inkjet device comparison

As discussed in Chapter I, a variety of actuation methods have been reported to eject droplets in DOD inkjet devices, including piezoelectric [1], thermal bubble [2], acoustic [3], electrostatic, [4] etc. Although commercially successful today, piezo-based print heads use bulk piezoelectric material as pressure transducers, which require a large device area to achieve sufficient displacement volume and actuation strength. The number of inkjet devices on a print head is thus limited (about 180 on the most advanced piezoelectric cartridges). An acoustic device ejects a droplet from a free liquid surface by a pressure gradient generated from the interference of acoustic waves. The acoustic transducer typically has an area larger than 400μm, which cannot be reduced without sacrificing interference strength and, hence, device performance. It also requires precise control over the thickness of the liquid film, which could cause problems for reliable droplet ejection. Electrostatic inkjet devices use the bending of a flat plate under an electrostatic field for actuation, and have device areas of about 500x500μm in the original design. Even though the actuator size could be reduced, the limitations of the

bending plate make it difficult to satisfy the requirements for high actuation pressure and short response time simultaneously. Thermal bubble inkjet devices, on the other hand, only use small thermal heaters for actuation, thanks to the free expansion of the vapor bubble. They are also compatible with micro-fabrication processes, because of their simple heater structure, and more robust, because of their lack of moving mechanical parts. The devices could then be made into a dense array to fulfill the most stringent throughput requirements of maskless lithography applications (Table 1.2). Through theoretical analysis, we also found that they could generate micron and even submicron scale droplets (refer the following sections). Therefore, in our research, we have chosen the thermal bubble inkjet technology in the design of our first version of an inkjet print head for maskless lithography purposes.

One drawback of a thermal bubble inkjet printing system is that thermal properties limit the scope of materials it can handle. This problem could be addressed using solutions containing nano-sized particles. The solvent could be chosen to provide high vapor pressure with low surface tension and viscosity coefficients, while the nano-particles could possess different physical properties such as conductivity, semi-conductivity, magnetism, etc for various applications. We will discuss more of materials-related issues in Chapter VI.

3.1.2 Thermal bubble Inkjet Operation mechanism

In a thermal bubble inkjet device, a smooth, micro-fabricated heater heats the liquid inside a chamber in several microseconds, with thermal flux greater than $100MW/m^2$ [5]. Since there is no heterogeneous nucleation site on the heater surface, liquid will not evaporate until it reaches the superheat temperature limit at the liquid-solid interface

(about 300°C for water). At this temperature, homogeneous nucleation occurs on the whole heater surface, and a thin vapor film then quickly grows up as water vapor evaporates into the nucleus. In the initial bubble growth phase, the vapor bubble pressure is much higher than the ambient pressure, due to the extremely high fluid temperature. The vapor bubble then pushes the vapor/liquid boundary, accelerating the fluid inside the chamber and the nozzle. At the same time, energy is removed from the thin superheated liquid layer through evaporation; the bubble temperature, which is almost the same as the surrounding fluid temperature, decreases quickly as bubble grows, and bubble pressure drops exponentially. The vapor-liquid boundary stops moving when the pressure inside the bubble is significantly lower than the ambient pressure. The bubble then begins to collapse, and droplet detachment occurs, due to the mechanism described in chapter II. After droplet ejection, the chamber will be refilled by capillary force. Figure 3.1 illustrates the whole operation cycle of a thermal bubble inkjet device.

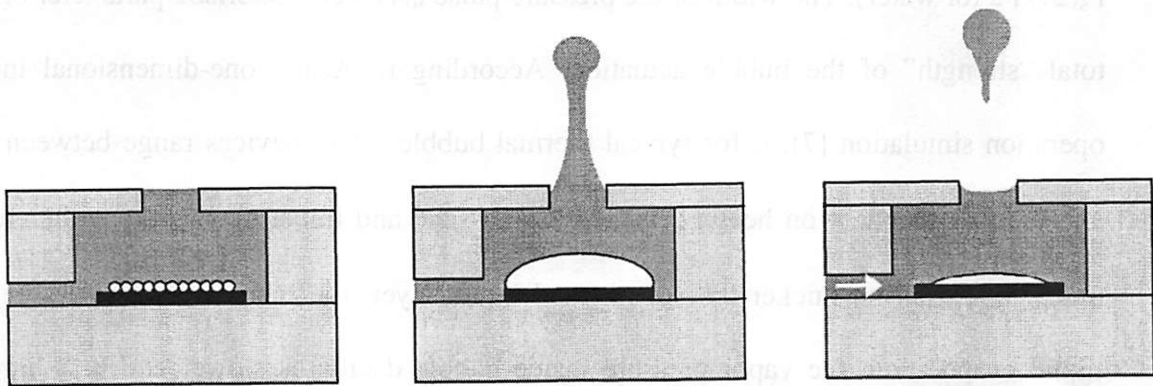

Figure 3.1: The operation cycle of a thermal bubble inkjet device; (a) bubble nucleation, (b) bubble growth, (c) bubble collapse, droplet break-up and chamber refilling.

3.1.3 Pressure characteristic and droplet size limit

The pressure characteristic of a thermal bubble inkjet device is quite complicated and difficult to measure by experimental methods. Asai et al. have investigated nucleation, growth and collapse behaviors of vapor bubbles, based on nucleation probability, vapor phase functions, and thermal transfer phenomena, developing a practical pressure model for characterization of thermal bubble inkjet devices [6]. Their model expresses the typical vapor pressure as:

$$P_b = (P_g - P_s)\exp[-(t/t_o)^{1/2}] + P_s; \qquad [3.1]$$

where P_g is the initial bubble pressure and is close to the saturated vapor pressure of the fluid at the nucleation temperature. Since the nucleation temperature has very small variance under conditions for inkjet operation (~300C for water), P_g is almost fixed for any given material. It is about 4MPa for water. The pressure will then decay exponentially as time progresses, until it reaches the vapor pressure at room temperature, P_s(27kPa for water). The width of the pressure pulse t_o is a characteristic parameter of the total "strength" of the bubble actuation. According to Asai's one-dimensional inkjet operation simulation [7], t_o for typical thermal bubble inkjet devices range between 0.1 and 0.2μs, dependent on heating history, heater size, and inkjet design. It can be easily understood that the thicker the superheated liquid layer, the more energy available for liquid evaporation; the vapor pressure inside bubble decreases slower and t_o is bigger. Larger heater sizes and higher liquid resistance to bubble expansion also increase t_o. A bubble pressure profile with t_o=0.1μs is shown in Figure 3.2.

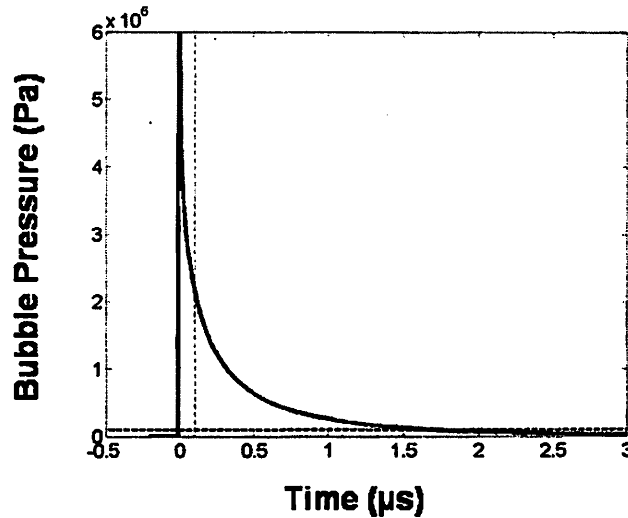

Figure 3.2: Bubble pressure profile of a thermal bubble inkjet device with to=0.1μs, Pg=6MPa

Using the pressure characteristic from equation 3.1, ConventorWare allowed us to investigate the size limitations of droplets produced by thermal bubble inkjet devices. Assuming an initial bubble pressure Po=4MPa (the saturated vapor pressure of water at 270°C), and t_o varying between 0.01 and 0.2μs, our simulation shows that the smallest droplet that a thermal bubble device could generate would be around 0.5μm in diameter, through a converging shape nozzle with diameter of 400nm and aspect ration of 4:1 (100nm thick) (Figure 3.3(a)). The condition for single droplet generation is found to be at t_o~0.1μs. With a smaller t_o, the liquid would have insufficient liquid momentum to break up (Figure 3.3(b)), while larger t_o would cause multiple droplets to be formed (Figure 3.3(c)). If we further decrease the nozzle dimensions, no matter how we adjust t_o, only a liquid bundle will be pushed outside the nozzle, which will not experience sufficient surface deformation with the given bubble pressure profile (Figure 3.4). Water droplets 0.5μm in diameter are therefore

the minimum predicted for thermal bubble devices. Similar studies were also performed for organic solvents such as methanol and toluene. Methanol has a superheated temperature limit around 230°C and hence a Po magnitude around 1MPa. Since it also has a surface tension coefficient about half of that of the water, a minimum droplet dimension around 1μm is estimated.

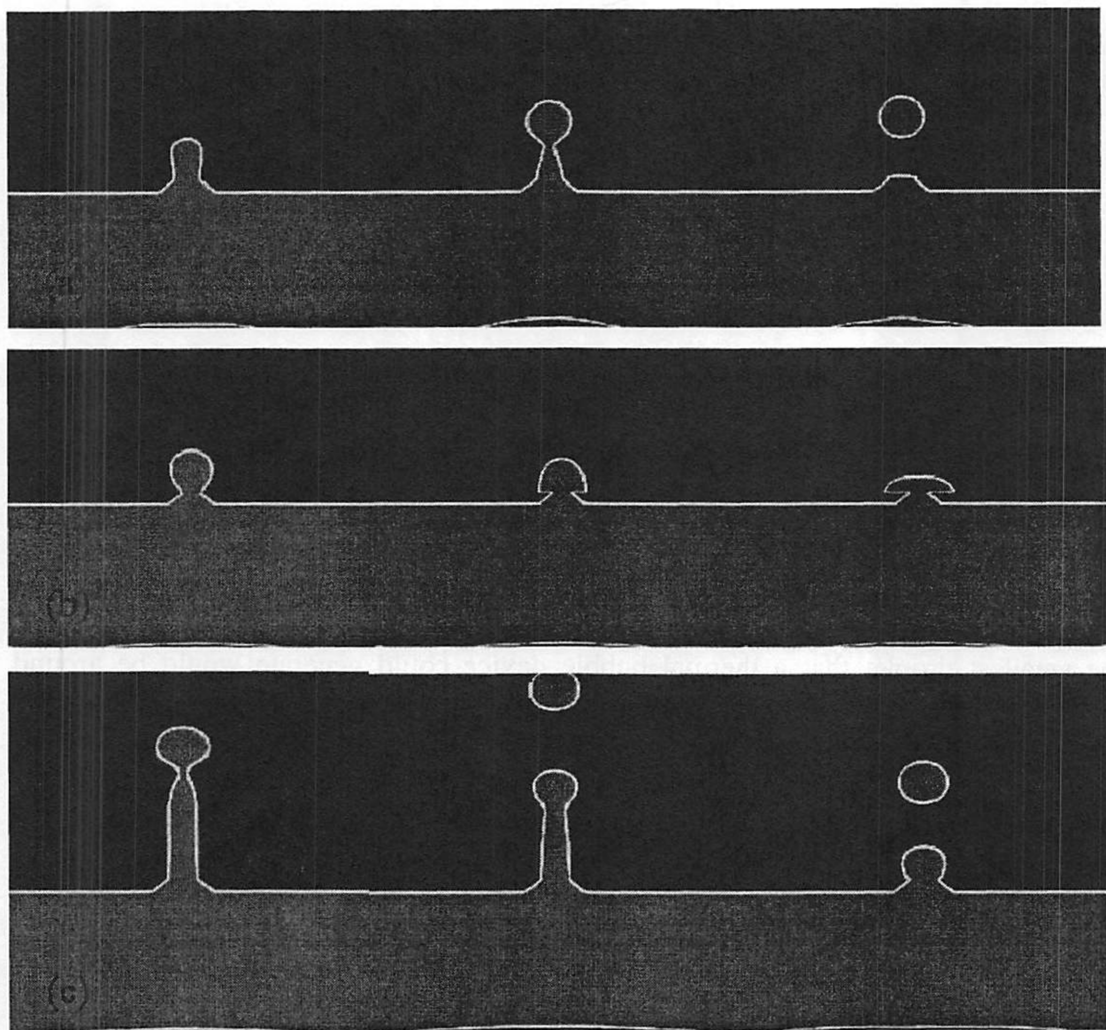

Figure 3.3: Simulated droplet generation result for thermal bubble inkjet device: (a) a 0.5μm scale droplet generation through a 0.4μm nozzle with to=0.1μs; (b) no droplet generation with to=0.08μs; (c) multiple droplets generated with to=0.2μs.

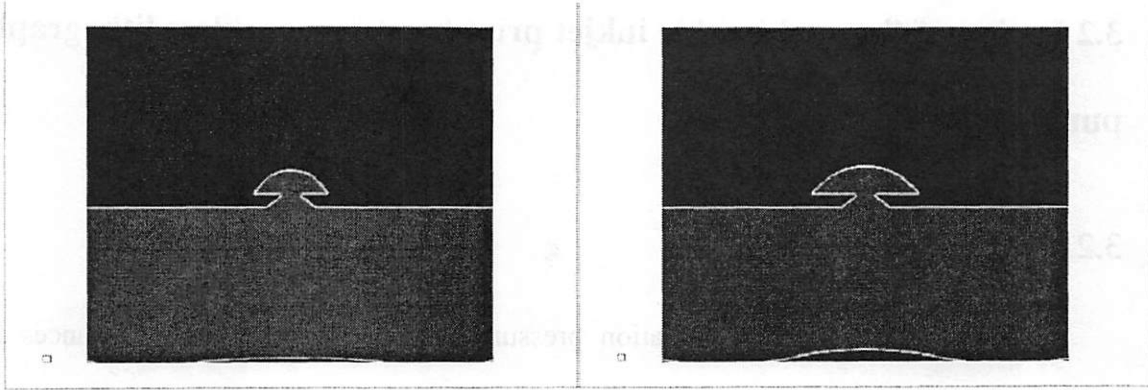

Figure 3.4: Simulated droplet generation result for thermal bubble inkjet device: no droplet generation occurs for a 0.2μm nozzle with to=0.2μs

One caveat that should be mentioned here, regarding the simulated minimum droplet size, is that the peak pressure Po=4MPa and exact timing condition (t_o=0.1μm) may not be achievable in a real inkjet device. The bubble pressure characteristics could be far more complicated than the simple exponential shape, due to the thermodynamic and hydrodynamic coupling of the heater, the vapor bubble, and the fluid system; acoustic and viscous pressure will be lost inside the inkjet chamber and nozzle boundaries. The theoretical droplet size limit must therefore be verified by experimental methods (we will get back to this point in Chapter V).

However, the result does give us a rough idea of the possible droplet dimensions that a thermal bubble device could produce. It is then worthwhile to pursue our research to optimize the design and fabrication process of a thermal bubble inkjet print head to reach a higher resolution than the current inkjet printing systems. These devices could then be used for possible maskless lithography applications, including patterning organic transistor circuits and MEMS devices, for which micron to submicron scale droplet resolutions are sufficient.

3.2 Design of thermal bubble inkjet print head for maskless lithography purpose:

3.2.1 The design issues

Besides achieving high actuation pressures and low liquid flow resistances for smaller droplet formation, designing an inkjet print head for maskless lithography demands many other considerations.

The first issue is droplet repetition rate. A high repetition rate is preferred, since it allows us to reduce the device density on the substrate, and therefore ease the design and fabrication requirements of the print head. The time interval between the generations of consecutive droplets is determined by the combination of heating time, heater cooling time, droplet generation time, chamber refilling time, and fluid damping time. In a micron to submicron scale inkjet device, the typical droplet formation time is shorter than 1μs as been shown in table 2.1&2. Decreasing the heater cooling, chamber refilling and fluid damping times are thusly the objectives of our design.

The second issue is droplet generation stability, which is mostly influenced by the stability of bubble formation and the shape of the nozzle. For an inkjet device to operate continuously at a given pressure characteristic, the bubble formation must be tightly controlled, which means precise heater design. Droplet generation instability is mostly influenced by the nozzle shape and wetting condition, which we will discuss in detail later.

The third issue is energy consumption. Since maskless lithography demands an extremely high rate of droplet formation, the amount of energy consumed can be huge,

and cooling the print head can be problematic. A low firing energy per droplet is thusly preferred.

Other significant issues include small device area, which we have discussed many times, chemical compatibility, to print different materials, and robust print head and device structure, for a long operational lifetime. These issues are not only important for a thermal bubble inkjet print head, but also the basic requirements for any type of print head designed for maskless lithography applications. Taking all this issues into consideration, we have designed a high resolution, high-speed thermal bubble inkjet print head based on silicon micro-machining technology.

3.2.2 The overall print head structure

The overall structure of the proposed print head is shown in Figure 3.5. It is composed of a large array of thermal bubble inkjet devices formed on top of a silicon substrate. Each device is connected to a fluid reservoir in the back of the substrate through a square-shaped feeding hole formed by through-wafer etching. The individual feeding holes eliminate the large, common flow-channels used in other inkjet print heads [8-9], increasing the strength of the print head structure, and minimizing device cross-talk and the possibility of widespread device failure. The feeding holes can also been shared between adjacent devices to reduce device area. The devices are connected to electric data lines that carry the driving signals from an integrated controlling circuit to each device. An integrated controlling circuit must be built on chip because of the huge amount a data to be handled for maskless lithography purposes. (For example, a print head would require about 10Tbit of data to control the individual devices involved in patterning an 8 inch wafer in 5 min with a pixel size of 0.5μm).

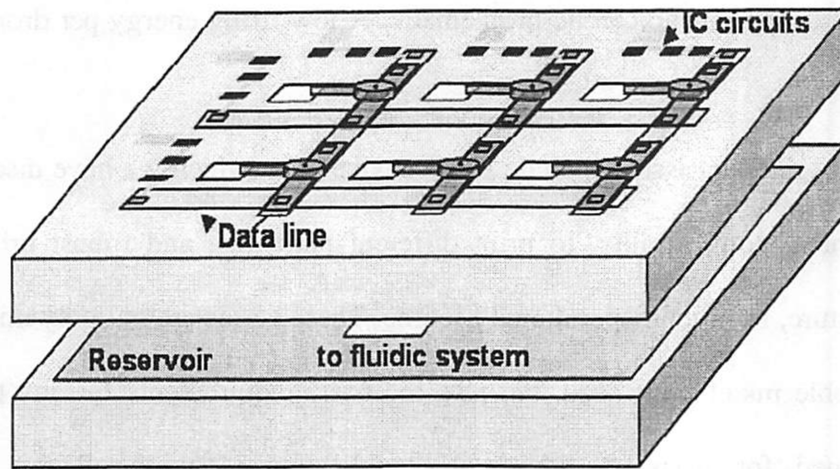

Figure 3.5: Schematic structure of a thermal bubble inkjet print head designed for inkjet printing maskless lithography system

3.2.3 The device structure

As described in Chapter I, thermal bubble inkjet devices can be categorized as top-shooters or side-shooters, depending on their structure [10]. A top-shooter ejects droplets vertically from the heater (typically used in HP cartridges), while a side shooter ejects droplets parallel to the heater (typically used in Canon cartridges), both shown in Figure 3.6. Side shooters require nozzles far away from the heater surface and lose more acoustic pressure in the chamber. Additionally, their nozzle sizes are coupled with the inkjet dimensions and hard to reduce. Therefore, our inkjet print head uses a top shooter device structure.

The top and cross section views of our top-shooting thermal bubble inkjet device are illustrated in Figure 3.7. A small nozzle opens in a thin membrane, separated by a shallow fluid chamber from a thin-film Pt heater stack. The chamber is connected to a liquid feeding hole with a long, narrow refilling channel. The shape and dimensions of the inkjet nozzle, heater, chamber, and refilling channels directly determine the droplet

resolution as well as the device's operation frequency and energy consumption, and so must be carefully designed. The detailed design consideration of these components will be discussed in the following sections.

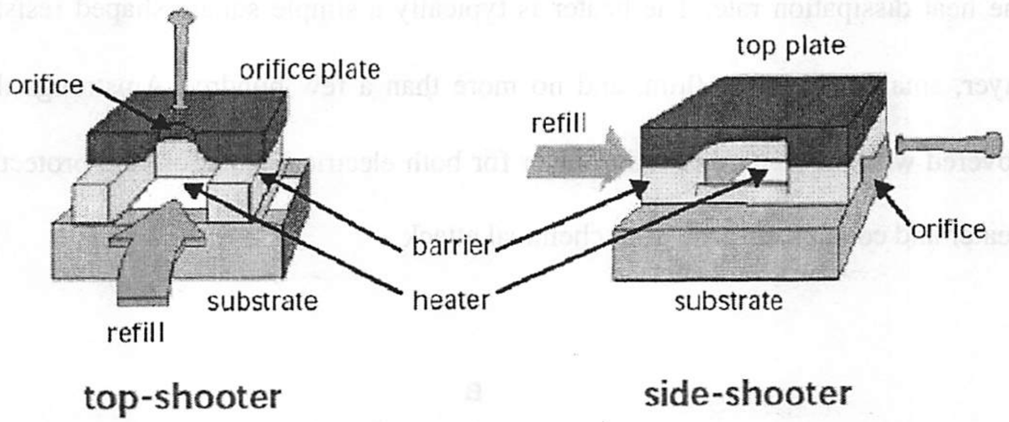

Figure 3.6: Thermal bubble inkjet device structures [10]

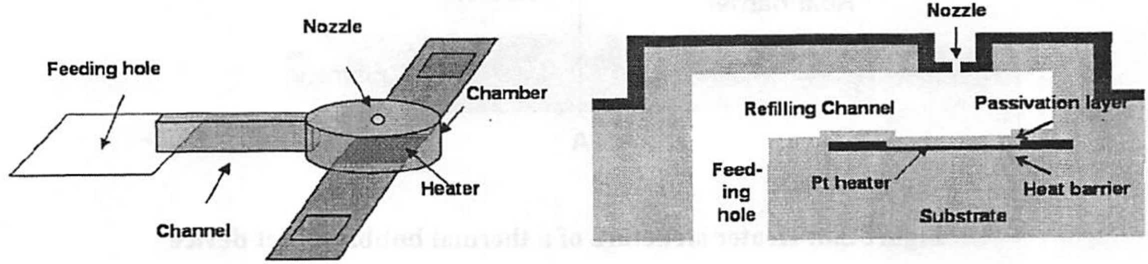

Figure 3.7: Schematic diagram of our top-shooting thermal bubble inkjet device. Left: top view, right: cross section

3.2.4 Heater design

3.2.4.1: Heater structure

The thin film heater is the most critical part of a thermal bubble inkjet device, since it directly influences the bubble pressure characteristics. The structure of a typical inkjet heater stack is shown in Figure 3.8. It consists of a substrate, a heat barrier layer, a thin

film heater, electrical contacts and a passivation layer [11]. The substrate provides structural support for the thin film device. The heat barrier controls the heat diffusion from the heater into the substrate and therefore determines the energy consumption and the heat dissipation rate. The heater is typically a simple square-shaped resistive metal layer, smaller than 60x60μm, and no more than a few hundred Amstrongs thick. It is covered with an inert passivation layer for both electrical isolation and protection of the heater and contact surfaces from chemical attack.

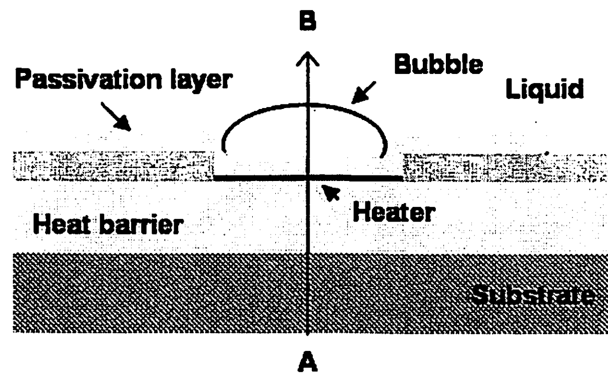

Figure 3.8: Heater structure of a thermal bubble inkjet device

Our inkjet device uses a silicon substrate, for its high thermal conductivity and associated superior heat removing capability. This is important because the inkjet print head will operate at extremely high frequency, generating a large amount of heat. Local heat buildup will greatly influence the device performance. Both the heater barrier and passivation layer use silicon dioxide, for its good thermal, electrical and chemical insulation capabilities. Materials like SiN and SiC have been used in industry inkjet cartridges because of similar properties, but SiO_2 is most easily implemented with our fabrication capabilities. The thin film heater consists of a Ti/Pt/Ti sandwich with

thickness around 40/200/40A. Pt is chosen because of its excellent thermal stability, which makes it a common heating element of MEMS devices. Ti is used as the adhesion layers to the top and bottom oxide. The total resistance of the layers is about 14ohm/square. The resistance value is chosen based on the total resistance of the interconnect lines.

3.2.4.2: One-dimensional heater operation simulation results

Control of the bubble actuation strength requires a thorough understanding of the heater's thermal behavior under various heating conditions. It is also important to achieve an optimum design of the heat barrier and passivation layer (the resistor itself is negligible since it is extremely thin, therefore imposing small thermal capacity). Because of the short time scale (micro-seconds) and small heater dimensions (tens of microns on a side), experimental measurement of heater temperature profile is difficult, and computer simulation is then the optimal tool to fulfill this task.

When a heating pulse is applied, the temperature distribution in an inkjet device is three-dimensional. However, achieving a uniform homogeneous nucleation on the heater surface requires that the heater dimensions be much greater than the thermal diffusion depth into the silicon and the fluid during the heating cycle. Since this condition is satisfied in our design (the heaters are all bigger than 20μm and the thermal diffusion depth is about 5μm), a one-dimension thermal diffusion simulation will sufficiently capture the main characteristics of the heating process.

The one-dimensional thermal diffusion equation along the vertical direction of a heater stack (line AB in Figure 3.8) can be expressed as:

$$\rho c \frac{\partial T}{\partial t} = \frac{\partial}{\partial x}(\kappa \frac{\partial T}{\partial x}) + \frac{\dot{P}}{V} \quad [3.2]$$

where α, ρ, c, V, P are the thermal diffusion coefficient, density, specific heat, volume and total power generated of each layer. Given the input voltage, heater size, resistance, and layer thicknesses, we could then numerically calculate the temperature distribution in the heater stacks.

We have firstly studied bubble nucleation behavior under different heating conditions. Figure 3.9 shows the temperature distribution in a heater stack with 2μm heater barrier layer and 0.7μm passivation layer when a heating pulse of 7V is applied. The heater dimension is 30x30μm. If we choose the fluid temperature for the bubble formation to be 300°C (the superheat limit of water), then the simulation result indicates that the bubble nucleation occurs about 5μs after the application of the electric signal. If the heating pulse is terminated immediately, the temperature profile in the fluid suggests that the heater transfers about 1.5μJ of thermal energy into the superheated fluid at its surface. The average thermal flux flow from the heater to the liquid is then 400MW/m^2, with the highest heater temperature around 470°C.

Similar simulation is also performed with a heating voltage of 13V. With increased heating voltage, which results in increased thermal flux, the bubble nucleation occurs in a shorter time, while the temperature profile in all layers becomes steeper, as shown in Figure 3.9(b). We have plotted the heating voltage vs. the required heating pulse width along with the corresponding heater temperatures, fluid thermal energy, and the percentage of total input heating power converted to fluid thermal energy (i.e. the heating efficiency) in Figure 3.10. We can see that with increased heating pulse width, the heater

driving strength is stronger (more fluid thermal energy results in higher bubble strength), the heater is less likely to break (due to lower heater temperature) and the heating becomes more efficient. Controlling heating pulse width is then an effective way to achieve optimum droplet generation condition. If we assume that the heater breaks at a temperature of 1100°C, then our simulation also shows that the heater cannot be operated above 20V with a 1μs pulse width, and above 10V with 5μs pulse width. These results are quite close to our experimental observation, which will be discussed in Chapter V.

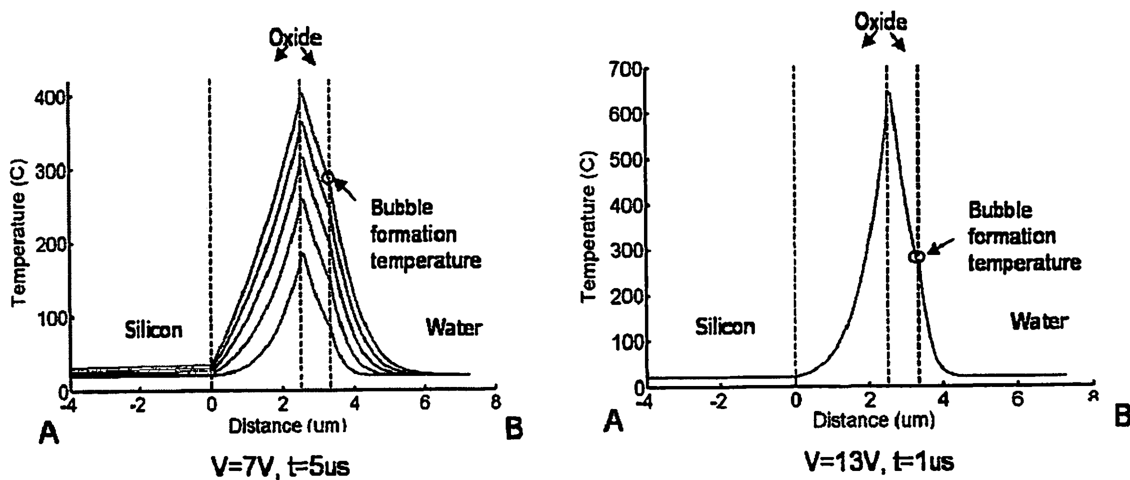

Figure 3.9: Temperature distribution in the substrate, heater and fluid during a heating cycle with different heating voltage amplitude. The curves are generated at 1μs interval.

From the simulation, we also found that the heat barrier thickness dramatically affects heater performance, and must be optimized. Thick heat barriers allow less energy to be lost to the substrate, therefore reducing the energy required for bubble nucleation, as shown in Figure 3.11. However, thick barriers also mean slower energy dissipation from the inkjet device. Since the residual thermal energy in the fluid and heater influences the total bubble actuation strength, a longer time interval is then necessary before next firing

cycle for stable droplet generation. We have simulated the heater cooling time (i.e., when the temperature is smaller than 50°C) with different heat barrier thickness using the one-dimensional thermal diffusion equation, with initial temperature profile set to be the one at the end of a previous heating cycle. The results are also plotted in Figure 3.11.

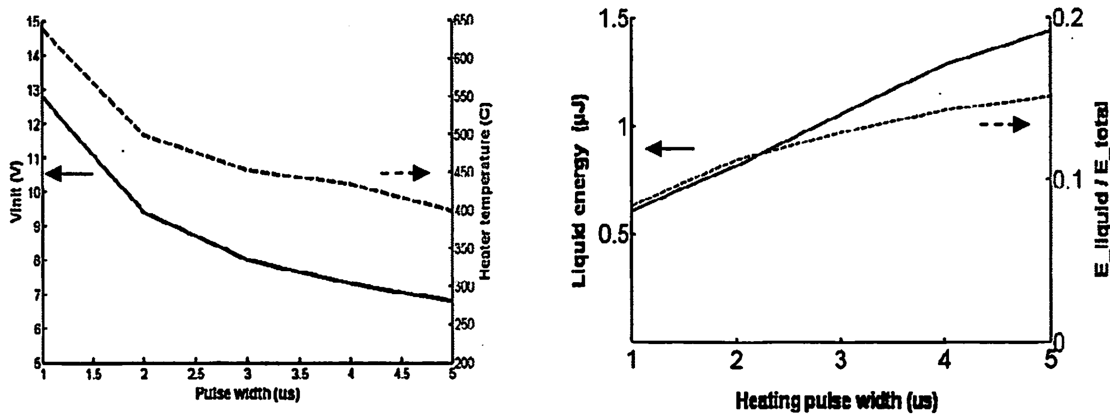

Figure 3.10: Heating voltage, heater temperature, fluid energy and the heating efficiency vs. the heating pulse width for heaters with 0.7μm SiO_2 passivation layer and 2μm SiO_2 heat barrier.

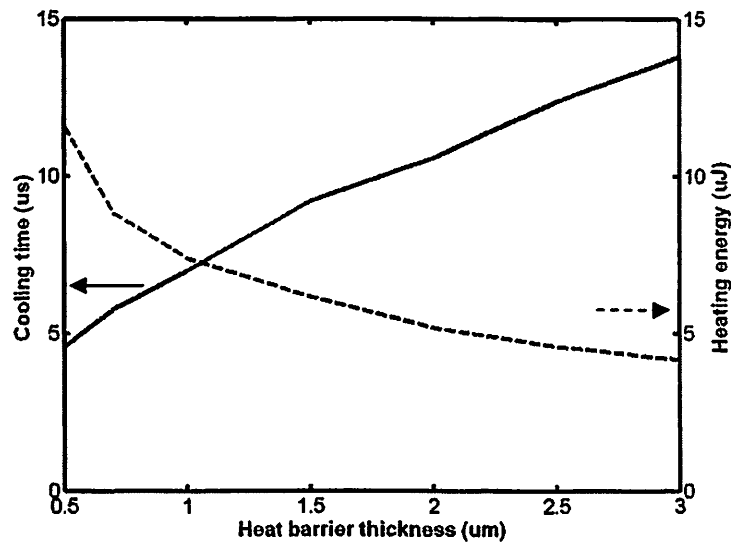

Figure 3.11 Heater cooling time and required heating energy vs. heat barrier thickness

From the plot, we can see that the heater cooling time is almost proportional to the heat barrier thickness, while the required heating energy flattens when the heat barrier thickness exceeds 2μm. Our design thus uses a heat barrier with a thickness of 2μm as the trade-off between the inkjet operation frequency and energy consumption considerations. With this thickness, the system cooling time is estimated to be approximately 10μs (the actual time can be longer if the substrate is not sufficiently cooled).

Passivation layer thickness is another heater parameter to be optimized. Thinner passivation layers is more thermally efficient (lower heating voltage with fixed heating time), as shown in Figure 3.11(b). The heater temperature is also lower. However, thinner passivation layers also mean worse electrical and chemical isolation of the heater surface. Since bubble collapse applies a large cavitation force to the heater surface, a thinner layer would also be less mechanically robust. In consideration of all these effects, an oxide passivation layer between 0.5-0.8μm is used in our inkjet devices.

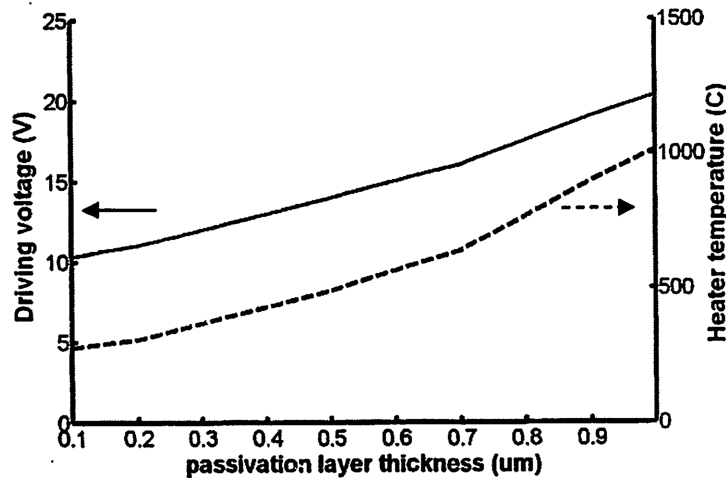

Figure 3.12: Driving voltage and heater temperature vs. passivation thickness

3.2.5 Nozzle design

The nozzle is also a critical part of an inkjet device, which determines the ejected droplet resolution and influences the device operation stability. Therefore it needs to be carefully designed. The nozzle should have a round shape and a smooth profile. Any irregularity of the nozzle shape would cause irregular droplet velocity and result in poor droplet position accuracy and pattern quality [12], which becomes more important as droplet size decreases. The droplet formation is also strongly affected by fluid wetting property. If the emerged fluid wets the area surrounding the nozzle asymmetrically, the unbalanced surface tension force will drag the droplet to one side and deflect it in that direction, as shown in Figure 3.13. Therefore our print head uses an anti-wetting coating outside the nozzle to increase the droplet generation stability. A thin Ni layer is used as the anti-wetting coating for water based printing materials because Ni has a stable, hydrophobic surface; its deposition process is also simple.

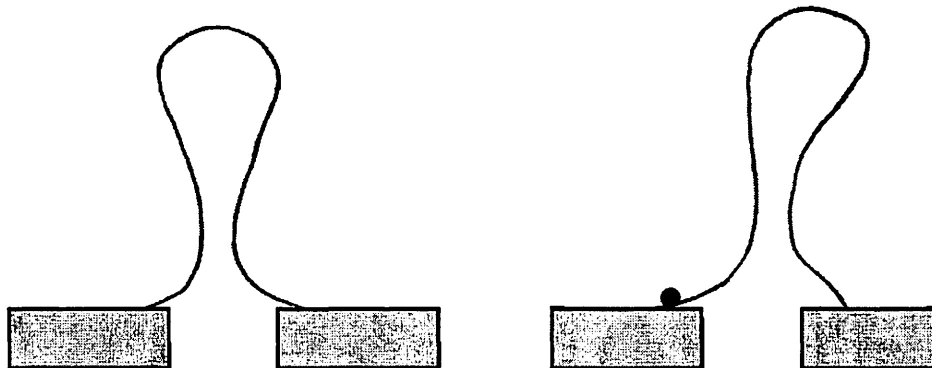

Figure 3.13: Influence of un-balanced wetting or irregular nozzle shape on droplet generation stability

According to our numerical simulation study in Chapter 2, a convergent-shaped nozzle will have smaller flow resistance hence a higher droplet resolution under the same actuation condition. The converging nozzle is thus used in one of our print head designs (refer to Chapter 4.1). However, forming a converging nozzle greatly increases the complexity of the print head fabrication when a sacrificial etching process is used (refer to Chapter 4.2). Our theoretical study in Chapter 2 shows that a cylindrical nozzle with a small aspect ratio will also have comparable performance; therefore it is implemented in our newest print head design. However, when the nozzle size decreases to the submicron scale, a nozzle with a small aspect ratio means an extremely thin nozzle membrane. Since the membrane strength scales with the 4th power of the film thickness, the thinner membrane will also be weaker. It then tends to bend under the high fluid pressure during liquid acceleration stage, and functions as a pressure buffer, which reduces the liquid velocity and momentum for droplet ejection.

Therefore, a well-shaped nozzle structure is used for our inkjet device, as shown in Figure 3.14. In this structure, the thin nozzle membrane is kept very small. The membrane thickness outside the nozzle area is increased in two steps, to a thickness of around 6-7μm. Since the membrane's strength scales with the 3rd power of its radius, this structure greatly increases membrane rigidity and prevents flexing. The steps are used to reduce the abruptness of the nozzle well, which makes it easier to pattern the nozzle by an etching process. This design is quite simple and can be easily integrated into our Ge sacrificial etching process (only an extra deposition and etching step is needed). The increased membrane rigidity can also help improve the robustness of the whole device structure and increase its operational lifetime.

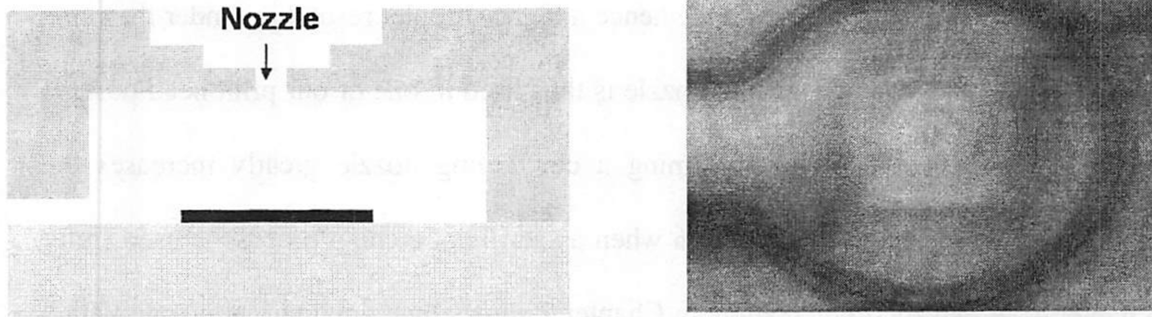

Figure 3.14: Left: schematic of the well-shaped nozzle in our print head. Right: a microscopic picture of a well-shaped nozzle in our test chip

3.2.6 Refilling channel design

The inkjet device is a two-ended system, with the nozzle as one end and the refilling channel as the other. As nozzle size decreases, its flow resistance increases. We should then design the refilling channel to match the nozzle's flow resistance, since a low resistive channel will result in a large volume of backflow, causing a faster bubble pressure drop and lower actuation strength for droplet ejection.

An impulsive inkjet model developed by Beasley [13] is used in our research to find the appropriate refilling channel size. This model treats the fluid as incompressible, and assumes that the flow in each channel section is a fully developed laminar flow at all times. In a reference channel (chosen here to be the main channel), the flow will be characterized by average acceleration **Ac** and average velocity **Vc.** The real channels are then replaced with equivalent channels, each with the same average velocity and acceleration as the reference channel. The assigned equivalent damping coefficients for inertial **(Mi)** and viscous **(Bi)** will match the overall pressure drop of the actual channels, and can be expressed as:

$$M_i = \rho A_c \int (A_c / A_i(x)) dx_i \qquad [3.6]$$

$$B_i = \eta v_c \int (G_i(x) A_c / A_i^2(x)) dx_i \qquad [3.7]$$

where A_i and A_c are the cross-sectional area of the channel and reference channel, and $G(x)=8\pi$ for a circular channel, $G(x)=12(0.33+1.02(z+z^{-1}))$ for a rectangular-shaped channel, and z is the channel aspect ratio.

Given the above definitions, the following flow equations govern the liquid flow during the bubble growth stage:

$$M_n \frac{d^2 Q_n}{dt^2} + B_n \frac{dQ_n}{dt} = P_b - (P_{atm} + 2\sigma / r_{nozzle}) \qquad [3.8]$$

and

$$M_r \frac{d^2 Q_r}{dt^2} + B_r \frac{dQ_r}{dt} = P_b - P_{rev} \qquad [3.9]$$

where M_n, M_r, and B_n, B_r, are the equivalent inertial and viscous damping coefficients of the nozzle and refilling channels. Here, note that the B_n and M_n should also include the liquid column that has been pushed out through the nozzle, as shown in Figure 3.15(a). Q_n and Q_r are the flow volume through the nozzle and refilling channel respectively, and $2\sigma/r$ is the surface tension force. We can then express the governing equations of fluid flow during the chamber refilling and damping stage as:

$$(M_n + M_r) \frac{dV}{dt^2} + (B_n + B_r) \frac{dV}{dt} = 2\sigma / r_{meniscus} \qquad [3.10]$$

$$r_{meniscus} = \frac{r^2_{nozzle} + y^2}{2y} \qquad [3.11]$$

y is the distance from the nozzle plane to the meniscus lowest position.

The design of an inkjet device with high bubble actuation efficiency should ensure that the flow volume is much smaller through the refilling channel than that through the

nozzle. However, highly resistive refilling channels extend the chamber refilling time, which decreases the inkjet operation frequency. Therefore, we have designed the refilling system based on a simple criterion:

$$Q_n/Q_r>=2 \quad [3.12]$$

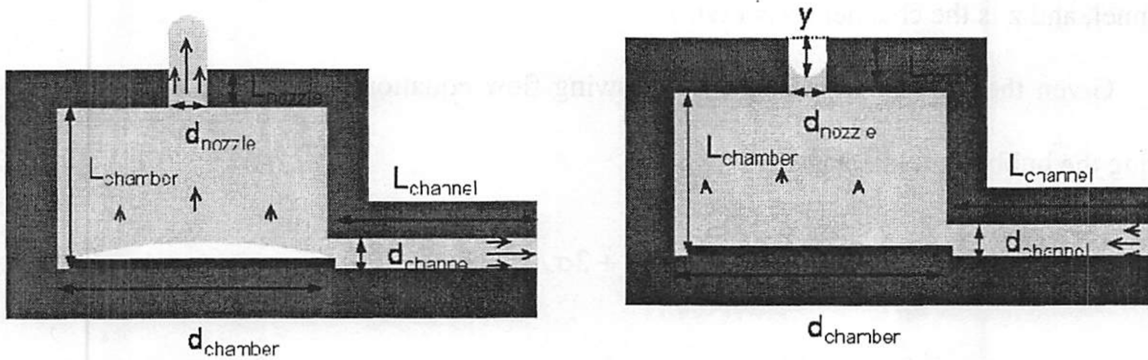

Figure 3.15: Schematic of laminar liquid flow during droplet ejection (left) and chamber refilling (right) stage

Equations 3.8 and 3.9 have been numerically calculated with a square-shaped pressure pulse with Po=1MPa and t_o=0.1μs for nozzles with diameter between 1.5 and 5μm and thickness of 1μm. The refilling channel lengths are chosen to match the liquid volume flow through the nozzles, as expressed in equation 3.12. The refilling channel is assumed to be square–shaped, with depth of 5μm (value chosen from fabrication requirements). Figure 3.16 plots the required minimum channel length vs. the nozzle dimension with different channel width. A narrower channel requires shorter length and then saves the device area. For fabrication simplification, all the refilling channels in our print head have a length of 100μm and width of 20μm.

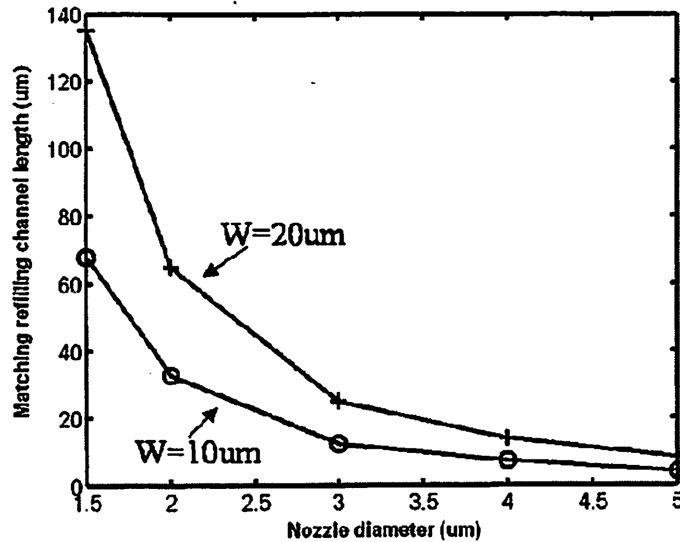

Figure 3.16: Required minimum channel length vs. the nozzle diameter

Using equations 3.10 and 3.11, we have also studied the chamber refilling and meniscus damping behavior. We assume that the refilling occurs when the liquid flow retracts back into the channel the same length as droplet radius, and the liquid velocity is zero at the beginning. These assumptions may not be accurate, but they are sufficient to provide a rough idea of the time scale for chamber refilling and meniscus damping. The meniscus position vs. time is plotted for inkjet devices with nozzle aspect ratio of 1:1 and nozzle diameters of 5μm, 2μm, 1μm and 0.5μm, respectively, in Figure 3.17. The refilling channels have fixed lengths of 100μm and areas of 5x20μm^2. The plot shows that the liquid refilling and damping time decreases as nozzle size decreases, due to the increase of the liquid surface tension and viscosity forces. The time is about 20μs for 5μm nozzles, and smaller than 0.5μs for 1μm nozzles. Compared with the heater cooling time (>10μs), the chamber refilling and meniscus damping then have negligible influence

on inkjet device's operation frequency when the targeted droplet size is in micron to submicron scale.

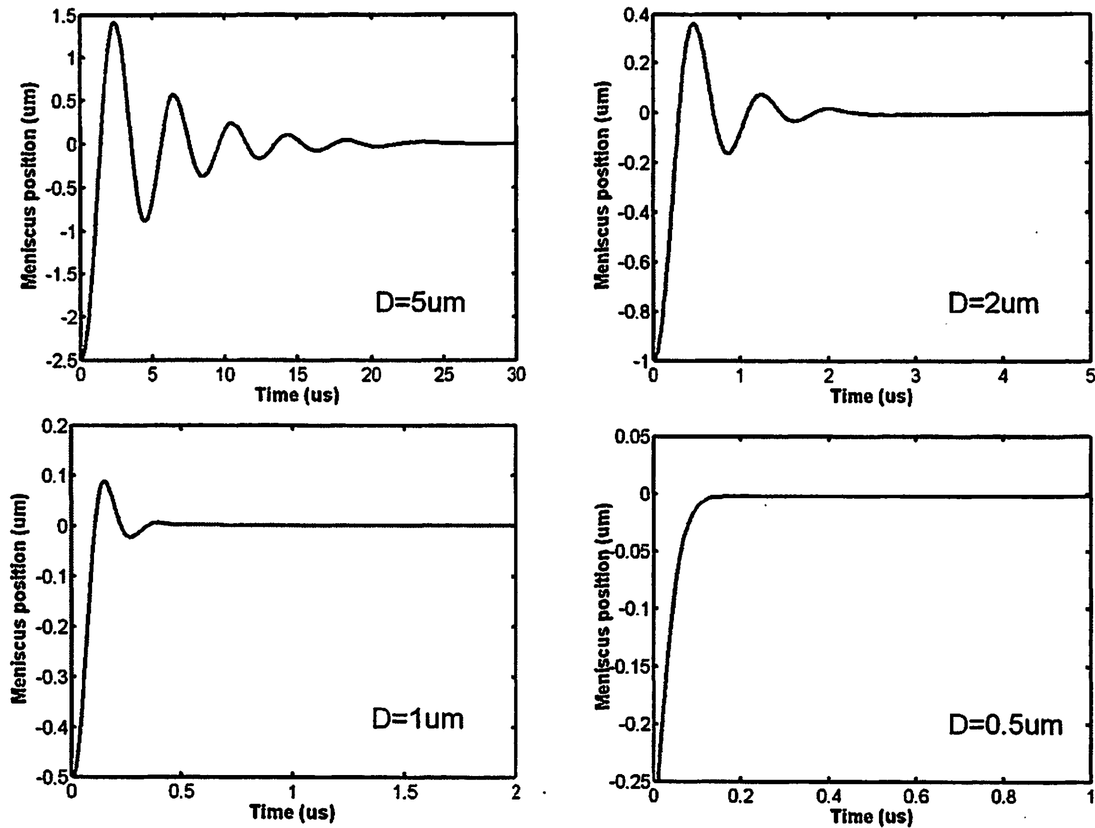

Figure 3.17: Inkjet refilling and meniscus damping behavior of different nozzle dimensions

3.2.7 Design of the inkjet chambers

During both the droplet generation and chamber refilling phases, liquid flows very slowly inside the inkjet chamber, because of its large dimensions. Therefore, the inkjet chamber size has a negligible influence on both the droplet resolution and repetition rate if an incompressible fluid model is considered. This is confirmed through our numerical simulation using CoventorWare. However, the actual fluid inside inkjet device is compressible, especially under a pressure as high as the initial bubble nucleation

pressure. The pressure pulse actually propagates through the inkjet chamber as an acoustic wave. When an acoustic wave propagates through a small tube, the wave magnitude decreases with the propagation length according to the equations

$$P(x) = P_o e^{-\alpha x} \qquad [3.13]$$

$$\alpha = k \frac{1}{2R} \sqrt{\frac{2\mu}{\varpi\rho}} \qquad [3.14]$$

where k, R, μ, ϖ, and ρ are the wave vector, the tube radius, the fluid viscous coefficient, angular frequency, and mass density, respectively [14]. In a small tube, the attenuation constant is proportional to the square root of the frequency and inversely proportional to the chamber radius, in contrast to the square power dependence on the frequency in free space. For a thermal bubble inkjet device, the peak pressure of the bubble actuation is around 4MPa and the characteristic time scale under high pressure is about 0.05μs (refer to section 3.1.2), so the characteristic frequency of the bubble actuation pressure wave is about $2E7s^{-1}$. In our print head, the chamber diameter is kept just slightly larger than the heater size to minimize the device area. The calculated attenuation constant is α~1E4/m for an inkjet chamber with a radius of 30μm, so the pressure magnitude drops by half in every 65μm of channel length. To maintain a high actuation pressure at the nozzle, shallow inkjet chambers around 5-10μm deep are then used in our print head. The chamber depth is also chosen for ease of fabrication with a sacrificial structure etching process.

3.3 Summary

In summary, in our research, we have designed a DOD inkjet print head for high resolution patterning applications based on thermal bubble inkjet printing theory. Our print head has unique advantages over other thermal bubble inkjet systems:

1. The thin-film heater is designed for high thermal stability, high energy transfer efficiency and short cooling time (<20μs).
2. Thin nozzles reduce liquid flow resistance; small nozzle membranes increase strength and prevent flexing.
3. Optimized refilling channels provide high bubble actuation efficiency and small chamber refilling time and liquid damping time (<1μs for micron scale nozzles).
4. Small, shallow chambers minimize pressure lost in the fluid media; individual feeding holes eliminate crosstalk.
5. Thick chamber walls improve structural robustness and ensure long device operational lifetime.
6. A small device area allows large device arrays and high printing throughput.

According to our numerical simulations, such a thermal bubble inkjet print head can generate water droplets as small as **0.5μm**; its operation frequency, which is mainly limited by the heater cooling time, could be as high as **30KHz**. The device area could be smaller than 80x200μm with 50μm feeding holes, 50μm refilling channels and 60μm inkjet chamber. So up to **5x10^{5}** devices can be densely packed on a 4 inch wafer. As we discussed in the previous sections, due to the complexity of the bubble formation process and the limitations of our models and numerical tools for the study of the droplet generation, we must rely on experimental results to confirm the droplet size limit and to

investigate the main factors that will influence the printing process. Therefore, fabrication of the high resolution inkjet print head designed in this chapter is the focus of our research. This work will be presented in the following chapter.

Reference

1. F. C. Lee, "PZT printing applications, technologies, new devices," in *Proc. Ultrasonic Symposium*, pp. 693–697, 1988.

2. S. Aden, J. Bohörquez, D. Collins, D. Crook, A. García, and U. Hess, "The third-generation HP thermal inkjet print head," *Hewlett-Packard J.*, vol. 45, pp. 41–45, 1994.

3. S. Kamisuki, T. Hagata, C. Tezuka, Y. Nose, M. Fujii, and M. Atobe, "A low power, small, electrostatically-driven commercial inkjet head," in *Proc. IEEE Micro Electro Mechanical Systems*, Heilderberg, Germany, pp. 63–68. 1998.

4. D, Huang, E.S. Kim, "Micro-machines acoustic wave ejector" *Journal of Microelectromechan. Sys.*, vol.10, pp.442-449, 2001.

5. Allen, R.R., Meyer, J.D., and Knight, W. R. "Thermodynamics and hydrodynamics of thermal ink jets," *Hewlett-Packard J.*, pp. 21–27, 1985.

A. Asai, "Bubble dynamics in boiling under high heat flux pulse heating," *Transactions of the ASME. Journal of Heat Transfer,* vol.113, No. 4, p.973-9, 1991.

A. Asai, "Three-dimensional calculation of bubble growth and drop ejection in a bubble jet printer," *J. of Fluids Eng. Trans. of the ASME,* vol.114, no.4, pp.638-41, 1992.

6. J. Chen, K. D. Wise, "A high-resolution silicon monolithic nozzle array for inkjet printing," *IEEE Tran. Elec. Dev.*, vol. 44, no. 9, pp1401-09, 1997.

7. F.G. Tseng, C.J. Kim, and C.M. Ho, "A high-resolution hgh-frequency monolithic top-shooting microinjector free of satellite drops" *Journal of Microelectromechan. Sys.,* vol.11, pp.427-447, 2002.

8. P. Krause, E. Obermeier, and W. Wehl, "Backshooter—a new smart micromachined single-chip inkjet print head," *in Tech. Dig. 8th Int. Conf. Solid-State Sensors and Actuators,* pp. 325–328, 1995.

9. Eldurkar V., Aden, J.S., "Development of the thin-film structure for the thinkjet print head," *Hewlett-Packard J.*, pp. 27-33, 1985.

10. M. Doring, "Ink-jet printing", *Philips Tech. Rev.,* vol. 40, pp192-198, 1982.

11. Beasley JD. "Model for fluid ejection and refill in an impulse drive jet,"*Photographic Science & Engineering,* vol.21, no.2, pp.78-82, 1977.

12. L. Elvira-Sagura, "Acoustic wave dispersion in a cylindrical elastic tube filled with a viscous liquid", *Ultrasonics*, vol. 37, pp537-547, 2000.

CHAPTER IV

PRINT HEAD FABRICATION

As discussed in the previous chapters, an inkjet print head built for the maskless lithography purpose would require millions of devices with integrated controlling circuits for high patterning throughput. The inkjet nozzles would have extremely small sizes (micron to deep sub-micron) and smooth shapes for stable, high resolution droplets generation. The dimensions of the inkjet chambers, heaters, and refilling channels would all need to be defined precisely, for high operation frequency and ease of droplet ejection. The only approach that could fulfill such requirements is one that takes advantage of state of the art silicon micro-machining technology.

Our research has employed two micro-machining processes to fabricate the high resolution thermal bubble inkjet print head designed in the previous chapter. This work was done in the Microfabrication Laboratory (Microlab) [1] of the EECS department, UC Berkeley, an advanced micro-fabrication facility at the university level. We attempted to form the inkjet devices with both a wafer-to-wafer eutectic bonding method and a Ge sacrificial structure etching method. The second process is more successful, producing a high device yield and an optimized device structure, and is thusly the focus of this chapter.

4.1 Wafer-wafer bonding processes

MEMS researchers most commonly use the wafer-wafer direct bonding method to form micro-fluidic structures [2-7]. This is also our first choice for fabricating a monolithic thermal bubble inkjet print head with high device density. The main process steps are shown in Figure 4.1. In this process, 2μm Low Temperature Oxide (LTO) is firstly deposited as the heat barrier on a 4 inch silicon wafer (the bottom wafer), as shown in Figure 4.1(a). Then, a magnetron sputtering and liftoff process deposits and patterns a Ti/Pt/Ti heater stack approximately 10/40/10nm in thickness. 0.4μm thick Cu interconnect lines are also formed using e-beam evaporation and another lift off process (Figure 4.1(b)). Afterwards, LTO around 2μm thick is deposited on top of the heater (Figure 4.1(c)) and a Chemical Mechanical Polishing (CMP) process flattens the wafer surface for the following bonding step. Through precise control of the wafer polish time, the process stops just when the final oxide layer thickness above the heater decreases to about 0.7μm (Figure 4.1(d)). The oxide is then etched to expose the Cu bonding pads (Figure 4.1(d)).

On another double-polished silicon wafer (the top wafer), 6μm phosphorus doped oxide (PSG) is deposited (Figure 4.1(e)). Of this, 4μm PSG is etched away using 5:1 Buffered Hydrofluoric Acid (BHF) to form a curved dummy structure for the inkjet nozzle (Figure 4.1(f)), leaving 2μm PSG to perform as an etch stopper of a later through-wafer etching process. Then 2.5μm low stress nitride is deposited as the nozzle membrane, which is dry etched to open the small nozzles ((Figure 4.1(g)). During this step, precise alignment is required to place the nozzle directly in the center of the dummy structures, forming a symmetrical shape. Afterwards, the nitride layer

on the back side of the double-polished wafer is etched away, and the leftover oxide (about 2μm) is patterned as the etching mask of the liquid-delivering pipes and channels (Figure 4.1(h)). A two-step Deep Reactive Ion Etching (DRIE) process then forms the inkjet chamber and channels. Firstly, using a thick photoresist mask, the wafer is etched through, opening the inkjet chambers, and the etching stops at the oxide barrier layer. Once the photoresist hard mask is removed, we use the pre-patterned oxide mask to etch flow channels and liquid-delivery pipes approximately 30μm deep into the wafer (Figure 4.1(i)). The pre-patterned oxide mask is necessary because the photoresist spinning process cannot cover the edges of the deep etched features.

The double polished wafer is then etched in BHF to get rid of the oxide dummy structures. A smooth nozzle with a converging shape is then opened, and a fresh surface of silicon is exposed on the other side of the wafer, to make it ready for the bonding process. A Ni eutectic bonding method (which will be discussed in the following section) joins the top and bottom wafers, forming the liquid flowing channels and chambers. The final print head structure is shown in Figure 4.2. The through-wafer etching step that forms the inkjet chambers actually also opens the liquid-feeding and wire-bonding holes, but due to their large dimensions (>400μm), the whole top membrane is etched through much more quickly.

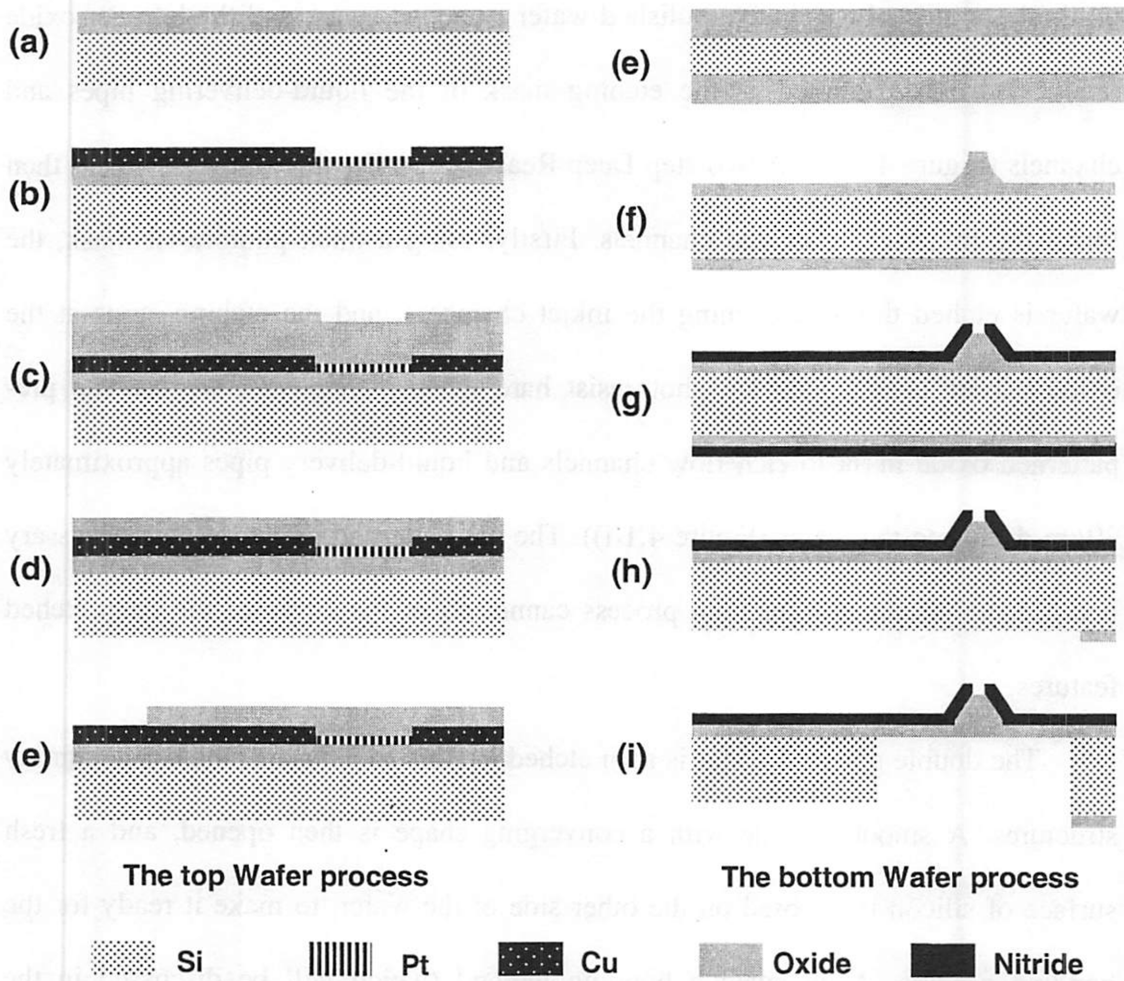

Figure 4.1: The top and bottom wafer process flow for print head fabrication using the wafer bonding method

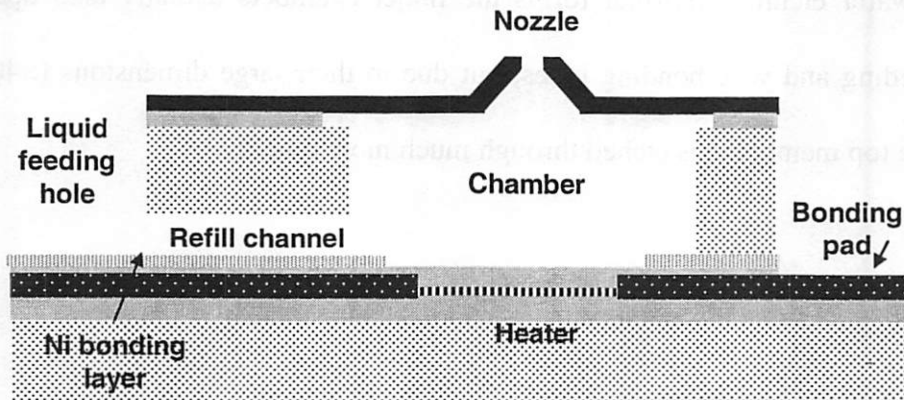

Figure 4.2: Final thermal bubble inkjet print head structure using the wafer bonding method (could compose array of devices)

The most critical step in this print head fabrication process is the wafer-wafer bonding. Our research investigated and tested many existing wafer bonding methods, including Si-Si thermal direct bonding [2, 3], plasma-enhanced low temperature bonding [4], adhesive layer bonding [5, 6], metal eutectic bonding [7, 8] etc. However, the thermal direct bonding method requires maintaining a bonding temperature of as high as 1000°C for hours, which causes the thin nitride nozzle membranes to break due to the high thermal stress. Plasma-enhanced bonding works at much lower temperatures (around 300°C) by activating the surface bonds using plasma treatment, but requires an extremely clean, smooth surface and is therefore very sensitive to wafer cleaning procedures and the surrounding environment, resulting in an unacceptably low yield. We also tested adhesive bonding approach by using a stamping method to apply epoxy to the top wafer's extruded surfaces, as illustrated in Figure 4.3(a). However, the adhesives tend to reflow during the curing cycle after wafer alignment, clogging the small refilling channels, as shown in Figure 4.3(b). Despite all these failures, we have finally found a reliable bonding approach: the Si-Ni eutectic bonding technique.

In this method, an e-beam evaporation system deposits a 40/300nm Ti/Ni intermediate layer on the bottom wafer (Ti is used for adhesion to the oxide surface), except for the tops of the heaters, where the nucleation will occur (the heaters are protected by a photoresist mask). The bottom wafer is then aligned and pressed against the top silicon wafer inside a nitrogen chamber, with an ambient temperature of approximately 400°C and a bonding stress of 2PSI for 2 hours. Ni silicide forms at the Si-Ni interface in this temperature range, resulting in a strong bond between the top and bottom wafers. Such a Si-Ni bonding interface is shown in Figure 4.4. The bonding yield

is quite high, since Ni and Si interfuse with each other quickly and the process does not require an extremely smooth wafer surface; the wafers do not delaminate when the wafer pair is cut into small chips. Figure 4.5(a) shows an array of inkjet chambers and refilling channels formed by the wafer bonding process; the cutting process has broken the top membranes in this picture. Figure 4.5(b) is a close-up view of a heater at the bottom of an inkjet chamber, with a refilling channel in the background. We can see that the Ni does not cover the heater surface. The top view of a 5μm round nozzle opened on a nitride top membrane is shown in Figure 4.5(c); Figure 4.5(d) illustrates the nozzle's smooth inner profile, formed by the dummy etching process.

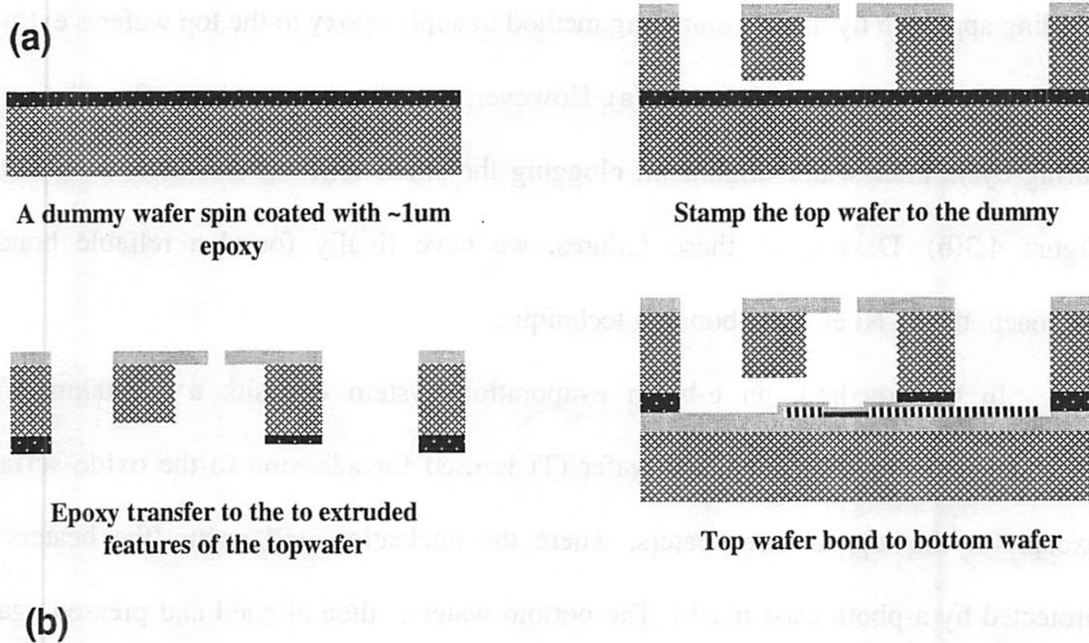

Figure 4.3: The epoxy stamping bonding method. (a) Process flow; (b) bonding result

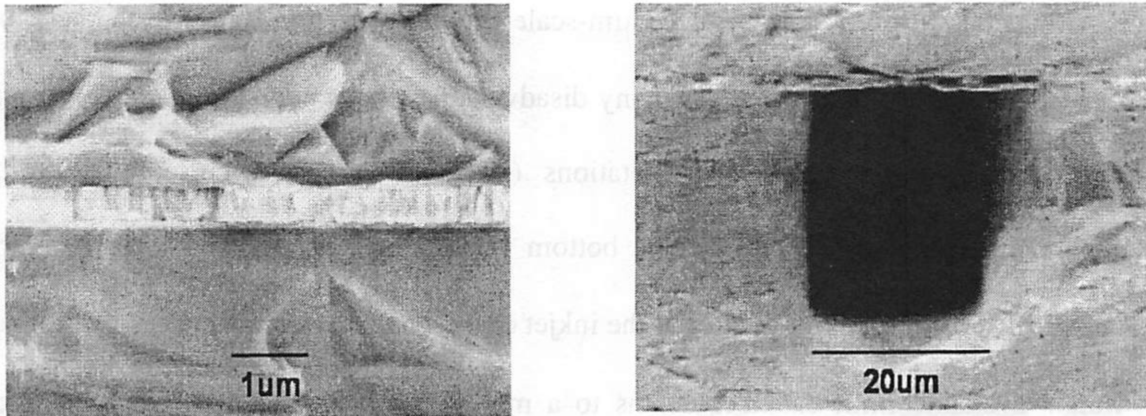

Figure 4.4: (a) Ni silicide interface formed by Ni-Si eutectic bonding method; (b) a liquid refilling channel formed by Ni-Si eutectic bonding method

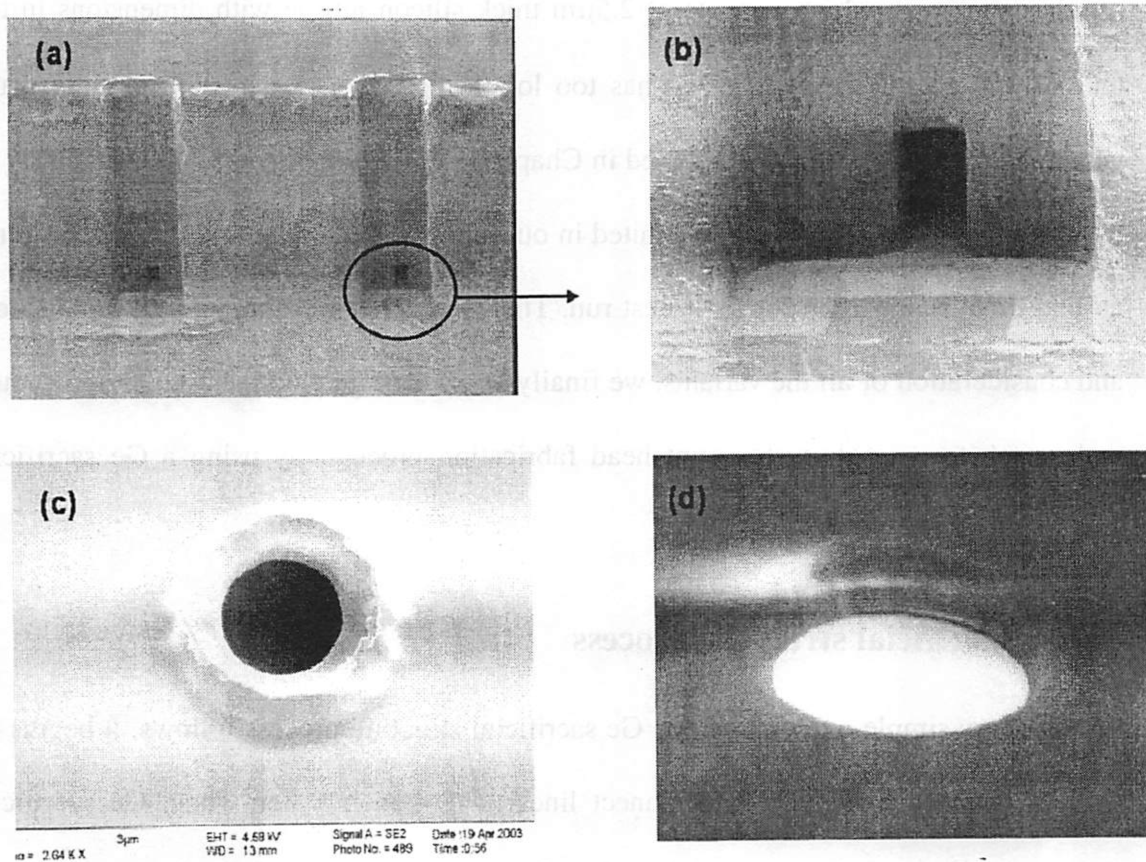

Figure 4.5: (a) Array of Liquid refilling channel formed by Ni-Si eutectic bonding method; (b) close up view of a heater; (c) top view of an inkjet nozzle; (d) nozzle inner surface

Even though wafer-wafer bonding process successfully demonstrated an experimental system that generated 5μm-scale droplets (refer to the next chapter), our theoretical study shows that it has many disadvantages when attempting smaller droplet dimensions. Firstly, equipment limitations (*KSBonder* in the Microlab) make the alignment error between the top and bottom wafers in the bonding process too large (around 15μm) for precise control of the inkjet chamber size. Moreover, even the thinnest wafers available limit chamber depths to a minimum of about 50μm. Our theoretical study indicates that acoustic pressure loss, and therefore difficulty in droplet generation, increases with chamber depth, so we always prefer shallower chambers. In addition, the nozzle membrane, which is made of 2.5μm thick silicon nitride with dimensions in the tens of microns, is too fragile and has too low a resilience to the high pressure wave generated by the actuator, as discussed in Chapter 3. Most importantly, the availability of the bonding process equipment is limited in our fabrication facility, and the process turn-around time is very long for every test run. Therefore, after careful study of this process and consideration of all the variants, we finally decided to give up the bonding procedure and switch to a single-wafer print head fabrication process, by using a Ge sacrificial structure etching method.

4.2 Ge sacrificial structure process

A very simple overview of the Ge sacrificial structure process follows. It begins by forming Pt heaters and Cu interconnect lines on a 4 inch wafer. Then, Ge sacrificial structures, representing the inkjet chambers and refilling channels, are formed. Afterward, oxide deposition creates chamber walls and nozzle membranes, and etching the wafer from the back side opens the fluid flowing holes. Hydrogen peroxide (H_2O_2)

can then remove the Ge sacrificial structures, opening the inkjet chambers and channels. Since hot H_2O_2 etches Ge very quickly, and its selectivity to Si and SiO_2 is almost infinite, the etching step has no influence on the deposited inkjet structures [8]. The final step opens the nozzles by plasma etching.

To ease understanding of the detailed process flow and also to allow following researchers to replicate the process run, the following sections break down the process into small, clearly defined steps. Each step contains the technical procedures and the process parameters (in the "details" portion) derived from our most recent recipe of our process run in Microlab (Spring 2004), as well as a discussion of its advantages and technical difficulties. The steps will also be grouped by common purpose, and an illustration of an inkjet device's cross section after each step will precede each group. The corresponding mask layout of the device is shown in Figure 4.6.

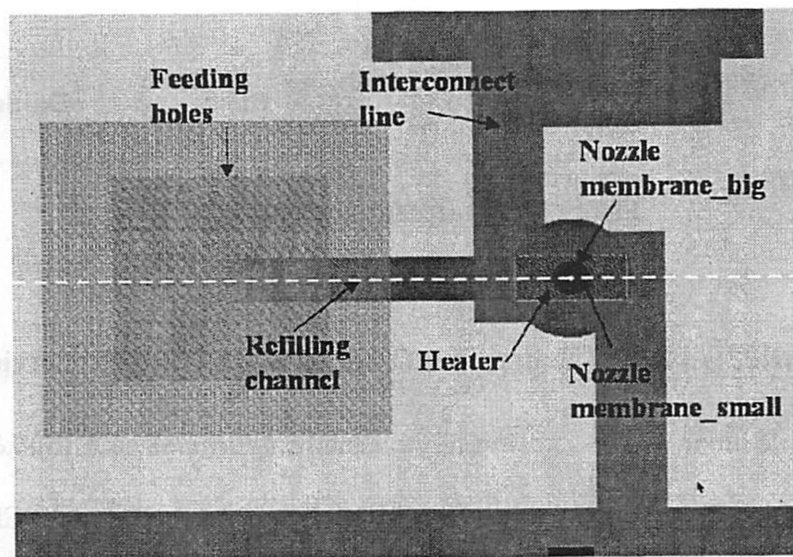

Figure 4.6: Layout of a single inkjet device for the Ge sacrificial etching process

4.2.1 Detailed process flow of the single wafer print head fabrication process

A: Heater formation:

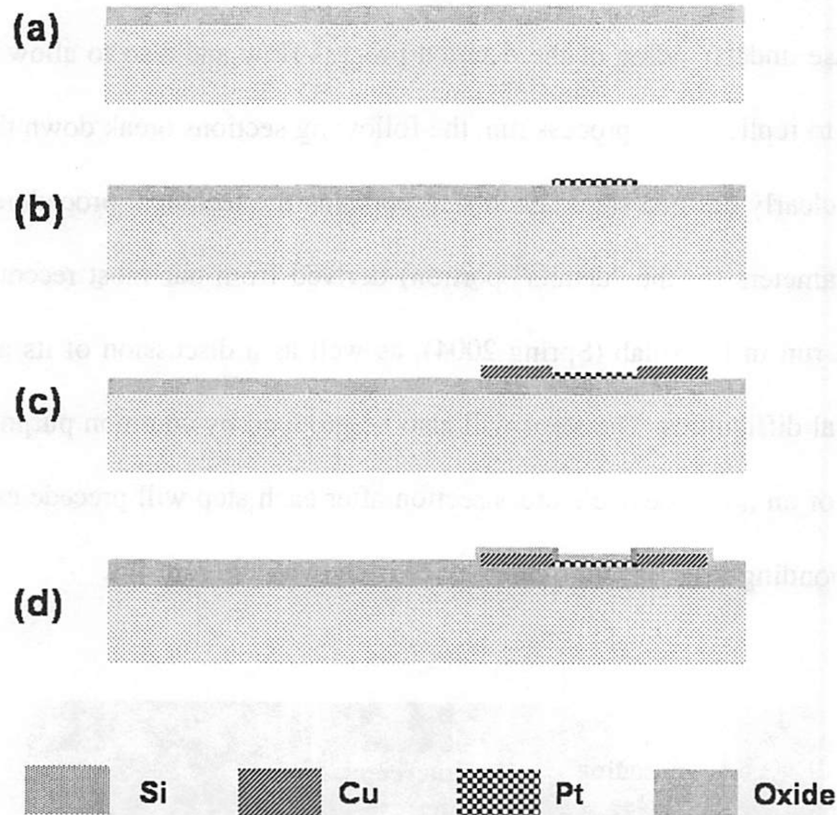

Figure 4.7: Heater formation process flow

Step 1: Deposit 2μm Low Temperature Oxide (LTO) as the heat barrier –Fig. 4.7(a)

Details: Silicon wafers are initially cleaned in *Piranha* bath (*Sink8* in *Microlab*), and then loaded in *Tystar12*, the Non-MOS clean Low Pressure Chemical Vapor Deposition (LPCVD) furnace; the *12SULTOA* program performs deposition at a temperature of 450°C, with 120sccm SiH_4 and 90sccm O_2 flow. The process pressure is 300mtorr and the total deposition time is around 2 hour 20 min.

Step 2: Deposition and patterning of the heater structures—Fig. 4.7(b)

A. Formation of the photoresist mask for heater lift-off process

Details: *Svgcoat1* spin-coats 2.8μm of *I-line* photoresist onto the wafers, and *Ksaligner*, a contact lithography tool, exposes the resist. The exposure time is about 7s at 28mw/cm^2 UV light intensity. The wafer is then soaked in chlorobenzene for 10-15min and developed with *Microdep5740* in *Svgdev* for 120s.

Discussion: The chlorobenzene process is chosen to form sloped sidewalls of the photoresist pattern, contributing to the easiness of the liftoff process of Pt heaters.

B. Sputter deposition of Ti/Pt/Ti layer

Details: *Randex*, a magnetron sputtering system, deposits a metal multilayer; the sputtering energy is 100W with Ar flow rate of 120sccm. Using a continuous rotating mode of the substrate, we get about 5nm Ti layer after 5min of deposition, and around 40nm Pt layer after 25min of deposition.

Discussion: Continuous rotation is necessary to reduce the wafer temperature during metal deposition. This prevents burning of the photoresist and degradation of the photoresist sidewall, which will cause bad photoresist lift-off results and excessive metal on the edge of the patterns. An example is shown in Figure 4.8(a).

C. Lift-off process

Details: Immersing the sputtered wafers in acetone and placing them in an ultrasonic bath completely strips away the underlying photoresist layer, leaving the patterned Pt heater structure.

Step 3: Deposit and patterning Ti/Cu/Ti interconnect lines—Fig. 4.7(c)

Details: Photoresist patterns are formed using the same process as in step 2-A.The machine *Edwardseb3*, an e-beam evaporation system, deposits the metal layers. The Ti layers are deposited with an e-beam gun current flow of 80Amp, and a deposition rate of 0.1nm/s; to form a good adhesive layer, the Ti layers must be thicker than 10nm. The Cu layer is deposited at 50Amp current with deposition rate around 0.07nm/s (with a higher current and deposition rate, the Cu source will spill out of the crucible); the target thickness of the Cu layer is about 400nm. Since the Cu deposition rate is slow, we prevent photoresist burning, by stopping the Cu deposition process every 25min, allowing the machine and the silicon substrate to cool. The Cu lines are then formed using the same lift-off process described in step2-C.

Step 4: Deposit 0.8um LTO as passivation layer—4.7(d)

Details: The deposition process is exactly the same as step 1, with deposition time set to be 55min. Because the wafers already have metal layers on their tops, they can no longer be cleaned in a *Piranha* bath before being loaded into the furnace; they must be cleaned in acetone, and then rinsed in DI water and spin dried.

Figure 4.8 shows the microscopic pictures of the heater and the Cu interconnect structure following the above steps. The heater sizes vary from 20μm to 50μm, according to our design, and the Cu interconnect lines are about 250μm wide, to match the resistance of the heaters. The square-shaped Pt heater has a resistance of approximately 14ohm, and the total resistance between the ground line and a Cu pad is about 24-26ohm, according to a four-probe-station measurement.

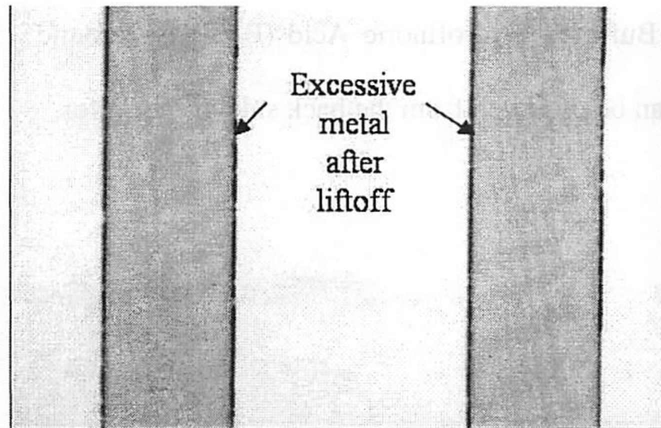

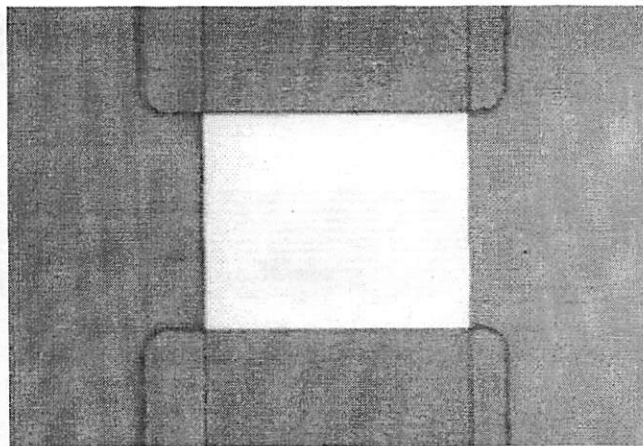

Figure 4.8: (a) Cu lines formed using lift-off process with photoresist burning; (b) top view of a Pt heater formed by lift-off process.

B: Forming Ge sacrificial structures of the inkjet chambers and refilling channels

Step 5: Remove the oxide layer on the top of the feeding holes—Figure 4.9(a)

Details: The oxide on the top of the feeding holes must be etched to provide direct contact between the Ge dummy structures and the silicon. After the wafers are patterned with photoresist using the mask *"Oxide"* (typical photoresist processes will do), they are

wet etched in 5:1 Buffered Hydrofluoric Acid (BHF) for around 15min; the complete removal of oxide can be observed from the back side of the wafer.

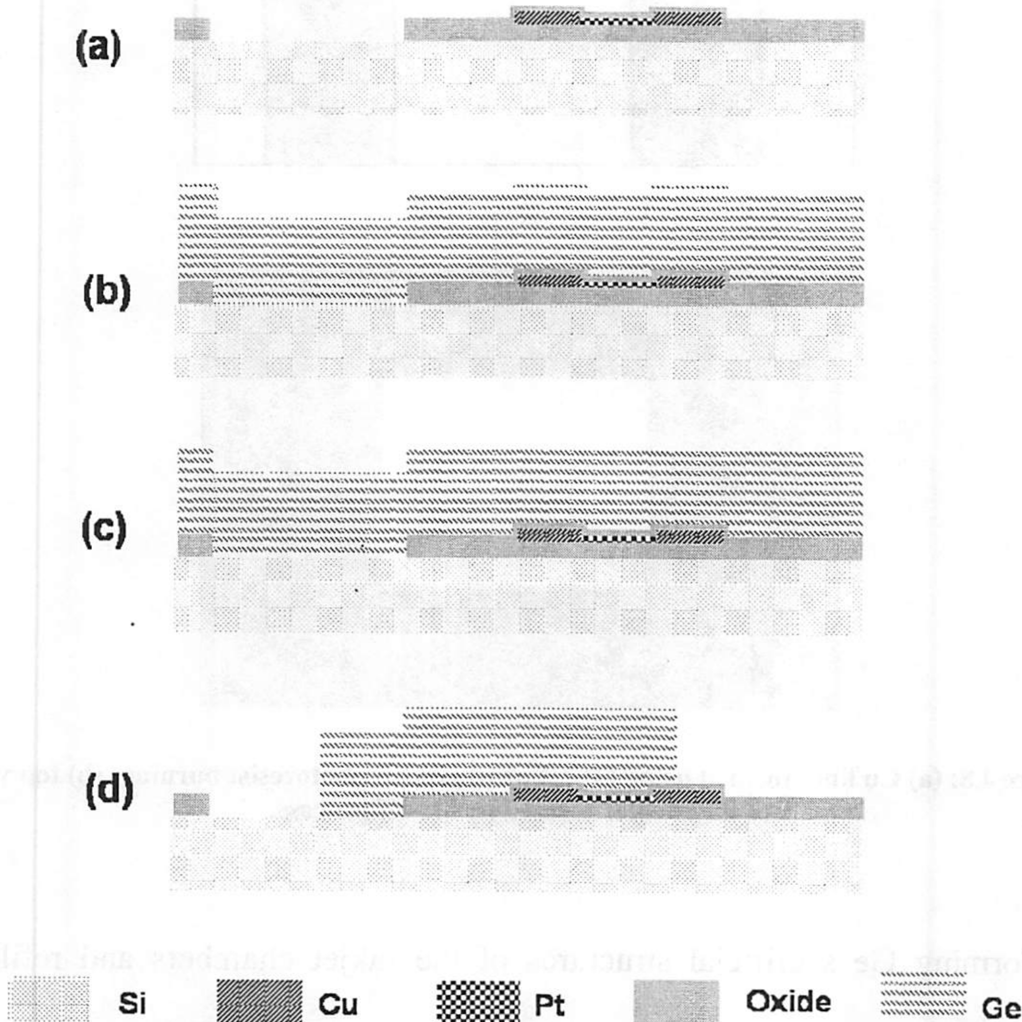

Figure 4.9: Ge sacrificial structure formation process flow

Step 6: Deposit Ge dummy layer--- Figure 4.9(b)

Details: This process is performed with *Tystar20*, a Non-MOS clean Ge deposition furnace, using program *SIGEVARB.020*. A Si seed layer is initially formed on the oxide

with 200sccm Si_2H_6 flow, 425°C temperature and 400mtorr pressure for 5 minutes. An un-doped Ge layer, with a target thickness of 5μm, is then deposited with 100sccm Ge_2H_6 flow, 375°C temperature and 600mtorr pressure, over the course of 6 hours.

Step7: Flatten the Ge surface using a Chemical Mechanical Polishing (CMP) process -- Figure 4.9(c)

Details: Due to the poly-crystal structure, the surface of the deposited Ge layer is quite rough and must be smoothed to prevent the formation of irregular inkjet nozzles. The wafers are processed using machine *CMP* and recipe *oxide.std.00*, with a Ge polishing rate of about 80nm/min. The wafers need to be rotated 90° every 60 seconds during polishing to achieve a uniform Ge removing rate across the wafers. Typically, polishing must continue for 6-8min before a smooth Ge surface can be observed. The wafers are then cleaned by being soaked in ammonia, rinsed with DI water, and brushed at the same time with a sponge to remove the slurry.

Step 8: Pattern Ge layer as the dummy structures-- Figure 4.9(d)

Details: MicroChem's *STR5740* photoresist is coated on wafer at a spinning rate of 3000rpm; the final resist thickness is around 8μm. The wafers are then exposed in *Ksaligner* for 10s with mask *"Chamber"*, and developed in MicroDev developer for about 2min. After 2 hours of hard-baking the photoresist mask, we etch the wafers in *Lam5* using recipe *5001*, with HBr/Cl_2 gas flow rate of 150/50sccm and 300W forward power. The etching rate is around 0.9μm/min, and approximately 360 seconds of etching are required to remove the 5μm Ge layer with 10% over etch.

Discussion: The thick photoresist is chosen to provide a better step coverage on the edge of the oxide holes for the Ge dummy structure. The photoresist mask in contact with the Ge sacrificial structures cannot be removed by a *PRS3000* bath, since the bath will react with Ge and make the dummy structure surfaces rough. The photoresist mask can only be etched with acetone or oxygen plasma (*Technics-c*, ~30min at 300W).

A patterned Ge dummy structure is shown in Figure 4.10. We can see that, due to the CMP process and the special care taken in removing the photoresist etching masks, the Ge surface is very smooth and clean. The Ge surface of the refilling channel inside the oxide hole, which was not sufficiently polished, is quite rough. The sacrificial structure has a final thickness of approximately 4.5μm.

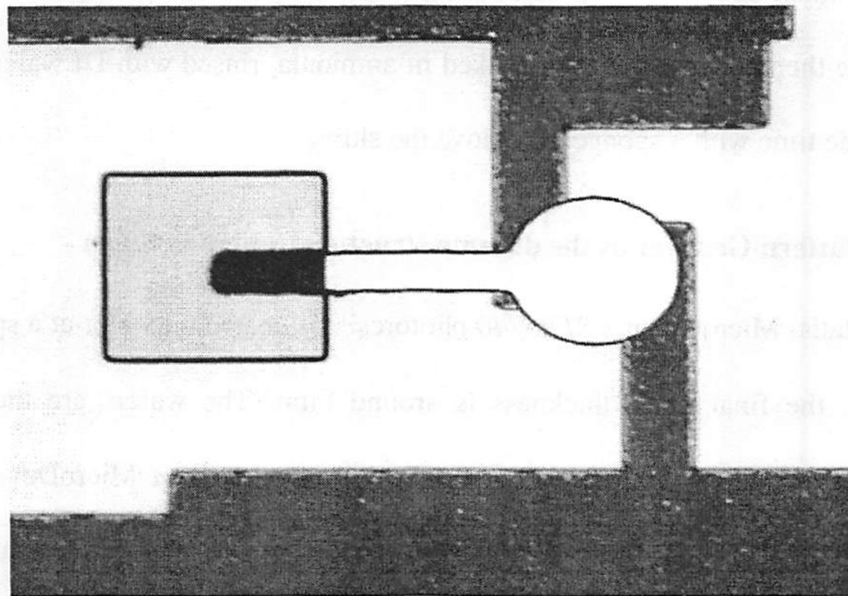

Figure 4.10: Top view of the Ge sacrificial structure

C: Forming the inkjet chamber wall, nozzle membranes and feeding holes

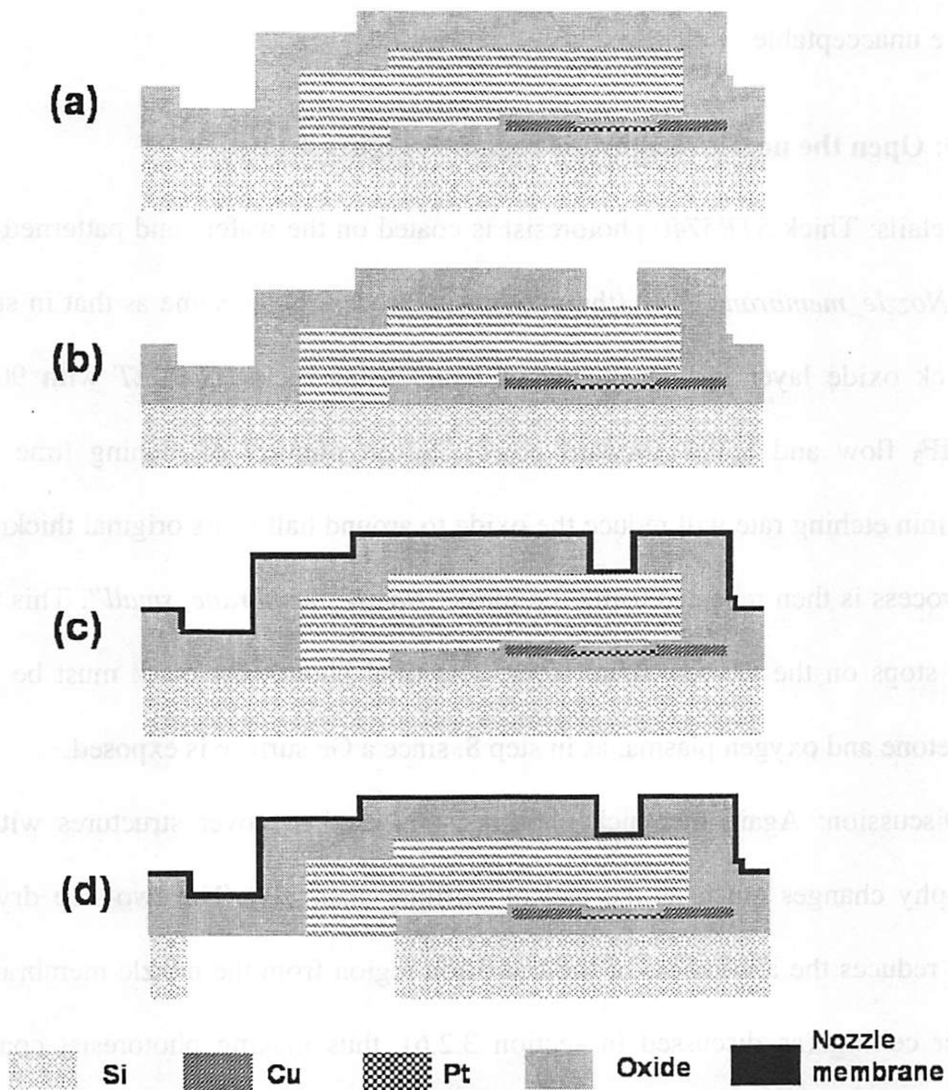

Figure 4.11: Forming inkjet chamber, nozzle membranes and feeding holes

Step 9: Deposit 5um LTO as chamber walls -- Figure 4.11(a)

Details: The LTO deposition recipe is the same as that in step 1, with deposition time around 6 hours; to ensure the strength of the inkjet structure, the chamber wall has a targeted thickness of around 5μm.

Discuss: The wafers can be cleaned with only acetone and water, before being loaded into the Non-MOS clean furnace. The *Piranha* bath etches Ge very quickly and is therefore unacceptable

Step 10: Open the nozzle membrane region--- Figure 4.11(b)

Details: Thick *STR5740* photoresist is coated on the wafers and patterned with the mask *"Nozzle_membrane_big"* (the photoresist process is the same as that in step 8-A). The thick oxide layer is then etched in *Lam2* using recipe *SIO2ET* with 90/30sccm CF_4/CHF_3 flow and 850W forward power. Seven minutes of etching time at about 450nm/min etching rate will reduce the oxide to around half of its original thickness. The same process is then repeated using the mask *"Nozzle_membrane_small"*. This time, the etching stops on the Ge sacrificial layer. The final photoresist mask must be removed with acetone and oxygen plasma, as in step 8, since a Ge surface is exposed.

Discussion: Again the thick photoresist is used to cover structures with abrupt topography changes (such as the end of refilling channels). The two-step dry etching process reduces the abruptness of the transition region from the nozzle membrane to the chamber ceiling (as discussed in section 3.2.6), thus making photoresist coating and patterning easier when opening the inkjet nozzles.

Step 11: Deposit thin LTO nozzle membrane-- Figure 4.11(c)

Details: An LTO layer is deposited using the same process flow as in step 9; depending on the targeted nozzle aspect ratio, the deposition time will be about 1-2 hours, producing a membrane thickness between 1-2μm.

Discussion: The newest process run of our inkjet device uses LTO nozzle membranes due to the low process temperature (450°C) and high membrane quality. Depositing oxide membranes involves a lower thermal budget than LPCVD nitride membranes (~750°C), and is also compatible with the Ge sacrificial material (due to low melting temperature and high vapor pressure of Ge). In addition, oxide membranes are free of pinhole defects found in nitride membranes deposited with a Plasma Enhanced Chemical Vapor Deposition (PECVD) process. Even though the oxide's Young's modulus is lower (70GPa compared with 200GPa for nitride), the membrane is still strong enough due to the small membrane area in our inkjet nozzle design (refer to section 3.2.6).

Step 12: Forming the liquid feeding holes through the wafer-- Figure 4.11(d)

A. Removing the material layers on the backside of the wafer:

Details: To open the liquid feeding holes from the backside of the wafers, we must remove the original deposited material layers. The oxide layer (about 6μm thick, including the chamber wall and nozzle membrane) is etched in *Lam2* for about 20min. Hot H_2O_2 (around 150°C) will remove the Ge layer in about 15min (etching rate ~0.4μm/s), until bare silicon surface is exposed. The Ge dummy structures in the front side of the wafer remain intact, protected by the high quality oxide layer.

B. Patterning the feeding holes

Details: *STR5740* photoresist is spin-coated twice to a final thickness of about 20μm. The photoresist thickness is necessary for through-wafer Si etching to a depth of 500μm. *Ksaligner* performs the lithography using the backside alignment mode and mask *"Hole"*; the exposure time is about 20s. The patterned wafer is then bonded with a

dummy wafer (coated with 2μm oxide) using photoresist, and hard baked in a *VWR* oven for 2 hours. The bonding procedure is necessary for the through-wafer etching process using *STS*.

C. Etching the feeding holes

Details: The wafer pair is then etched in *STS*, a silicon Deep Reactive Ion Etching (DRIE) machine, which cyclically alternates between etch and deposition steps forming high aspect ratio features. The etch firstly uses a high frequency Si etching recipe *ASH500* for 2 hours; after this, it switches to a low frequency silicon-on-insulator etching recipe *STSLF5* for about 30min. The HF recipe is for fast etching speed and LF recipe is used to minimize the footprint of the etched hole. Etching results must be checked frequently during the LF process (the Si is completely etched when the holes look bright and shinny under microscope) to prevent over-etching, which will result in a big and fragile membrane. The wafers are then de-bonded in *PRS3000* bath.

The through-wafer etching result of the liquid feeding holes is shown in Figure 4.12. The holes in the picture are about 150μm big. Using a carefully tuned *STS* etching recipe, the DRIE etching can produce features with aspect ratio of 30:1 [9], hence feeding holes as small as 50μm can be formed to reduce the device area on our print head.

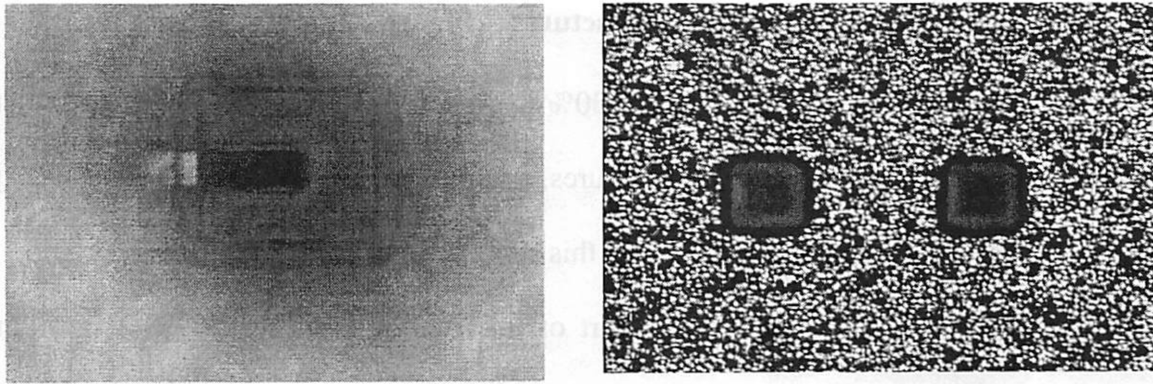

Figure 4.12: DRIE etched through wafer feeding holes

E: Opening the inkjet chamber, refilling channels and nozzles

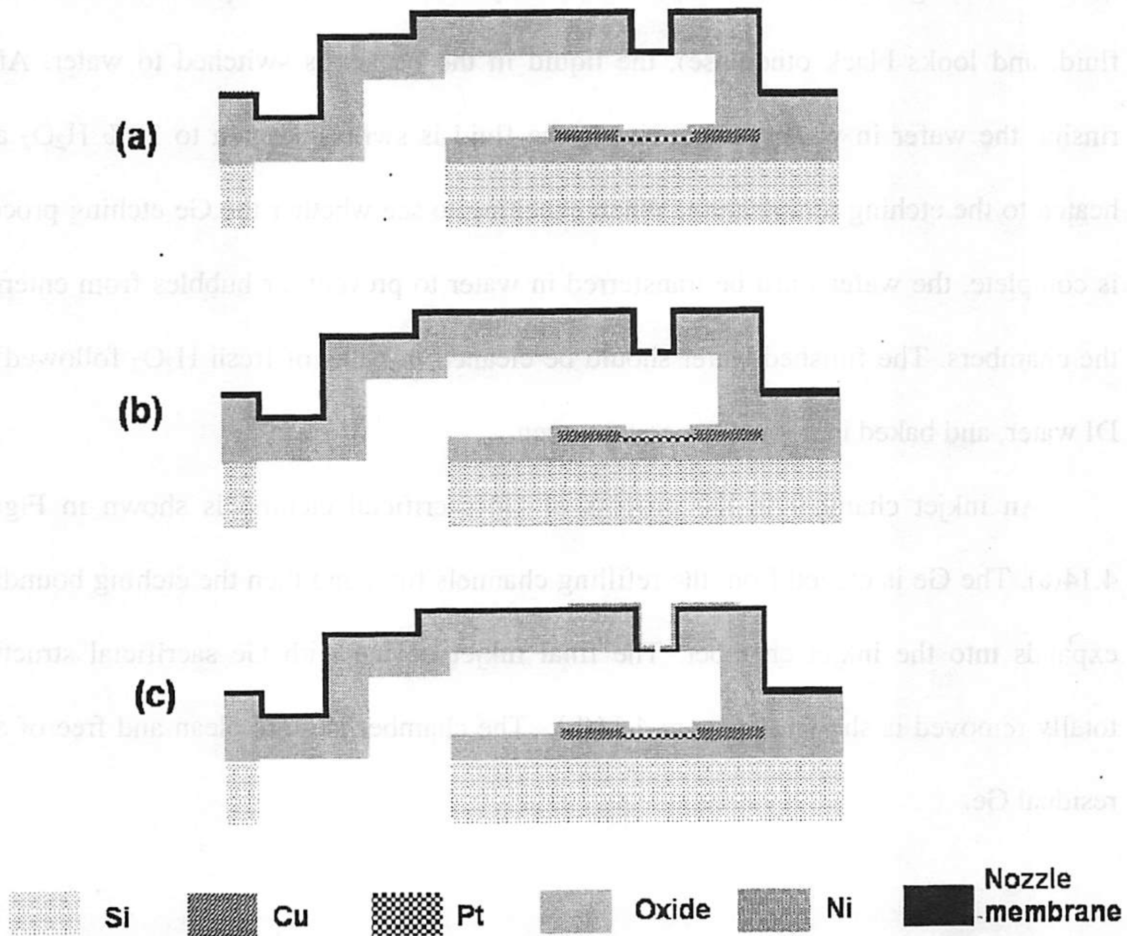

Figure 4.13: Forming inkjet chamber, refilling hole, bonding pads and nozzle membranes

Step 13: Removing the dummy Ge structures -- Figure 4.13(a)

Details: More than 6 hours in a 30% hydrogen peroxide bath, heated to around 150°C, removes the Ge sacrificial structures, and opens the refilling channels and inkjet chambers. The Ge etching rate is slow in this step due to the small channels.

Discussion: The most difficult part of this step is ensuring that H_2O_2 goes into every refilling hole on the wafer, for a high device yield. Since water doesn't wet the Si sidewalls of the feeding holes, the wafer is first immersed in acetone (which wets both silicon and oxide well) with filling holes facing up. When all the holes are filled with fluid (a little agitation of the wafer is necessary; the holes look bright when filled with fluid, and looks black otherwise), the liquid in the beaker is switched to water. After rinsing the wafer in water several times, the fluid is switched again to 30% H_2O_2 and heated to the etching temperature. When checking to see whether the Ge etching process is complete, the wafer must be transferred in water to prevent air bubbles from entering the chambers. The finished wafer should be cleaned in baths of fresh H_2O_2 followed by DI water, and baked in a low temperature oven.

An inkjet chamber in the process of Ge sacrificial etching is shown in Figure 4.14(a). The Ge is etched from the refilling channels first, and then the etching boundary expands into the inkjet chamber. The final inkjet device with Ge sacrificial structure totally removed is shown in Figure 4.14(b). The chamber is quite clean and free of any residual Ge.

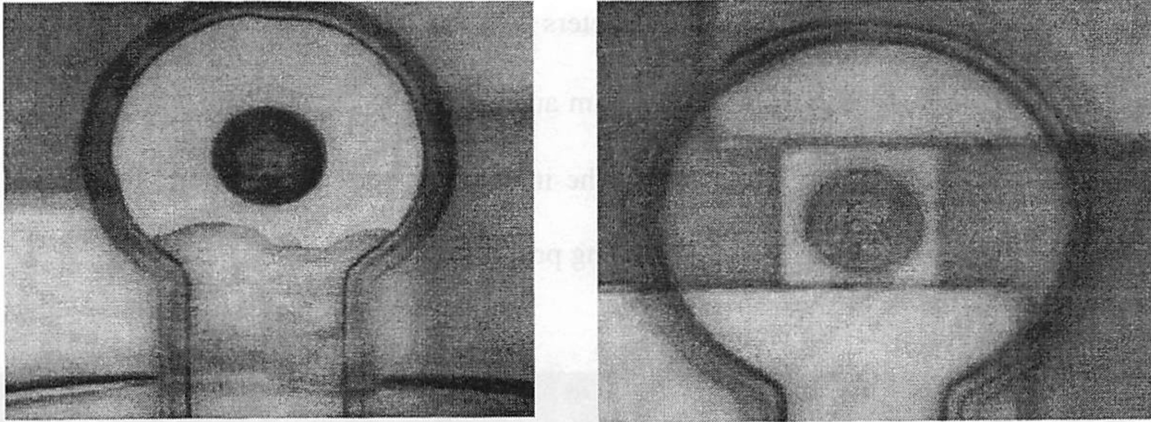

Figure 4.14: Ge sacrificial etching process. Left: Ge is removed from the refilling channel and inkjet chamber by hot H_2O_2, right: Ge is totally removed from inkjet chamber

Step 14: Dry-etching the nozzles-- Figure 4.13(b)

A. Pattern the nozzle etching mask

Details: The etching mask uses 2μm *G-line* photoresist (1μm photoresist is also tested, but the nozzle edges are not protected well). The photoresist will actually be thicker on top of the nozzle membrane due to the well structure, so over-exposure is necessary (~10s exposure time in *Ksaligner*). The nozzle dimensions can actually be controlled by adjusting the exposure dose and developing time. No hard bake of the photoresist is allowed: this causes photoresist reflow, which reduces the patterned nozzle size and makes the nozzle shape irregular.

B. Etching the nozzles

Details: The nozzle is etched in *Lam2* with the same recipe as in step 10. The etching time is around 4min, much longer than the typical etching time of a 1μm thick oxide film, because the plasma etching rate is lower for the small pattern size. After nozzle etching, the photoresist mask is removed by oxygen plasma in *technics-c*. Neither acetone nor *PRS3000* bath can be used, as they may contaminate the inkjet chambers.

Plasma etched nozzles with diameters of 5μm and 2.5μm are shown in Figure 4.15. The original mask openings are 5μm and 3μm, respectively. The nozzles have a round shape with small irregularities. The inkjet chambers are clean and there is no photoresist residue after the nozzle etching process.

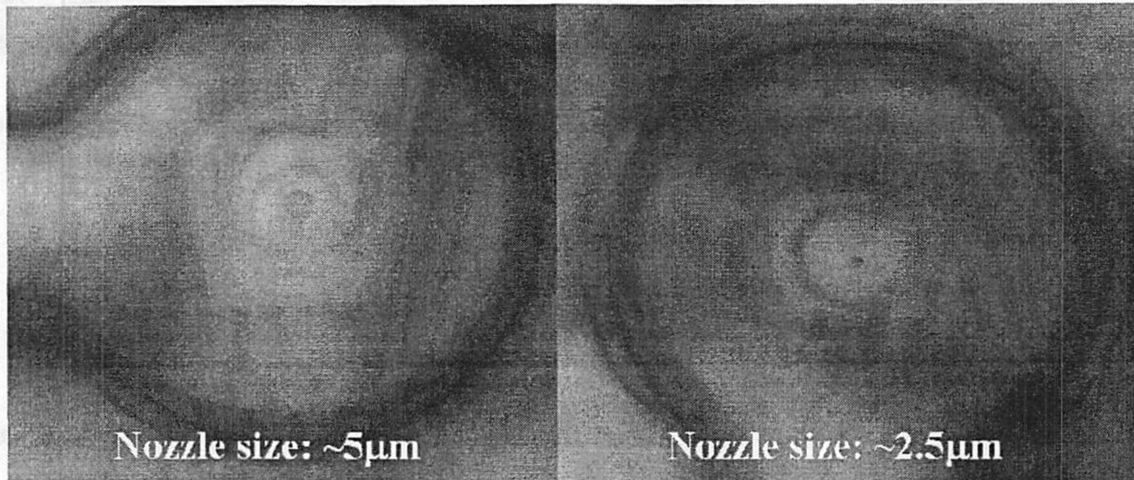

Figure 4.15: Inkjet nozzles opened by plasma etching method. Left: 5um scale nozzle; right: 2.5um scale nozzle. The inkjet chamber is clean and no photoresist residual after the nozzle etching

Step 15: Coat the nozzles with Ni anti-wetting coating-- Figure 4.13(c)

Details: In *Edwardeb3*, the entire wafer surface is then coated with an anti-wetting coating of 20/200nm Ti/Ni, excepting the bonding pad regions protected with *Kapton* tape. The Ni layer is deposited with 100Amp current flow and a deposition rate around 0.12nm/s.

4.2.2 Test chip structure

The Ge sacrificial structure etching process described above has successfully generated test chips of the designed high resolution thermal bubble inkjet print head.

Figure 4.16 shows the layout of a test chip. Each chip is composed of a row of inkjet devices with varying heater, chamber and nozzle sizes, as well as interconnect lines and bonding pads for electric heating signal input. SEM and micrographic pictures of an array of inkjet devices formed on the test chip (without a Ni coating) is shown in Figure 4.17. We can clearly see the inkjet refilling holes and the Pt heaters beneath the top oxide membrane. The inkjet chambers vary in size between 60-100μm, and heaters between 20-50μm. The refilling channels are about 30μm wide and 100μm long counting from the edge of the feeding hole. A single inkjet device is shown in close-up, in Figure 4.18. The device has a small nozzle membrane (15μm in diameter), shallow inkjet chamber (5μm deep) and thick chamber walls (6μm thick) as designed in chapter 3.

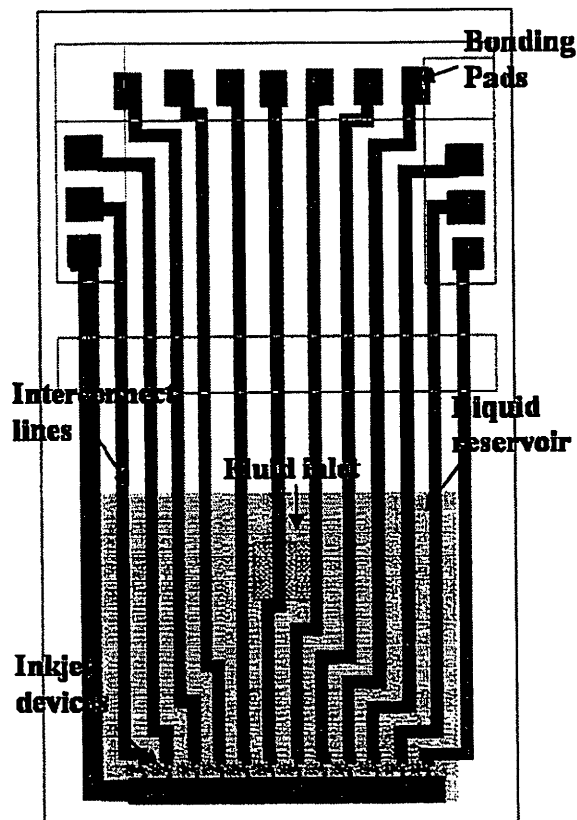

Figure 4.16: Test chip layout

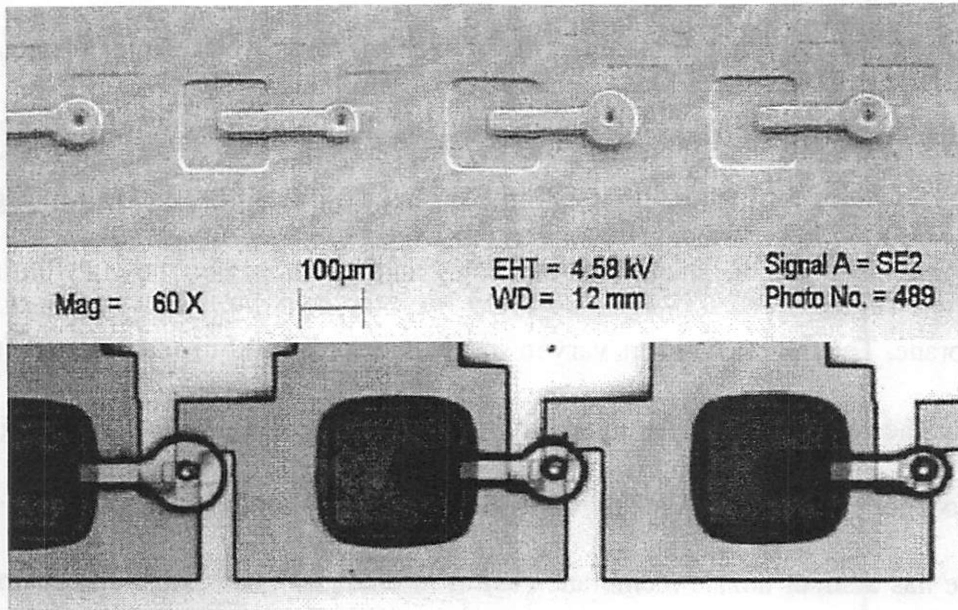

Figure 4.17: Array of inkjet structures on test chip

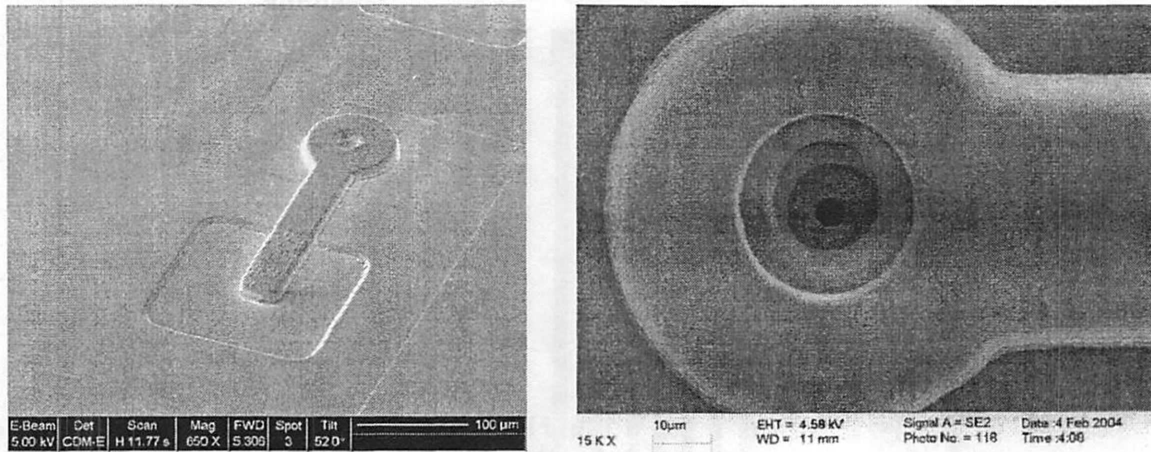

Figure 4.18: SEM pictures of a single inkjet device with 4μm nozzle

For experimental purposes, a handling chip connects the inkjet devices on the test chip to a liquid delivery system in our experimental setup. The handling chip is composed of a large fluid inlet and a liquid reservoir, which is open to all the feeding holes on the device chip. Its fabrication process is illustrated in Figure 4.19. A silicon

wafer is first coated with 1μm silicon oxide, and the oxide layer is patterned to form an etching mask for the reservoir region. Large fluid inlets (~2mm) are then etched through the handling wafer using the same through wafer etching process described in step 12. The pre-patterned oxide is used as the mask for a second DRIE etching step to form 100μm deep liquid reservoir.

Disco cuts the device and handling wafers into identically sized chips. To prevent cutting debris from entering the inkjet structures, which could clog the inkjet nozzle and refilling channels, the wafers are protected with photoresist on the top, and sealed with a blue tape at the bottom (the side with the feeding holes). After dicing, the chips are carefully removed from the tape, and cleaned with acetone. The device chip and the handling chip are then bonded together using a chemically resistant epoxy (*Epo-tek 377*) on the edges, as shown in Figure 4.20. The chip pair is then baked and mounted on a ceramic package, which provides the electrical contacts to the inkjet devices. A plastic tube (1/4'' inner diameter) is attached to the liquid inlet of the handling chip, also using *Epo-tek 377,* and the other side of the tube is connected to a liquid delivering system with Swagelok fitting. A wire-bonded test chip, ready for a droplet generation experiment, is shown in Figure 4.20(b)

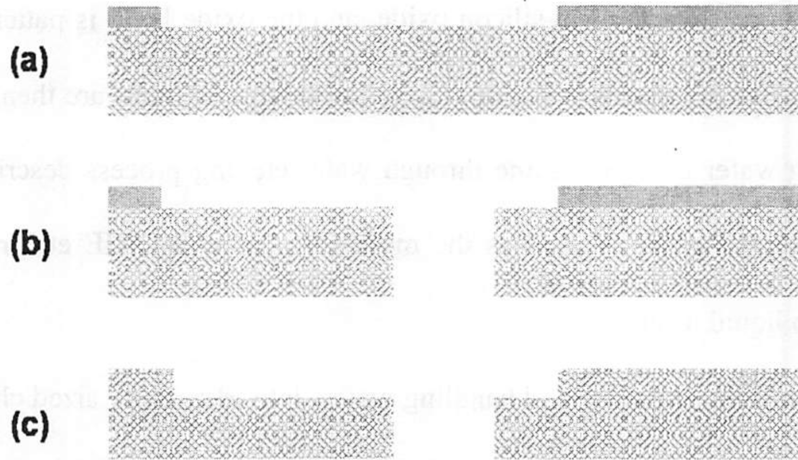

Figure 4.19: The handling chip fabrication process

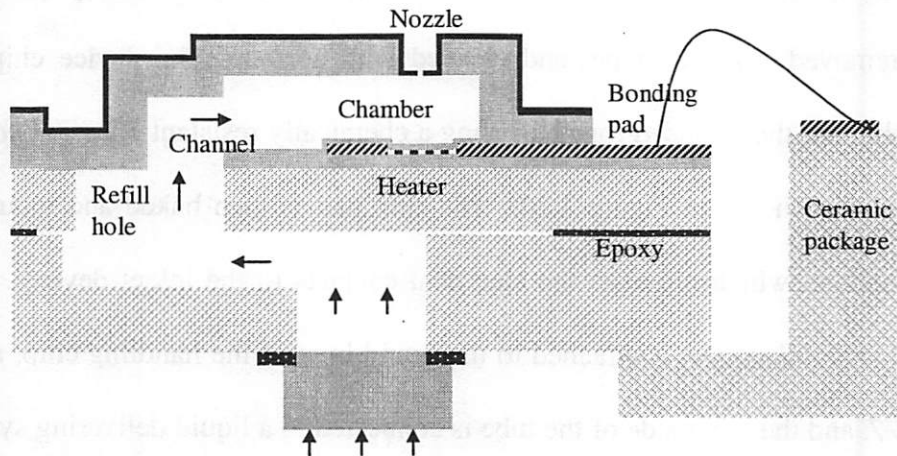

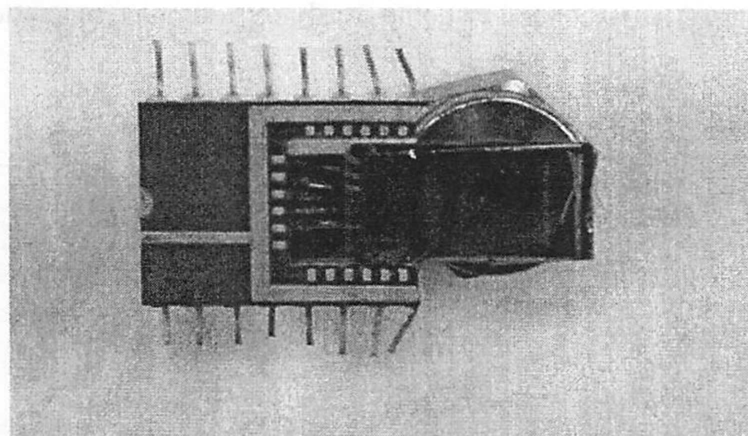

Figure 4.20: (a) Schematic of the final test chip structure; (b) micrographic image of a test chip attached with plastic tubing and wire bonded with a ceramic package

4.3.2 Focused Ion Beam drilled nozzles

The smallest nozzle that we can reliably fabricate using the plasma etching machines available in the Microlab measures approximately 2.5μm, due to both the optical lithography resolution (2μm) of the front/back alignment tool and the well-shaped structure of the inkjet nozzle. Smaller nozzles can be formed by slightly baking the photoresist (Figure 4.21), though their sizes and shapes are hard to control, and device yield is very low.

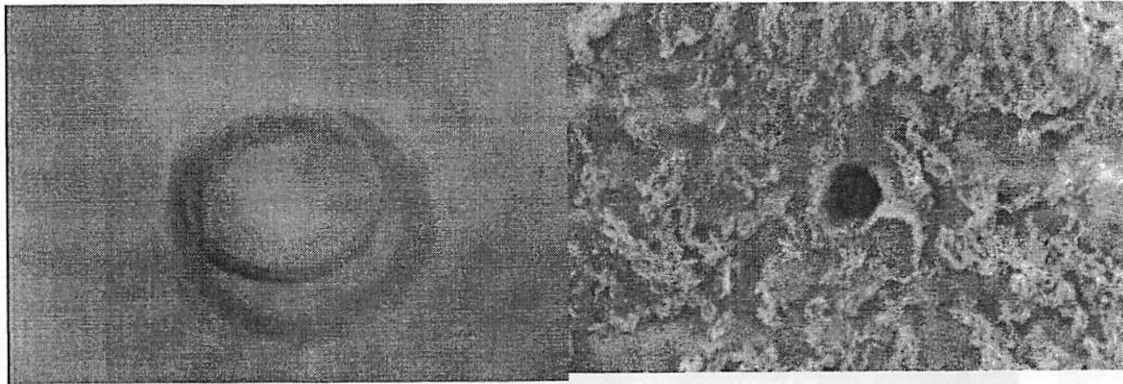

Figure 4.21: 1μm scale nozzle opened by photo resist reflow and plasma etching method with irregular nozzle shape and low yield

Our process flow does not open nozzles until the last step, so we could then form small nozzles by a direct Focused Ion Beam (FIB) drilling method. The National Center for Electron Microscopy (NCEM) of Lawrence Berkeley National Lab (LBL) provided the dual beam FIB system used in our research [12]. The smallest hole the system could produce is around 50nm in diameter. FIB drilling also offers additional advantages over plasma etching, such as a perfectly round nozzles and smooth sidewalls for uniform and stable droplet generation. A 1.2μm nozzle opened in a 1μm

thick oxide membrane is shown in Figure 4.22. The nozzle is already coated with a Ni anti-wetting coating, for imaging purposes. Our research uses test chips with nozzles formed both by plasma etching (down to 2.5μm) and FIB drilling (1μm-2μm) methods to experimentally study the minimum droplet size producible with our print head design. The experimental results will be discussed in the next Chapter.

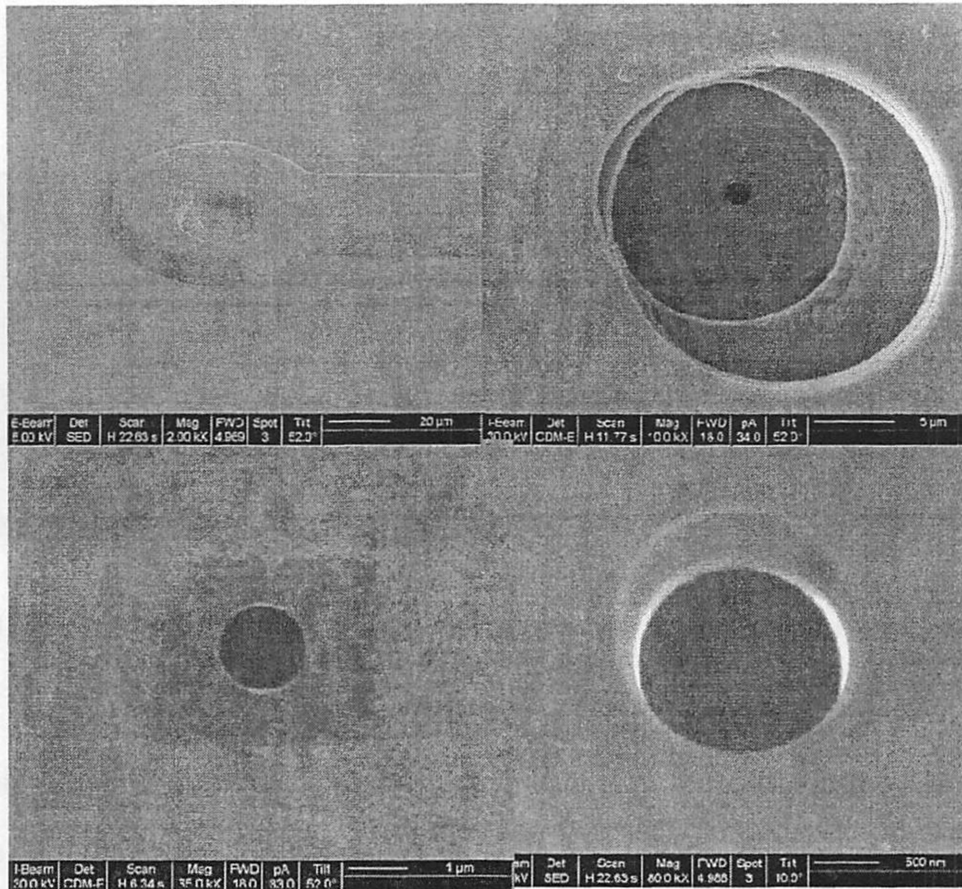

Figure 4.22: Focused ion beam drilled 1.2μm nozzle

4.3.3 Advantages of the Ge sacrificial etching process

In summary, we have developed a novel inkjet print head fabrication process using Ge sacrificial structures. This process is suitable for the fabrication of inkjet print heads

with high resolution and high droplet delivery rates for maskless lithography purposes, due to the following advantages:

1) The inkjet devices are fabricated on a single silicon wafer without a bonding process, which reduces fabrication complexity and increases the device yield.

2) The patterning accuracy is only limited by the resolution of the optical lithography system and is in the micron range. Our inkjet design can therefore be implemented fully, to achieve smallest droplet size.

3) The whole process has a low thermal budget (highest deposition temperature 450°C), so switching CMOS circuits can be fabricated with the inkjet devices to form a monolithic print head. The CMOS process can be integrated before the heater fabrication in step 1, or between steps 11 and 12, after formation of the Ge dummy structures and before opening of the inkjet chamber and nozzles.

4) The inkjet chambers, refilling channels and nozzles are made of materials such as silicon, silicon dioxide, and Ni, which have good chemical compatibility. This allows the print head to print materials other than water, for electric or mechanical device fabrication.

The process flow is also not limited to fabrication of inkjet print heads. With certain modifications, the Ge sacrificial etching method can also be used to form micro-fluidic structures for various sensors or actuator applications.

Reference

1. UC Berkeley Microfabrication Facility, http://www-microlab.eecs.berkeley.edu

2. Harendt, W. Appel, H.G. Grag et al, "Wafer fusion bonding and its application to silicon-on-insulator fabrication", *Journal of Micromechanics and Microengineering,* Wol. 1, pp145-151,1991.

3. Y.H. Wu, C. H. Huang et al, "The buried oxide properties in oxygen plasma-enhanced low-temperature wafer bonding", *Journal of the Electrochemical Society,* Vol.147 pp.2754-6, 2000.

4. X. Z. Xuan, J.P. Raskin, " Investigation on the uniformity of surface energy in silicon direct-bonding technique", *Journal of the Electrochemical Society,* Vol.151, pp.G568-73, 2004.

5. Klink, B. Hillerich, "Wafer bonding with an adhesive coating", *Proceedings of SPIE,* Vol.3514, pp.50-61, 1998.

6. Niklaus, P. Enoksson, E. Kalvesten, G. Stemme, "Low-temperature full wafer adhesive bonding", *Journal of Micromechanics & Microengineering,* Vol.11, pp.100-7, 2001.

7. C. Christensen, S. Bouwstra. " Eutectic bonds on wafer scale by thin film multilayers", *Proceedings of SPIE,* Vol.2879, pp.288-90, 1996.

8. Z.X. Xiao, G.Y. Wu et al., "Silicon/glass wafer-to-wafer bonding with Ti/Ni intermediate bonding", *Sensors and Actuators A*, Vol. 71, pp123-126, 1998.

9. Y. Shroff, Yijian Chen, W. Oldham, "Fabrication of parallel-plate nanomirror arrays for extreme ultraviolet maskless lithography", *Journal of Vacuum Science & Technology B*, Vol.19, pp.2412-15, 2001.

10. E.H. Klaassen, K. Petersen, J.M Noworolski et al, " Silicon fusion bonding and deep reactive ion etching; a new technology for microstructures" *8th International Conference on Solid-State Sensors and Actuators and Eurosensors IX.* Vol.1, pp.556-9, 1995.

11. A. Ayon, C. C. Lin, R. A. Braff, M. A. Schmidt, R. Bayt, and H. H. Sawin, "Etching Characteristics and Profile Control in a Time multiplexed Inductively Coupled Plasma Etch," *Solid-State Sensor and Actuator Workshop*, pp. 41-44, 1998.

12. NCEM dual beam FIB system: http://ncem.lbl.gov/frames/FIB.html

CHAPTER V

EXPERIMENTAL REULTS OF BUBBLE FORMATION AND DROPLET GENERATION

5.1 Experimental system

To determine the size limits for droplets produced by our thermal bubble inkjet print head and the operation conditions for stable and satellite free droplets formation, we have created a high resolution video imaging system to observe the bubble formation and droplet generation process in our test chips. A block diagram of our experimental setup is shown in Figure 5.1.

Several synchronized pulse generators provide square-shaped electric pulses with adjustable pulse magnitude (0.1-50V) and width (ns to ms range) to drive the heaters and trigger a strobe light source. Adjusting the delay time between the driving signal and the strobe trigger signal allows the system to capture different phases of the inkjet operation. The strobe light has a pulse width smaller than 1μs, and can thusly capture the bubble formation and droplet generation processes, which have time scales of several micron seconds. A Mitsubishi long-working-distance 100X objective lens is mounted to an externally triggered black and white CCD camera. The finite test chip size makes the long working distance necessary. Careful tuning of the focusing optics allows us to focus

both the camera and strobe light at the same point, as illustrated in Figure 5.2. Our test results indicate that the imaging system has a maximum resolution of about 1μm. The output video signal of the CCD camera is then connected to a TV monitor and a Sony Walkman, which can perform an analog-to-digital conversion of the video signal and record the result on Mini DV disks. A computer with video capturing and editing software extracts the desired video sequences and frames from the videos.

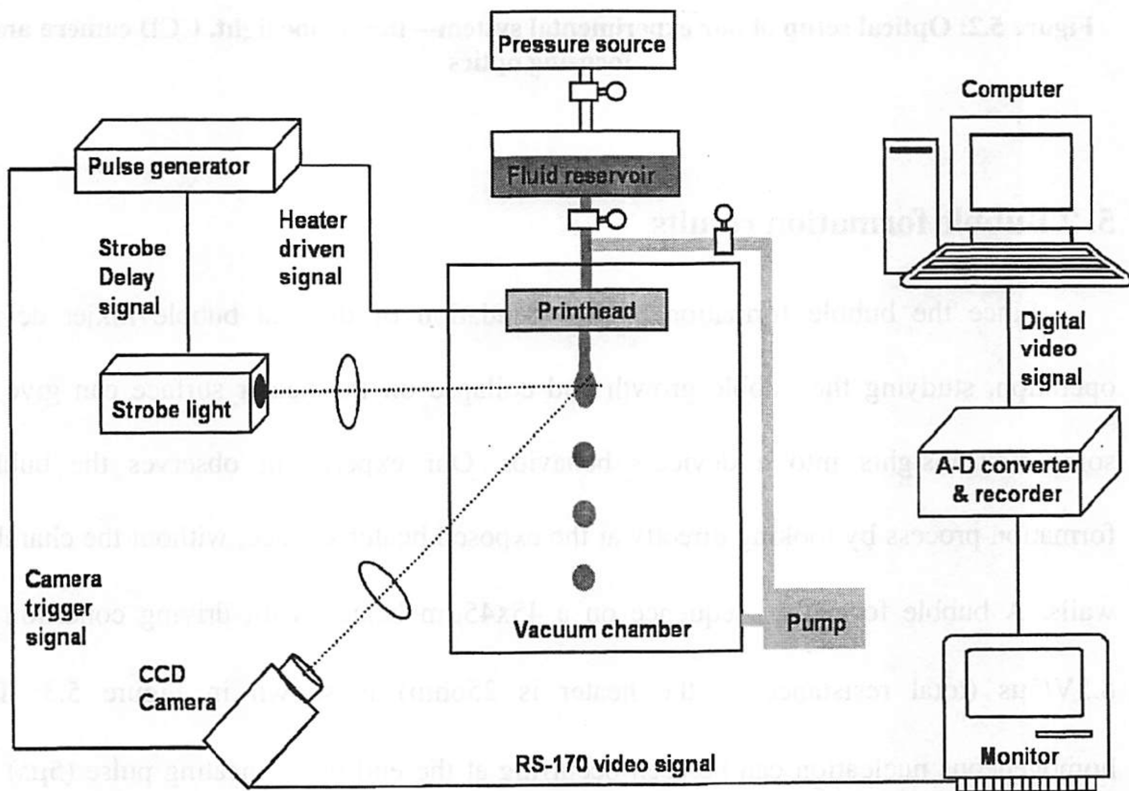

Figure 5.1: Experimental system for observing bubble formation and droplet generation process

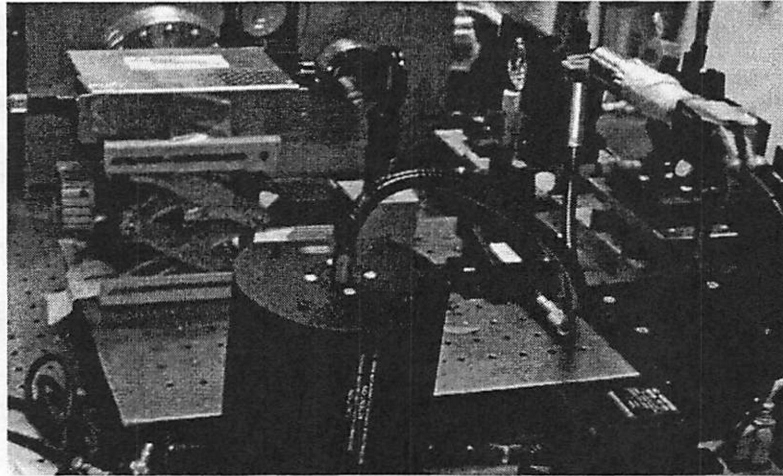

Figure 5.2: Optical setup of our experimental system—the strobe light, CCD camera and focusing optics

5. 2 Bubble formation results

Since the bubble formation is the foundation of thermal bubble inkjet device operation, studying the bubble growth and collapse on the heater surface can give us some first insights into a device's behavior. Our experiment observes the bubble formation process by looking directly at the exposed heater surface, without the chamber walls. A bubble formation sequence on a 45x45μm heater, with driving condition of 8.5V/5μs (total resistance of the heater is 25ohm) is shown in Figure 5.3. The homogeneous nucleation can be seen occurring at the end of the heating pulse (5μs) on the whole heater surface; the bubble then grows to its largest volume in about 3μs and collapses after 5μs, as predicted by thermal bubble inkjet theory.

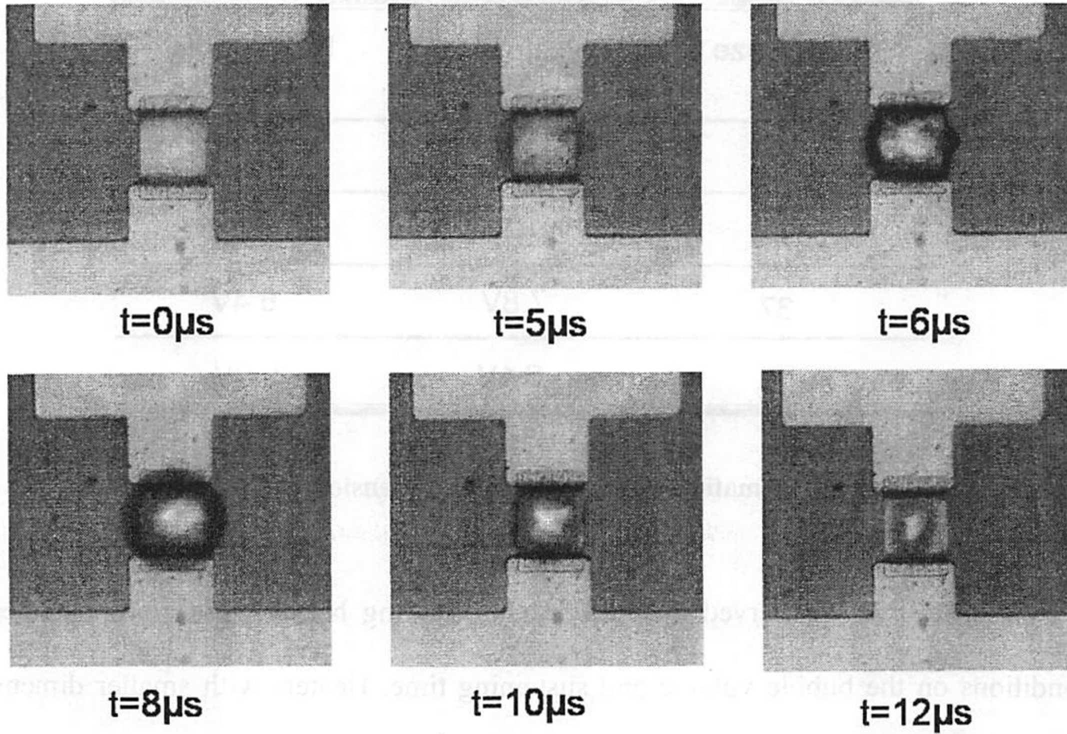

Figure 5.3: Bubble nucleation, growth and collapse sequence on a 45x45μm^2 heater with heating pulse of 8.5V/5μs

5.2.1 Influence of heating signal on bubble formation

From our experiment, we found that, given a fixed driving pulse width, the initial bubble formation voltage is almost proportional to the heater size, as shown in Table 5.1, indicating that, with identical heating thermal flux, the fluid temperature profiles remain similar, regardless of the heater dimension. The one-dimensional treatment of the heater operation is then well grounded. The initial bubble formation voltage also decreases as the pulse width increases. From the pulse width and voltage magnitude, we can use our 1-D thermal diffusion model to calculate the liquid temperature at the heater surface at the point of nucleation. This estimates that water nucleates around 270°C, which is quite close to the theoretical prediction (around 300°C) for a thermal bubble inkjet device.

Heater size (μm)	Pulse width 3μs	Pulse width 8μs
60	12.8V	11.0V
45	10V	7.5V
37	7.8V	6.4V
25	6.1V	5.0V

Table 5.1: Bubble formation voltage vs. heater dimension and heating pulse width

We have also observed the influence of varying heater dimensions and heating conditions on the bubble volume and sustaining time. Heaters with smaller dimensions generate substantially thinner bubbles (the bubble looks brighter on visual inspection), and sustain them for less time, which indicates a lower bubble actuation strength resulting smaller liquid vapor boundary movement. The bubble becomes much larger if we drive the heater with a longer pulse width and smaller thermal flux. These observations are quite consistent with the theoretical predictions of bubble behavior in Chapter 3. We also found that continued heating after bubble formation can also increase the bubble sustaining time, meaning that more thermal energy can be transferred from the heater to the surrounding liquid for vapor evaporation, even after the formation of a low-conductive vapor layer, which no previous bubble formation studies have reported.

The heater will break down when the heating voltage exceeds a certain magnitude. As shown in Fig. 5.4, the square-shaped heater breaks first at the center, indicating that thermal melting rather than high current flow is the main reason for the breakdown, since the heater temperature is the highest in the center, while the current density is uniform

everywhere. The heater breakdown and bubble formation voltages vs. heating pulse width for a 30um heater are listed in Table 5.2. We can see that the discrepancy (in percentage) between these two voltages is larger with longer pulse widths (lower thermal flux), which have flatter temperature profiles and lower heater temperatures. Heaters break down even before bubble nucleation if driven with pulse widths shorter than 0.5us. We have also tested the thermal stability of the Pt thermal heater under typical bubble formation conditions (~3μs pulse width), the heater does not change resistance significantly, even with hours of operation at driving frequencies as high as 20 kHz.

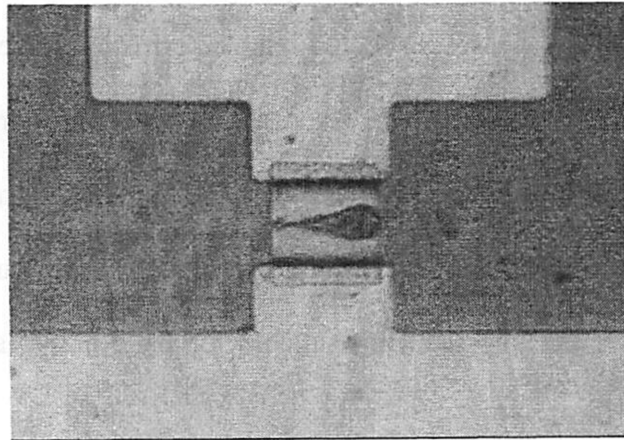

Figure 5.4: Micrographic image of a broken heater

Pulse width (μs)	1	2	3	5	8	13
Heater break voltage (V)	24	15	13	11	9	8.2
Bubble voltage (V)	21	11.2	9.7	8	6.8	5.8

Table 5.2: Observed heater breaking and bubble formation voltage vs. heating pulse width

5.2.2 Bubble formation in different materials

We also tested bubble formation behaviors for fluids other than water. Commonly used organic solvents, including methanol, acetone, toluene, and polyimide thinner, etc, also generate vapor bubbles. The calculated bubble formation temperatures for these materials are listed in Table 5.3. The values are lower than that of the water, which is consistent with the superheat temperature of these materials, as shown in Table 5.4. The maximum bubble actuation pressure of methanol and toluene, which is equal to the saturated vapor pressure of the fluid at the nucleation temperature, is then estimated to be around 1MPa.

In our research, we also conducted bubble formation experiments with materials such as epoxy and photoresist. As expected, the polymer components in these materials are not stable when their solvents are heated to the bubble formation temperature, and residues quickly form on the heater surface, preventing further bubble nucleation. These polymer-based materials are then not suitable for pattern formation with our thermal bubble inkjet print head.

Material	Bubble nucleation temperature (°C)
Methanol	160C
Toluene	200C
Polyimide thinner	210C
Propylbenzene	230C

Table 5.3: Calculated bubble nucleation temperature for different organic solvents

Material properties	Methanol	Toluene	Water
Superheat temperature at 1atm (C°):	193	260	312
Saturated vapor pressure (bar)	25	14	70
Viscosity (1e-3 Pa-s):	0.58	0.6	1
Surface tension (N/m):	0.023	0.029	0.073
Density (g/cm3)	0.79	0.87	1

Table 5.4: Fluid properties of typical organic solvents at superheat temperature

5.3 Droplet generation results

After determining the appropriate driving conditions for bubble formation, we used the imaging system to study the droplet generation behavior of our test chips. Each test chip was wire bonded to a ceramic package and connected to a fluid reservoir, as described in Chapter 4. The liquid in the reservoir was filtered and free of particles, to avoid clogging of the small inkjet nozzles and refilling channels. To prevent the formation of air bubbles inside the inkjet chamber, which would absorb the actuation pressure wave and prevent droplet ejection, each test chip was first mounted inside a vacuum chamber (Figure 5.3) and evacuated of air by a mechanical pump. Then, the valve to the vacuum system is closed, and valve to the liquid reservoir is opened; liquid flows into the chambers under atmospheric pressure. The chamber is then vented and excess liquid is absorbed by a lens paper. The chip is then removed and carefully mounted to an XYZ stage. By adjusting height of the liquid reservoir relative to the nozzles, we can maintain a small positive pressure in the liquid delivering system without leaking fluid from the nozzles (which is not too difficult with helping of the anti-wetting

coating). We can then, apply a heating pulse with adjustable width and magnitude to the inkjet devices on the test chips, through the ceramic package.

5.3.1 Minimum droplet dimensions

Test chips fabricated using both the wafer bonding and the Ge sacrificial structure etching methods generated droplets as predicted. The formation sequence of a single 15μm droplet generated from a 10μm nozzle on a bonded test chip is shown in Figure 5.5. The smallest droplet size we have ever observed for a bonded test chip is about 5μm, from 4μm scale nozzles. No droplet formation occurs for nozzles with smaller dimensions due to the limitations of the inkjet device structure fabricated using the wafer bonding method.

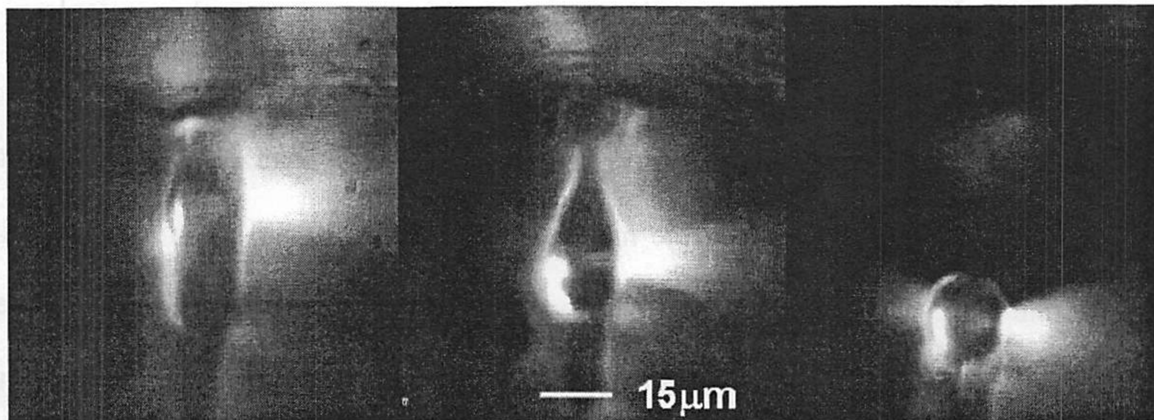

Figure 5.5: Single droplets formation sequence from a 10μm nozzle on a bonded test chip

Test chips fabricated using Ge sacrificial structure etching methods can produce smaller droplets, with nozzle dimensions as small as 1.2μm. The sub-2μm nozzles are actually formed by focused ion beam drilling. The minimum observed size of a single

droplet vs. nozzle diameter for our test chips is listed in Table 5.5. We measure droplets by comparing video images of the droplet to a reference length mark etched on the surface of the test chip. A reference length mark is shown in Figure 5.6.

Nozzle size (μm)	7	5	3.5	2.5	2	1.5	1.2
Droplet size (μm)	10	7	5	3.5	~3	~3	~3

Table 5.5: Observed minimum droplet size vs. nozzle diameter

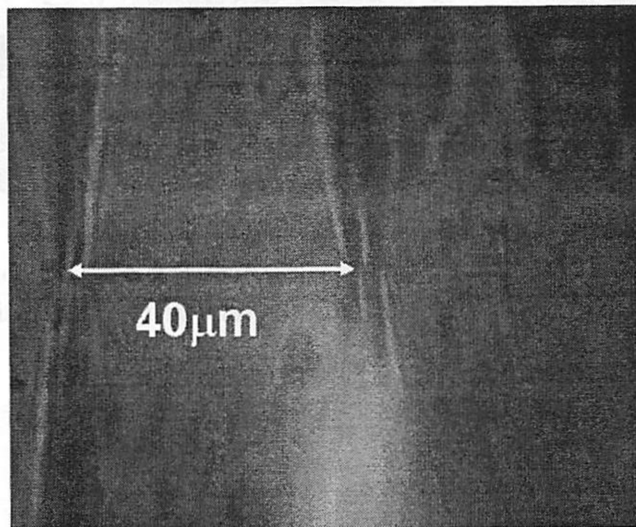

Figure 5.6: Reference length mark on the test chip surface

Figure 5.7 shows the sequence of 10μm scale droplets generated from an 8μm nozzle from our single wafer test chip. At this scale, a liquid column can be clearly seen formed outside the nozzle, and a thin neck evolves before the droplet detachment. The total droplet formation time (from emergence of liquid head to the break-up) is 5μs, quite close to the numerical simulation result shown in Table 2.2. Figure 5.8 shows a single

3.5μm droplet generated from a 2.5μm nozzle, which is the smallest nozzle size that can be fabricated using the plasma etching process. Because of the smaller nozzle dimension, the droplet formation time is reduced to around 1.5μs, also consistent with the theoretical predictions.

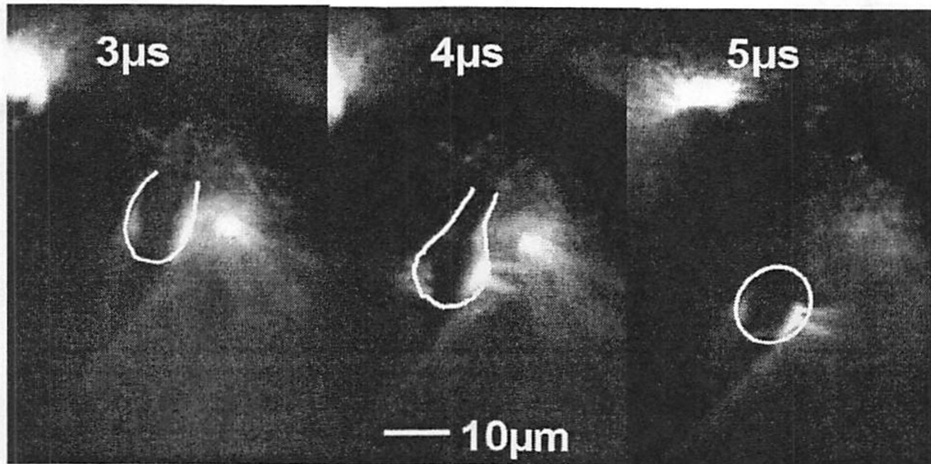

Figure 5.7: Single droplets formation sequence from a 7μm nozzle with 8V/ 4μs heating signal. The droplet size is about 10μm; the total droplet formation time is 5μs.

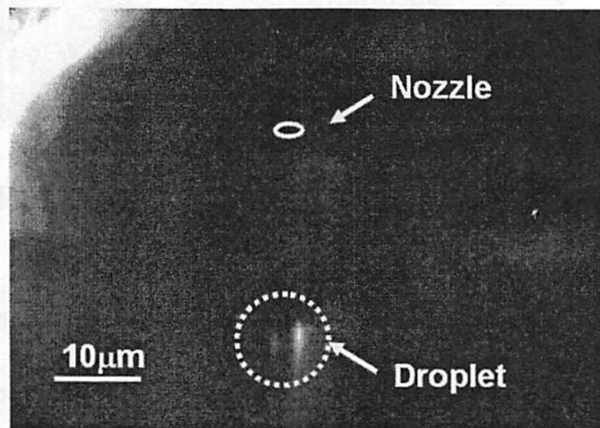

Figure 5.8: Single droplets formation from a 2.5μm nozzle, the droplet size is about 3.5μm

The smallest droplet size we have ever observed was generated from a 1.5μm scale nozzle and measured about 2.8μm (Figure 5.9). Decreasing the nozzle size below 2μm does not actually reduce droplet dimensions effectively; the droplet size becomes fixed around 3μm as indicated in Table 5.5. Two aspects explain the discrepancy between the experimental results and our theoretically predicted limit of a thermal bubble device (0.5μm). Firstly, the theoretical study assumes that the bubble actuation pressure follows a simple exponential shape, and that the pressure pulse width can be arbitrarily tuned. This is actually an oversimplification. There are many factors that influence the bubble's pressure profile, including liquid nucleation probability on the heater surface, heat transfer speed from the fluid to the liquid/vapor interface for liquid evaporation, the fluid inertial to bubble expansion, etc. The real bubble's pressure profile can be much more complicated; its high pressure part may be much shorter than our numerical simulation input, while its low pressure range can be longer. Secondly, the inkjet device simulation used an incompressible fluid model. The finite compressibility of the fluid and the acoustic reflectance of the nozzle and chamber boundaries can change the pressure distribution in the chamber and nozzle substantially, since the pressure magnitude here is in MPa range.

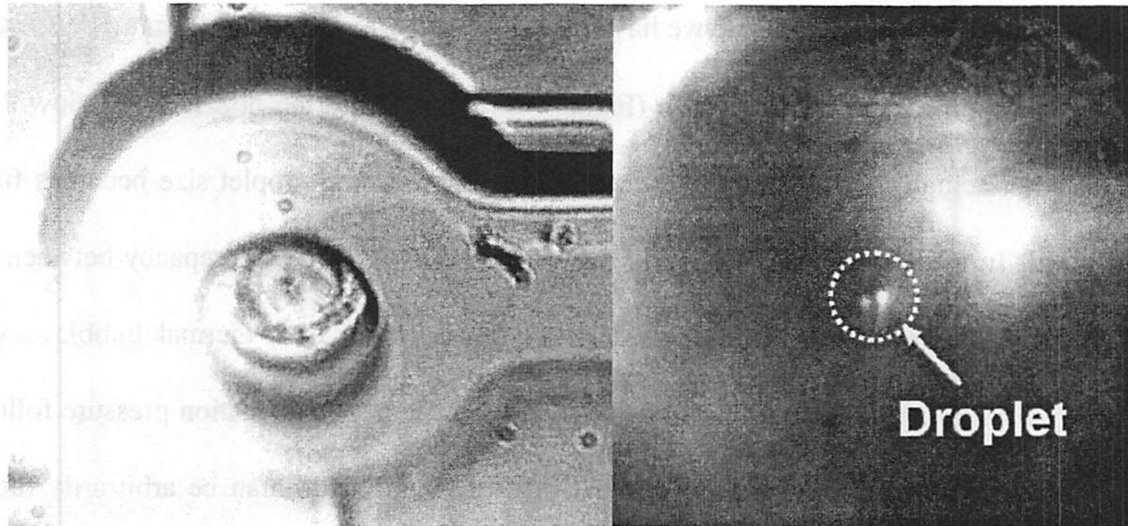

Figure 5.9: A 2.8μm single water droplet generated from a 1.5μm nozzle. Left: nozzle view, right: 2.8μm droplet

5.3.2 Influence of heating signal and heater size

Our experiments show that the droplet generation process depends strongly on the input heating signal, which is not surprising since we have already observed signal's influence on bubble actuation behavior. However, the strength of its influence on droplet generation varies significantly across different nozzle sizes.

First we consider a small nozzle (nozzle diameter in 1-3μm), holding the driving pulse width constant. Gradually increasing the heating voltage beyond the initial bubble formation voltage results in the formation of a liquid head, but no break-up. The liquid head emerges at the end of the heating signal, then becomes longer or even undergoes small surface distortions, but then retracts back to the nozzle, and no droplet break-up actually occurs. As the heating voltage increases further, the surface deformation of the liquid head magnifies, and, given a sufficiently long heating pulse, single droplet detachment can be observed when the voltage reaches a certain level. A barely-formed

droplet has a rather low velocity. Increasing the driving voltage or pulse width increases the droplet velocity and causes a slight enlargement of droplet size. Further increases cause the formation of satellite droplets, as shown in Figure 5.10, while the main droplet velocity continues to increase. Nozzles with dimensions between 1.2 to 2μm, will generate only single satellite droplets before the heater reaches its breaking voltage.

Figure 5.10: Satellite droplet formation from a sub-2μm nozzle

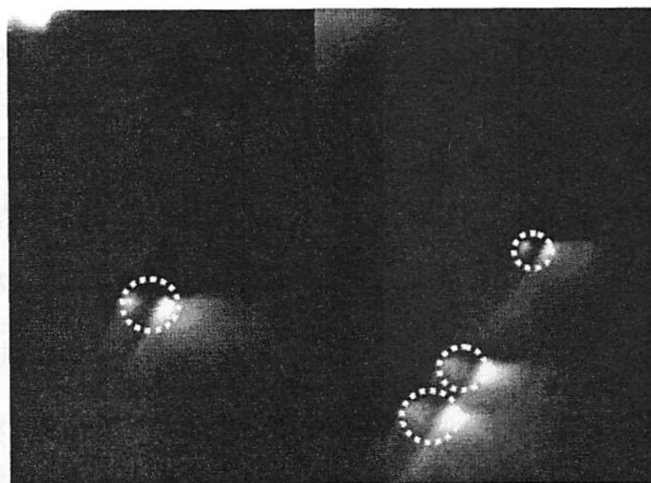

Figure 5.11: Influence of driving electric signal on droplet generation with 10μm nozzle. Left: single droplet formed at 8.5 V/4μs; right: multiple droplets formed at 7V/10μs.

Droplet generation behavior for larger nozzles (>4μm) is a little bit different. There is no obvious no-droplet-break-up stage; droplet formation is observed once the bubble formation voltage is reached. Increasing the electric pulse magnitude or pulse width can quickly increase the ejected droplet velocity and its volume. Higher heating conditions can cause multiple droplets, as shown in Figure 5.11.

We have plotted the initial bubble formation and heater breakdown conditions for an inkjet device with 30μm heater (Table 5.3) in Fig. 5.12, and marked the regions for single droplet generation with different nozzle dimensions. We can see that decreasing nozzle size shifts the inkjet operation window upwards and to the right, indicating that more heating energy (and hence stronger bubble actuation) is necessary to generate smaller droplets. The window size also becomes larger, indicating that satellite-free droplet formation can be more easily achieved for the micron scale nozzles. The observed maximum velocity of the 3μm scale droplet in the single droplet generation window is about 12m/s.

We have also observed changes in droplet generation behavior corresponding to heater size. Heaters ranging from 50, 40, 30 to 20μm (with chamber sizes of 100, 80, 60 and 60μm respectively) have been fabricated in our test chips. Larger heaters tend to form larger droplets at greater velocity, given identical driving pulse widths and thermal flux (power/area). However, the influence of heater size on droplet generation can be easily overpowered by slight changes in the heating signal. The heater size effect only becomes dominant when the heater dimension is reduced to 20μm. At this size, no droplet break-up has been observed for sub-2.5μm nozzles under any driving condition.

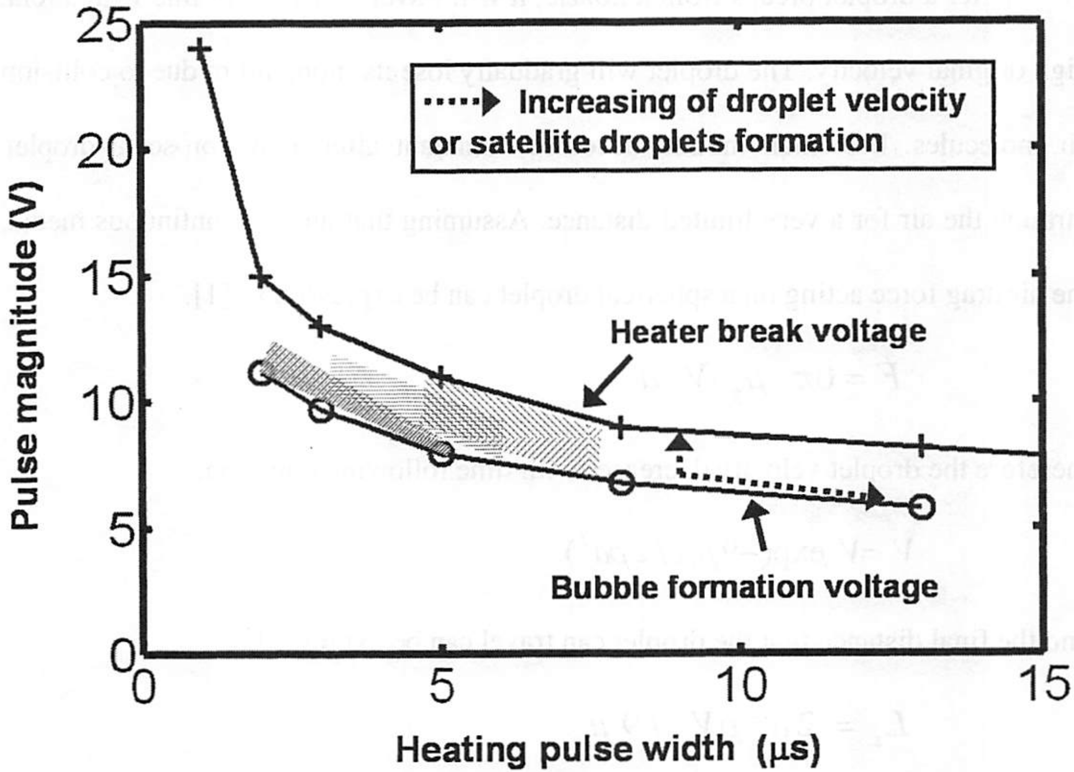

Single droplet generation window for 7μm nozzle

Single droplet generation window for 2.5 μm nozzle

Single droplet generation window for 1.5 μm nozzle

Figure 5.12: Single droplet generation window for 7μm, 2.5μm and 1.5μm nozzles with heater size of 30μm

5.3.3 Droplet velocity change and trajectory distribution

Reductions in droplet size are tremendously important in efforts to print high resolution patterns, but the challenge doesn't end there. The droplets must also have consistent volume and be delivered accurately to positions on a substrate. Experimental results show that our print head has excellent performance in droplet uniformity. Once the driving condition is fixed, the observed distribution of longitudinal droplet velocity varies by less than 5%, while droplet size change is not detectable.

After a droplet breaks from a nozzle, it will travel in a straight line with a relatively high original velocity. The droplet will gradually lose its momentum due to collision with air molecules. Brownian motion becomes dominant after a micron-scale droplet flies through the air for a very limited distance. Assuming that air is a continuous media, then the air drag force acting on a spherical droplet can be expressed as [1]:

$$F = 6\pi \cdot \mu_g \cdot V \cdot a \qquad [5.1]$$

therefore the droplet velocity decreases with time following equation:

$$V = V_o \exp(-9\mu_g t / 2\rho a^2) \qquad [5.2]$$

and the final distance that the droplet can travel can be expressed as:

$$L_s = 2a^2 \rho V_o / 9\mu_g \qquad [5.3]$$

where ρ is the liquid density, V_o and a are the initial droplet velocity and radius, respectively, and μ_g is the air viscosity coefficient. For a droplet with diameter of 3.5μm and initial velocity around 4m/s, theory predicts that a droplet will drop to half its initial velocity after 30μs, and effectively stop traveling after about 150μm. The results are quite close to our experimental observations (50μs and 300μm, as shown in Figure 5.13). The ultimate droplet flight distance and time (90% velocity reduction) for droplets with different dimensions and original velocity of 5m/s are calculated from equations 5.2 and 5.3 and listed in Table 5.5.

The misplacement of a droplet on a substrate can be attributed to two factors: the original droplet angular velocity distribution, and the random movement of the droplet due to collisions with air molecules. Setting certain delay times to the strobe trigger signal allows us to capture the trajectory distribution of ejected droplets at different flying

distances. As shown in Figure 5.13(a), when the droplet flight distance is short (<150μm with 50μs delay) and the droplet velocity is relatively high (>2m/s), the spread in droplet trajectory is much less than the size of a droplet. On a short time scale, the spreading should come from the original droplet angular velocity distribution, and the calculated spreading angle is smaller than 0.5°. However, as the droplet flying time increases and droplet approaches its stopping distance (~300μm), the droplet spread increases dramatically due to Brownian motion, as shown in Figure 5.13(b). The droplet position becomes totally random if the droplet flying time set to be larger than 500μs.

To achieve high pattern quality, we should keep the working distance between our print head and the substrate smaller than the droplet stopping distance, which, for the 2.8μm droplets, is only about 300μm, even with the highest achieved velocity (12m/s). Longer print-head-to-substrate distance is favorable considering substrate morphology and liquid evaporation (will be discussed in next section). Fortunately, the influence of air molecule collisions can be totally eliminated by operating the inkjet system in a low pressure environment, with much lower air molecule density. Under this condition, equation 5.3 predicts an infinitely long droplet flying distance, since air viscosity coefficient μ_g is proportional to the ambient pressure. However, once we consider the droplet angular velocity distribution (assuming 0.5° according to our experiment.), we must limit droplet flight distance to 1000μm to achieve good pattern quality with 3μm scale droplets.

Droplet size (μm)	10	4	3	2	1
Stopping distance (μm)	1600	260	147	65	16
Flying time (μs)	980	156	82	40	10

Table 5.5: Calculated droplet flying distance and time vs. droplet size

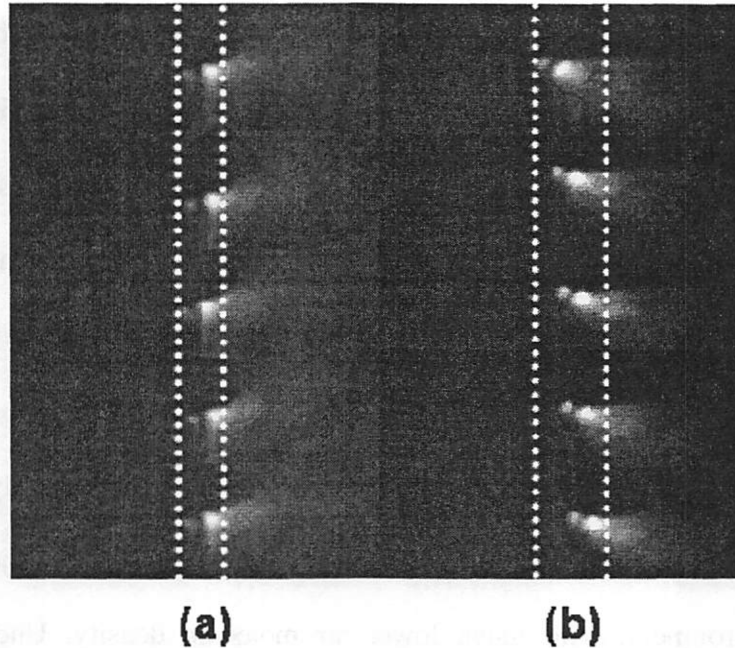

Figure 5.13: Droplets trajectory distribution of 3.5μm droplets at (a) delay time of 50μs, flight distance around 150μm and velocity about 2m/s; (b) delay time of 300μs, distance about 300μm and droplet velocity is almost zero.

5.3.4 Droplet volume change

The droplet volume also decreases before its hits the substrate, due to fluid evaporation. Maxwell laid the theoretical basis of droplet evaporation[2]: According to his study, the evaporate rate of a stationary droplet can be expressed as:

$$\frac{dr^2}{dt} = -\frac{2D}{\rho}(C_d - C_a) \qquad [5.5]$$

where r is the droplet radius, D is the diffusion constant of water vapor in air, C_d and C_a are the water vapor concentrations at the droplet surface and of the air. C_d will have an exponential relationship with the ambient temperature according to Clausius-Clapeyron equation. The lifetime of the droplet is then equal to:

$$t_{life} = \frac{\rho d_w^{\,2}}{8D(C_d - C_a)} \qquad [5.6]$$

which is proportional to the liquid droplet surface area. Here d_w is the droplet diameter.

The above equations do not consider the temperature change of the droplet due to evaporation, influence of the liquid surface tension force, non-continuity of the surrounding gas etc. G.A. Ferron et al. have given a simple mathematical equation to calculate the lifetime of a water droplet in consideration of all these corrections [3]. The total lifetime of a micro-scale water droplet can then be calculated as:

$$t_{life} = \frac{a \cdot d_w^{\,b} \exp(-k(T-20))}{(1-RH)} \qquad [5.7]$$

where a=6.74E8, b=1.97, k=0.0286 for temperature T between 0-60°C. RH is the relative humidity. This equation can calculate the droplet lifetime and the time scale for a water droplet to be reduced to half of its original size at room temperature; the results are listed in Table 5.6. Comparing the droplet evaporation time to the typical droplet traveling time in air (Table 5.5), we can see that the size reduction in a water droplet is negligible before it reaches the stopping distance. However, organic solvents such as methanol, acetone, and toluene etc., which are commonly used for nano-particle suspensions, have evaporation rates up to 10 times faster than water, due to higher saturated vapor

concentrations. Higher ambient temperatures can also achieve large evaporation rates. We could then use the evaporation phenomena in our favor to improve the inkjet device resolution. Chapter 7 will discuss this resolution enhancement technique in further detail.

D (um)	10	5	3	2	1
$t_{_life}$ (ms)	95	24	8.8	4	1
$t_{_half}$ (ms)	71	15.2	5.4	3	1

Table 5.6: Calculated water droplet lifetime in room temperature vs. droplet diameter

5.3.5 Frequency and power analysis

The frequency limit of our strobe light prevented our experimental setup from directly observing inkjet performance at frequencies higher than 150Hz. However, our inkjet devices should have maximum operation frequencies for stable droplet formation around 30 kHz, determined by the system cooling time (10-20μs), as discussed in section 3.2. Droplet formation time, chamber refilling time and meniscus damping are all negligible for micron scale droplets. Every firing cycle for 2.8μm droplet generation consumes about 10μJ of energy, calculated from the input heating signal from Figure 5.12. Energy can be saved by reducing heater size, pulse width, and also voltage drop in the interconnect wires (the test chips have interconnect resistances equal to the Pt heaters). Even considering this, energy consumption is limited to a minimum around 2-3μJ, due to the single droplet generation condition for the small nozzles. The maximum power consumption of the print head with 100,000 devices is then approximately 3000W

at a 10kHz operation frequency. Efficient substrate cooling is then essential to maintaining a constant print head temperature for stable droplet generation.

In summary, using a high resolution imaging system, we have observed test chips of our thermal bubble inkjet print heads generating water droplets down to 2.8μm. The droplet generation process is also found to be stable, uniform in droplet size and velocity, and free of satellite droplets. At small distances between the print head and substrate, droplet spread is also negligible. Our print head technology can thusly form the basis of a high resolution patterning system for building micro-scale electronic circuits and MEMS devices.

Even though this was not one of our original objectives, our experiment has achieved water droplet dimensions 5 times smaller than that produced by the most advanced inkjet cartridges (Table 1.1), and also smaller than the pixel size of a laser printer (10μm) and photographic images (6μm). The print head technology could then also be applied to commercial paper document printing market, where high-resolution inkjet printers are always in great demand.

Reference

1. F.G. Tseng, C.J. Kim, and C.M. Ho, "A high-resolution high-frequency monolithic top-shooting microejector free of satellite drops" Journal of Microelectromechan. Sys., vol.11, pp.427-447, 2002.

2. N.A. Fuchs, "Evaporation and droplet growth in gaseous media", Pergamon Press, 1959.

3. G.A. Ferron, S.C. Soderholm. "Estimation of the times for evaporation of pure water droplets and for stabilization of salt solution particles", *J. Areosol Sci.*,Vol. 21, pp415-429, 1990.

CHAPTER VI

TEST PRINTING OF NANO-PARTICLE BASED MATERIALS AND CARBON NANOTUBES

6.1 Material requirements

To build a maskless lithography system, we also need to find suitable materials that are both compatible with its print head and usable to form either functional device patterns or reliable mask layers for subsequent pattern-transferring processes.

Since our inkjet device uses a thermal bubble actuation mechanism, the fluid on the heater surface will be heated to a temperature higher than 200°C; the material of the choice should then be thermally stable, for continuous printing operation. Moreover, to achieve a high droplet resolution, the material should also have a high saturated vapor pressure, for strong bubble actuation strength, along with minimal surface tension and viscosity coefficient. Due to these restrictions, the typical polymer-based materials such as sol-gel, conductive polymers etc., commonly used for patterning optical devices [1] and organics circuits [2], are no longer applicable. Fortunately, another big category of materials, the nano-sized particles dispersed in solutions such as water and organic solvents, also known as nano-particle colloid inks, will not be limited by these constraints.

Particulate suspensions have many advantages as printing materials, including good chemical and thermal stability, adjustable particle concentration, and a wide choice of solutions. The suspended nano-particles could be selected for different properties, like conductivity (including Au or Ag particles [3, 4]), semi-conductivity (CdSe particles [5]), magnetism (Fe_3O_4 particles [6, 7]), etc, for various applications. Many groups have successfully demonstrated devices made of these materials.

In our research, suspensions of Au nano-particles and carbon nanotubes in aqueous solution have been test printed using our high resolution thermal bubble inkjet print head. Many pattern-formation-related issues have also been investigated. However, due to limited availability of the material and research time, no functional device has been built. We will discuss some of our preliminary experimental results in the following sections.

6.2 Inkjet printing of suspensions of Au nano-particles

6.2.1 Droplet generation

It is well known that monolayer-protected gold clusters can be uniformly dissolved into common solvents such as toluene, hexanes, and water [8, 9]. The size of the Au nano-particle can range between 1-20nm. Sintering the Au particles at temperatures between 150-400°C (depending on particle size) will form a low-resistance conducting layer.

In the course of our research, we obtained and tested a 2% (by weight) aqueous solution containing 10nm scale Au nano-particles (from Professor Paul Alivisatos's group) and a 10% propylbenzene solution containing Au nano-particles smaller than 5nm (from Professor Vivek Subramanian's group) (Figure 6.1 (a)&(b)). Both materials

undergo single droplet generation, as shown in Figure 6.1. Propylbenzene-based materials have heating voltages for droplet generation quite close to that of water, meaning that they have similar bubble nucleation temperatures, which is consistent with the result shown in Table 5.2. We choose nozzle sizes greater than 3µm and droplet dimensions between 4-5µm to print these materials, for better pattern quality.

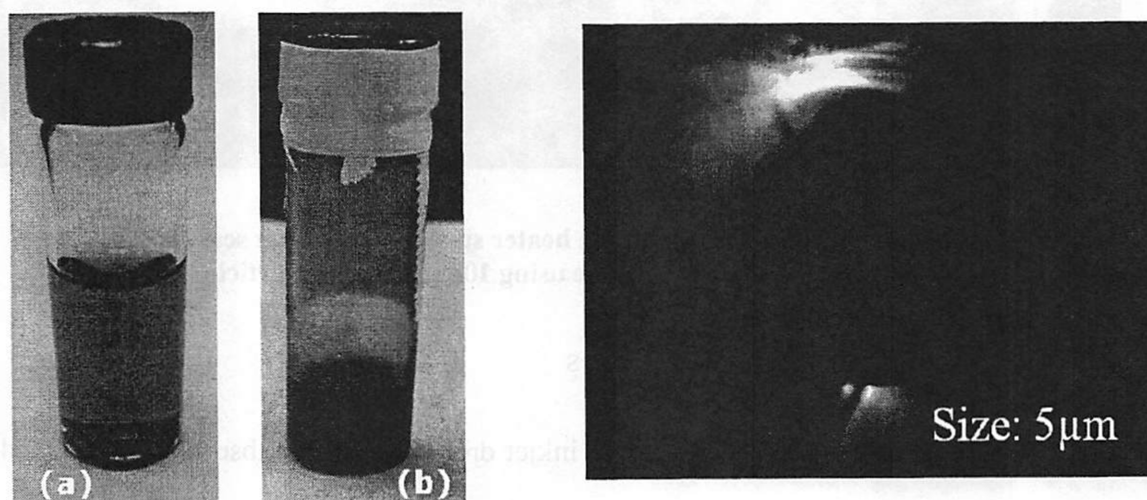

Figure 6.1: Left: (a) 2% 10nm scale Au nano-particles suspended in water; (b) 10% 5nm scale Au nano-particles in propylbenzene. Right: 5µm scale droplet generated with Au particle suspension in propylbenzene

Our experiments found that, at longer operation times, the 5nm-scale particle suspension tends to clog the nozzle. Optical observation of the heater surface reveals that the Au nano-particles accumulate on the heater surface (Figure 6.2(a)), probably due to the material's lower melting temperature, caused by its wide particle size distribution. On the other hand, the 10nm scale Au particles are very stable in droplet generation. The heater surface is clean under optical observation even when operated with a heating

frequency of 1kHz for hours, as shown in Figure 6.2(b). Our thermal bubble print head thus requires suspensions with relatively large (>5nm), uniform nano-particle sizes.

Figure 6.2: (a) Au accumulated on the heater surface using 5nm scale Au particle suspension; (b): clean heater surface using 10nm scale Au particle suspension

6.2.2 Inkjet printed Au dots and lines

Unlike printing on paper, where an inkjet droplet is totally absorbed by the media, in a maskless lithography system, a device pattern is formed by the interaction of a droplet with a substrate and the adjacent features. Achieving desired pattern geometry, then, requires a good understanding of droplet impact and interaction theory. To study pattern formation behavior of the nano-particle based material, we first printed the building blocks of a device pattern, simple Au dots and lines, by placing an oxide-coated silicon chip beneath the inkjet nozzle during droplet ejection. The small chip area allowed us to adjust the nozzle-to-substrate distance to as little as 150μm.

6.2.2.1 Inkjet printed Au dots

Printed Au dots are observed to form coffee-ring or donut structures, as shown in Figure 6.3. The shape can be explained by the droplet "splashing" behavior when it

impacts on a substrate. Since the droplet has a positive momentum, if its Weber number and Reynolds number are large, the fluid inertial overcomes liquid surface tension and viscosity force, driving the liquid outward, and leaving a thin liquid layer in the center, as illustrated in Figure 6.4(a). The solvent in the thin center region evaporates quickly, forming the donut structure. The printed Au dot has a footprint size around 15μm, about 3 times larger than the original droplet size (5μm), both due to the splashing effect and the small liquid-solid contact angle between water and the oxide. The outer ring of the dot is about 20nm thick; there are no Au nano-particles in the center of the ring, which can cause an un-even surface of the printed pattern.

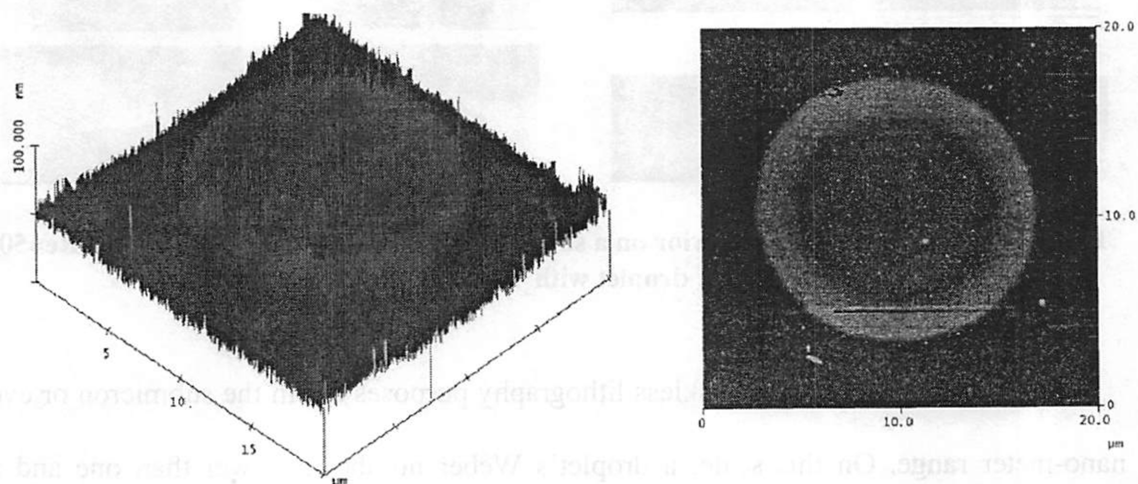

Figure 6.3: AFM image of a donut-shaped Au dot printed on oxide surface; the dot diameter is 15μm with original droplet size of 5μm

According to the study of Steven Molesa et al., heating the substrate could increase the evaporation rate of the solvent upon droplet deposition, therefore decreasing dot size and preventing the donut shape from forming [10], as shown in Figure 6.5. The droplet size in the picture is about 50μm. The splashing effect also becomes less dominant as the

droplets become smaller. According to the study of Schiaffino et al. [11], if the Weber number and Reynolds number of the droplet are relatively low, the unbalanced Young's force at the contact line instead of liquid inertia governs the droplet spreading on substrate. Droplets then form a simple cap shape on a substrate, as illustrated in picture 6.4(b), and their footprints are determined primarily by the liquid/solid contact angle.

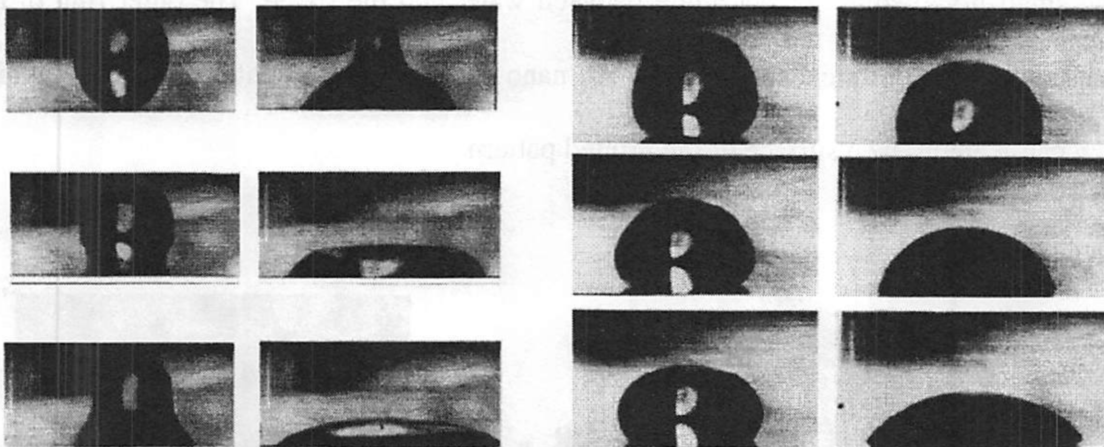

Figure 6.4: Droplet impact behavior on a substrate [11]. Left: droplet with We=3, Re=50, $\theta c=18^{o}$; right: droplet with We=0.33, Re=5, $\theta c=30^{o}$.

The target droplets for maskless lithography purposes are in the submicron or even nano-meter range. On this scale, a droplet's Weber number is lower than one and its Reynolds number is smaller than 10, so no splashing behavior will occur upon droplet deposition. The relationship between the droplet footage size and the liquid contact angle is then shown in Figure 6.6. We can see that if the liquid contact angle is between 20°-70°, which are typical values, the printed dot size is 2.5-1.5 times bigger than the original droplet size. Increasing the liquid contact angle on substrate could then increase the printed feature resolution.

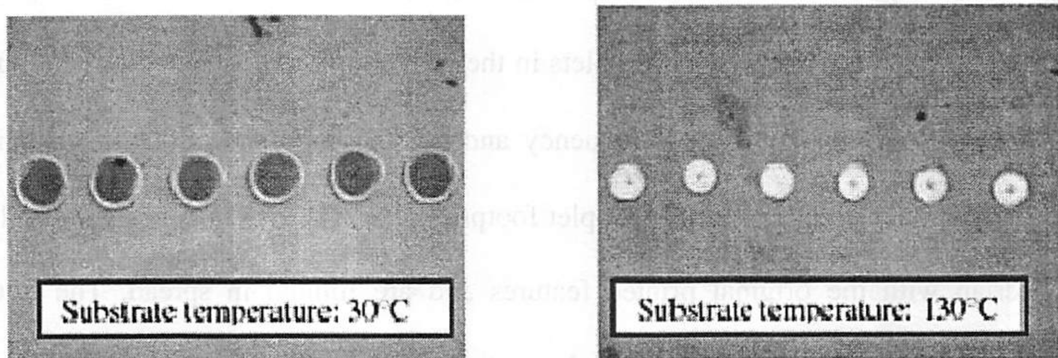

Figure 6.5: Heating up the substrate reduces printed dot size and prevent formation of donut shape [10].

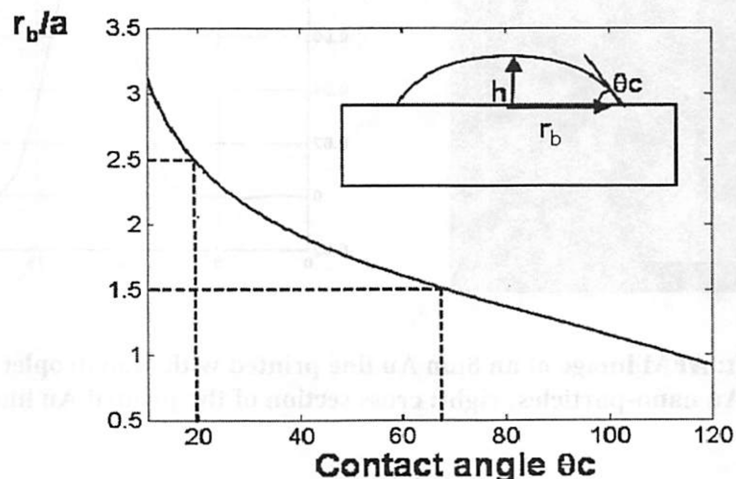

Figure 6.6: Ratio between the printed dot and original droplet size vs. liquid contact angle

6.2.2.2 Inkjet printed Au lines

By moving the oxide coated silicon chips with a simple translation stage, we also printed Au lines on the substrate. An AFM image of an 8μm Au line, formed with 4μm droplets, is shown in Figure 6.7(a). In this case, we maintained a nozzle-to-substrate distance around 200μm. The printed Au lines have a uniform size and smooth shape. The center region has a thickness of about 100nm, as shown in Figure 6.7(b). The donut

signature of a single dot is absent in the printed line, due to the interaction of the adjacent droplets. The step size between the droplets in the printed line is calculated to be around 1μm, from the droplet generation frequency and the moving speed of the translation stage. This is much smaller than the droplet footprint size. The newly deposited droplets thus overlap with the original printed features and are limited in spread. The liquid surface tension will pull the fluid and the Au particles to the center.

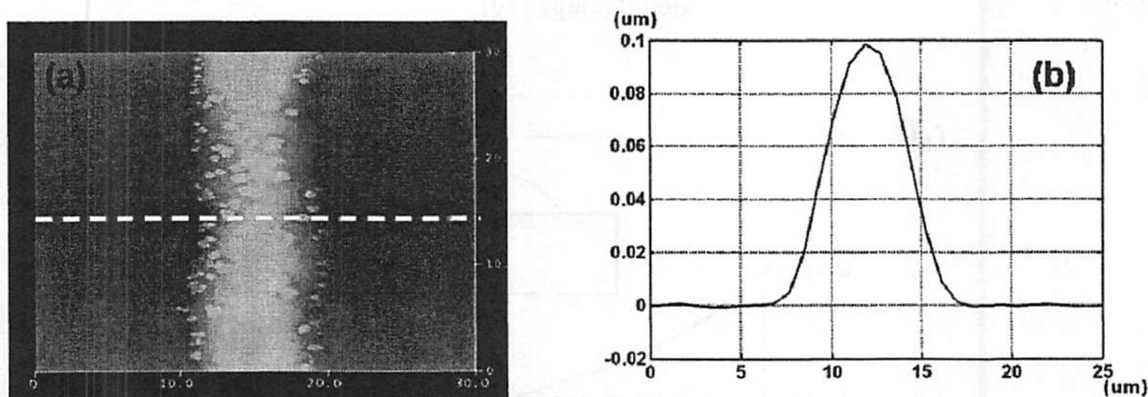

Figure 6.7: Left: AFM image of an 8μm Au line printed with 4μm droplet suspended with Au nano-particles; right: cross section of the printed Au line.

We have also examined the impact of the nozzle-to-substrate distance on the printing process. At longer distances, the wider droplet trajectory distribution, discussed in chapter 4.3.2, means that the printed line is wider. If the nozzle-to- substrate distance is kept longer than the droplet flying distance, the droplet's random walk in the horizontal direction completely blurs the line shape, as shown in Figure 6.8(b). We also increased the driving voltage of the inkjet device to achieve satellite droplet production. The very short flying distance of satellite droplets causes dots scattered on both sides of a printed Au line, even with small nozzle-to-substrate distances, as shown in Figure 6.8(c).

Therefore, improving the printed pattern quality for a maskless lithography system requires precise control of the heating conditions to ensure satellite-free droplet generation, and reductions in nozzle-to-substrate distance to minimize liquid spreading.

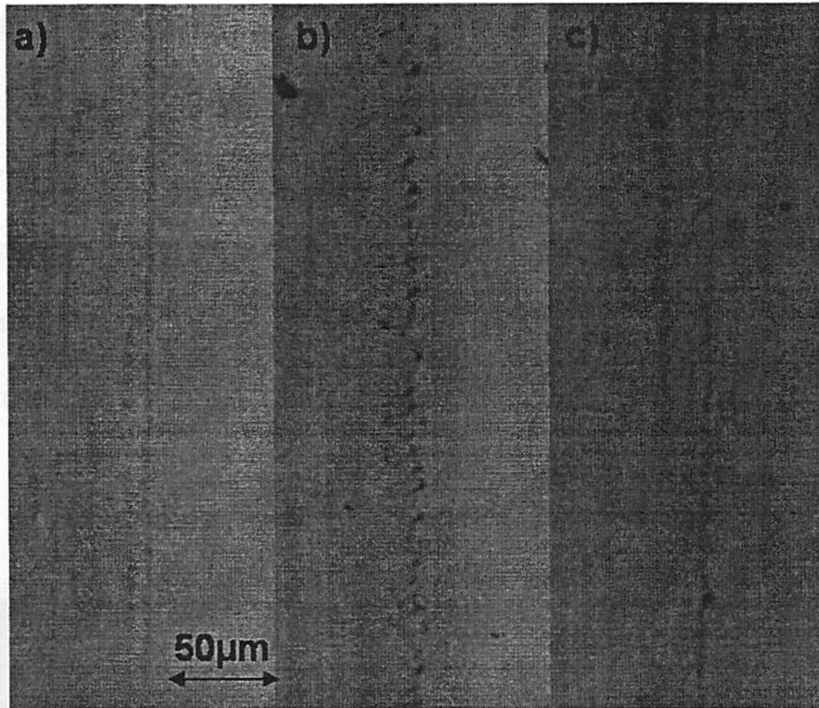

Figure 6.8: Au line printed with different operation conditions. (a) Single droplet generation with print head substrate distance<200μm; (b) Single droplet generation with print head substrate distance >400μm; (c) satellite droplet generation

6.2.3 Printing arbitrary patterns using an automatic printing system

To print more complicated patterns, we have installed our inkjet print head into an automatic patterning system, built by Professor Vivek Subramanian's group to print low cost organics circuits [10]. Their print heads, purchased from Microfab Inc., are piezoelectric-based devices and have a minimum printable droplet resolution of 30μm. The printing stage setup is shown in Figure 6.9(a). It consists of a print head mounted

above a translation stage with 1μm horizontal resolution and adjustable print head-to-substrate distance. The translation stage can hold a 4-inch wafer with a vacuum chuck and can be heated to a preset temperature. A simple piece of software allows us to define the device pattern from a computer. The computer controls the stage movement and generates electric pulses to trigger the DOD inkjet devices on the print head, thus forming the intended patterns. Figure 6.9(b) shows one of our test chip installed in the system and printing on a 4-inch wafer. The fluid delivering tubes and electrical input wires can also be seen in the picture. This system is actually a prototype of the maskless lithography system described in chapter I. Note that due to the large area of the chip and the ceramic package used for the electrical input, the minimum distance that can be achieved between the printhhead and substrate is larger than 0.4mm.

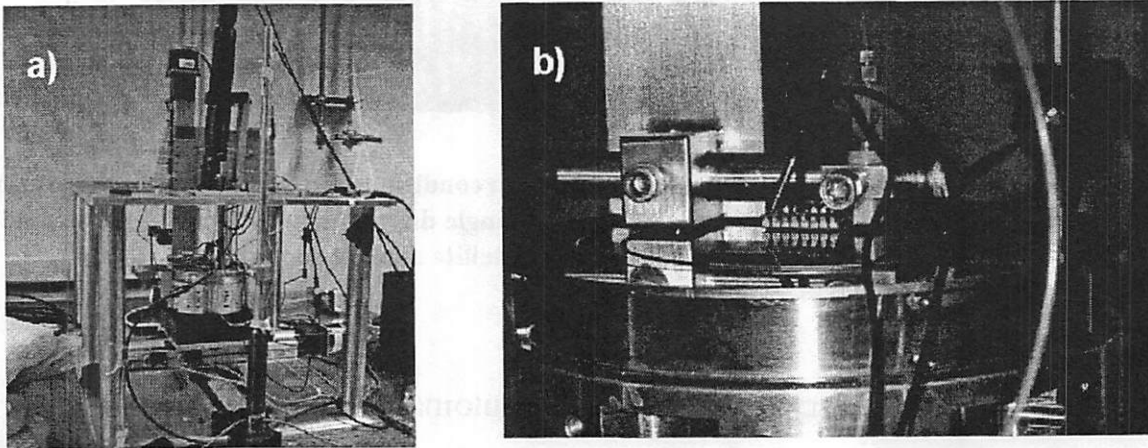

Figure 6.9: (a) The automatic patterning system set up; (b) a test chip mounted in the patterning system and printing on a wafer

Figure 6.9 shows arrays of Au lines and square pads printed on a silicon substrate by the patterning system. The space between the Au lines is 100μm and the adjacent

droplet distance in each line increases by 1μm from line to line. The Au pads are 100μm in dimension, with similar droplet distance increments. Cross sections of the printed lines and pads are also shown in Figure 6.10. The lines have a Gaussian shape when the droplet distance is 1μm, and become much thinner as the adjacent droplet distance increases. Printed line edges also become rougher with larger adjacent droplet distances, due to the round droplet footprint and its cross-sectional donut shape. Keeping the droplet distance (i.e. the pixel size) much smaller than the footprint size is then the key for inkjet printing methods to form smooth and uniform patterns for device fabrication. The Au pads have relatively rough surfaces. They average around 50nm in thickness when patterned with 1μm droplet distance. With larger droplet distances, they also begin to show their origins as arrays of dots, as illustrated in Figure 6.11. Generally, the printed Au line and pads have more irregular shapes than those in Figure 6.7, due to the limitation of print head-to-substrate distance in the printing system.

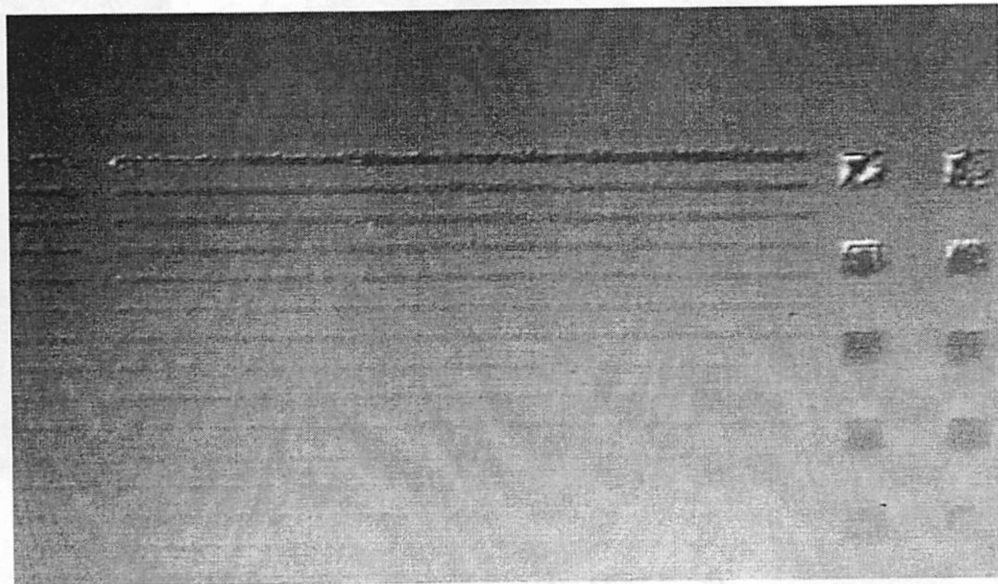

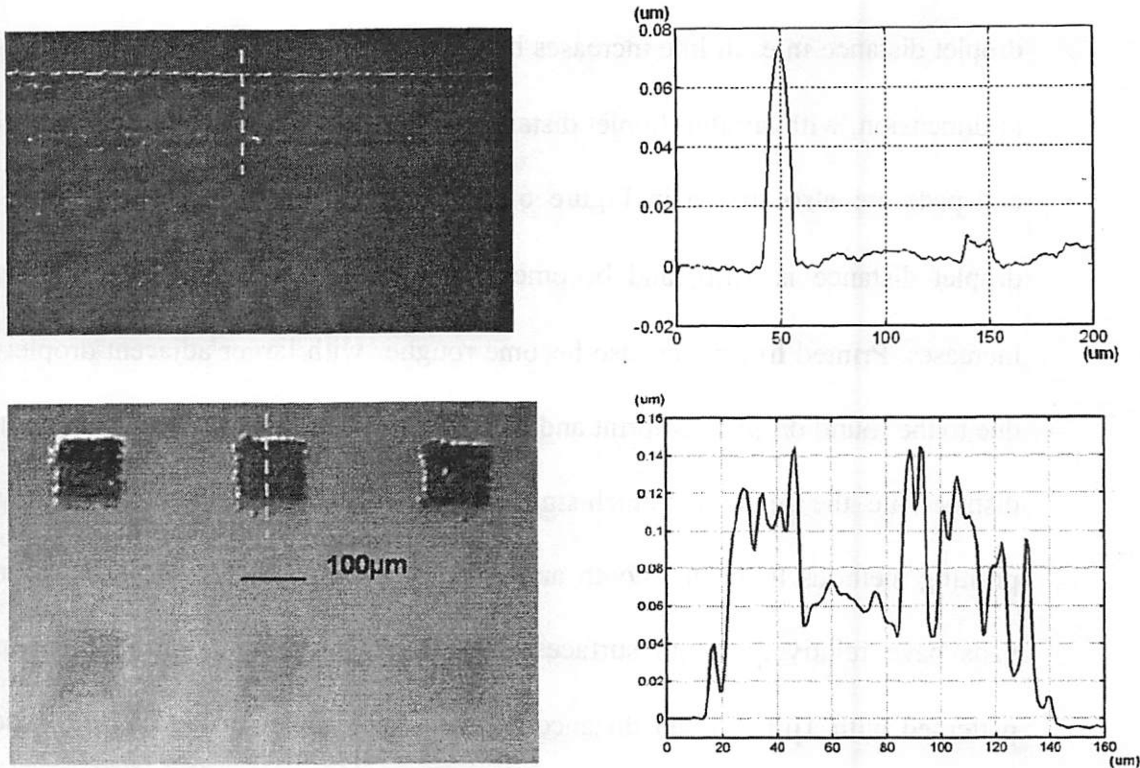

Figure 6.10: Lines and pads array printed with the automatic patterning system

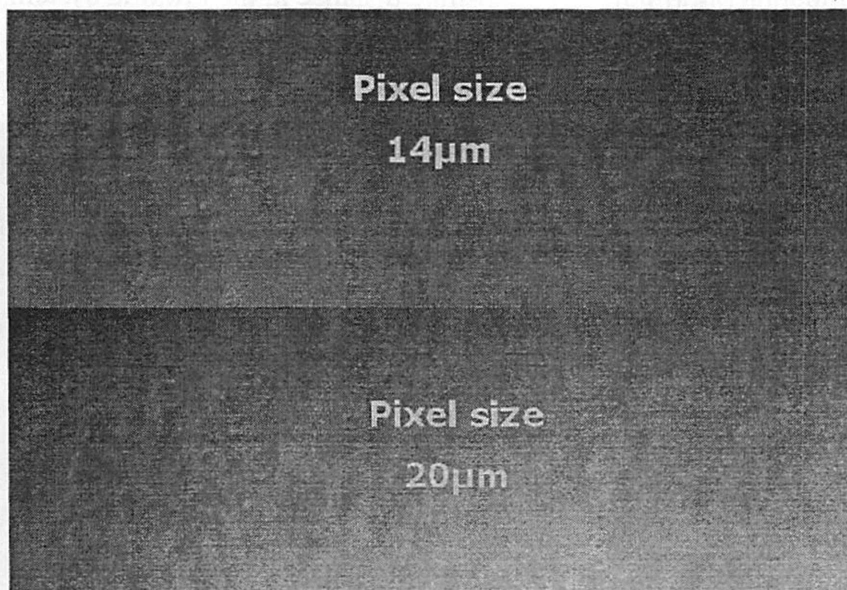

Figure 6.11: Dots array formed with large droplet distances

Using the prototype maskless patterning system to produce a test structure for resistance measurement, as illustrated in Figure 6.12, we can measure the conductivity of the printed Au layer. The Au pad and lines are formed with the smallest droplet distance (1μm) and double printing passes to increase the pattern thickness and uniformity. However, printed patterns still show very rough surfaces, and the pads are actually broken up in some regions. The patterns are sintered in high temperature oven for hours, and a probe station measures the Au layer resistance along the printed line. Not surprisingly, the measured resistance is always infinite, regardless of the sintering temperature (up to 350°C, quite enough for 10nm scale Au particles). Initially, we believed that it is a large fluid contact angle on the wafer that caused the uneven surface, since liquid surface tension tends to form round-shaped patterns and break lines into droplets, just as shown in the Figure 6.12(a). We then measured the contact angle of the printing material on the substrates, and found it to be smaller than 20°. Another explanation is that the Au particles in our material, which are wrapped by citrate to allow suspension in water [8], have a tendency to accumulate on the substrate, causing the rough pattern surface and a discontinuous film after solvent evaporation. However, special treatments of the substrate to prevent the accumulation behavior, such as O_2 plasma etching, failed to yield better results.

Even though the available Au nano-particle based material couldn't be directly used to form a conductive layer, the printed patterns can still be used as an etching mask to transfer the intended features to another layer beneath. We have etched an oxide chip printed with the 8μm Au lines using a fluoride based plasma etching system. After this process, the Au mask is stripped by gold etchant. Oxide lines with the same width as the

Au mask are formed on the substrate, as shown in Figure 6.13. The oxide line has a clean, flat surface in the center with thickness around 250nm. The original Au mask at the edge of the flat region is about 50nm thick (Figure 6.7(b)), so the selectivity between the Au nano-particle material and SiO_2 should be greater than 5.

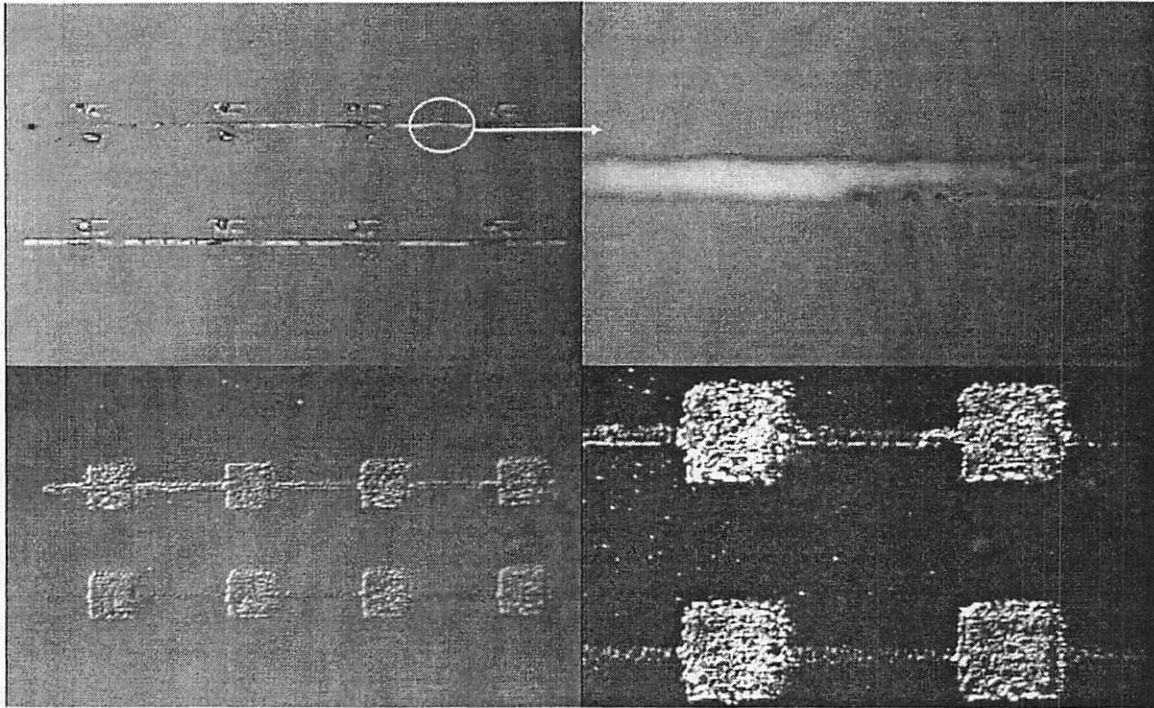

Figure 6.12: Inkjet printed resistance measurement patterns

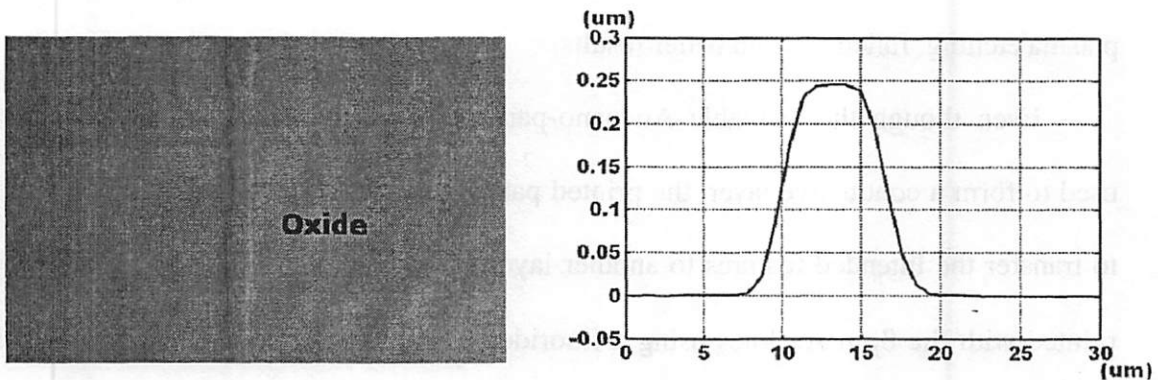

Figure 6.13: Oxide line etched using the inkjet printed pattern as mask

In summary, using Au nano-particle suspensions in our thermal bubble inkjet print head allowed us to investigate many pattern-formation-related issues for building an inkjet printing maskless lithography system. Au lines as small as 8μm have been printed, the smallest features ever reported by inkjet printing fabrication methods. The nano-particle-based material shows a good compatibility with our print head, even though more materials must still be tested to produce a functional device.

6.3 Direct deposition of carbon nano-tubes on pre-patterned electrodes

Over the past ten years, carbon nanotubes have been the focus of intense industrial and academic research, holding the promise of revolutionary applications in electronics, displays, chemical sensors, gas separation membranes, and structural materials [12]. For electronic applications, the cost-effective integration of carbon nanotubes with other circuit elements poses a significant challenge. While advances in on-wafer CVD growth of SWCNTs continue to be made, this approach is still largely incompatible with Si integrated circuit fabrication schemes, due to its high temperature requirements [13]. In comparison with in-situ CVD growth, inkjet printing methods can carry out post-growth assembly at room temperature, as a 'last-step' in an integrated circuit fabrication sequence.

Researchers in Sandia National Laboratories have demonstrated that wrapping SWCNT with ssDNA produces stable aqueous suspensions with high concentrations of individual nanotubes [14]. Using ssDNA-wrapped SWCNT suspensions in our thermal bubble inkjet printing system, we have successfully deposited SWCNT on silicon substrate at controlled locations, as shown in Figure 6.14(a), where a bundle of carbon nanotubes are placed between two pre-patterned electrodes, with the space of 1μm. The

droplets in this experiment are greater than 10μm in diameter, generated from 7μm nozzles, so the droplet footprint is about 30-50μm. The droplet footprint can be seen in the SEM picture in Figure 6.14(b) due to the presence of non-nanotube carbon debris in the solution. A higher density of carbon nanotubes exists on the edge of a droplet, due to the effects of droplet splashing. The typical nanotube length is between 1-3μm (Figure 6.14(c)). Single tubes and rope bundles of nanotubes are indistinguishable in the SEM pictures, so the nature of the deposits is unknown.

Even though the inkjet printing method cannot directly control the orientation of the carbon nanotubes, combining alternating current dielectrophoresis (ACDEP) method [15, 16] can polarize the carbon tubes and attract them to the high field region between the electrodes, as shown in Figure 6.15. Using inkjet deposition instead of directly dispensing solutions on the electrode provides a distinct advantage: by adjusting the density of the carbon nanotube suspension and reducing the droplet size, we can deliver a single nanotube to an electrode with each deposition cycle, preventing nanotube bundling during the alignment process. The inkjet dispensing method can also offer controlled positioning for other potentially useful nanostructures besides carbon nanotubes, such as silicon nanowires, CdSe nanorods etc. The inkjet printing method could then be a novel nano-device fabrication methodology without any process compatibility issues.

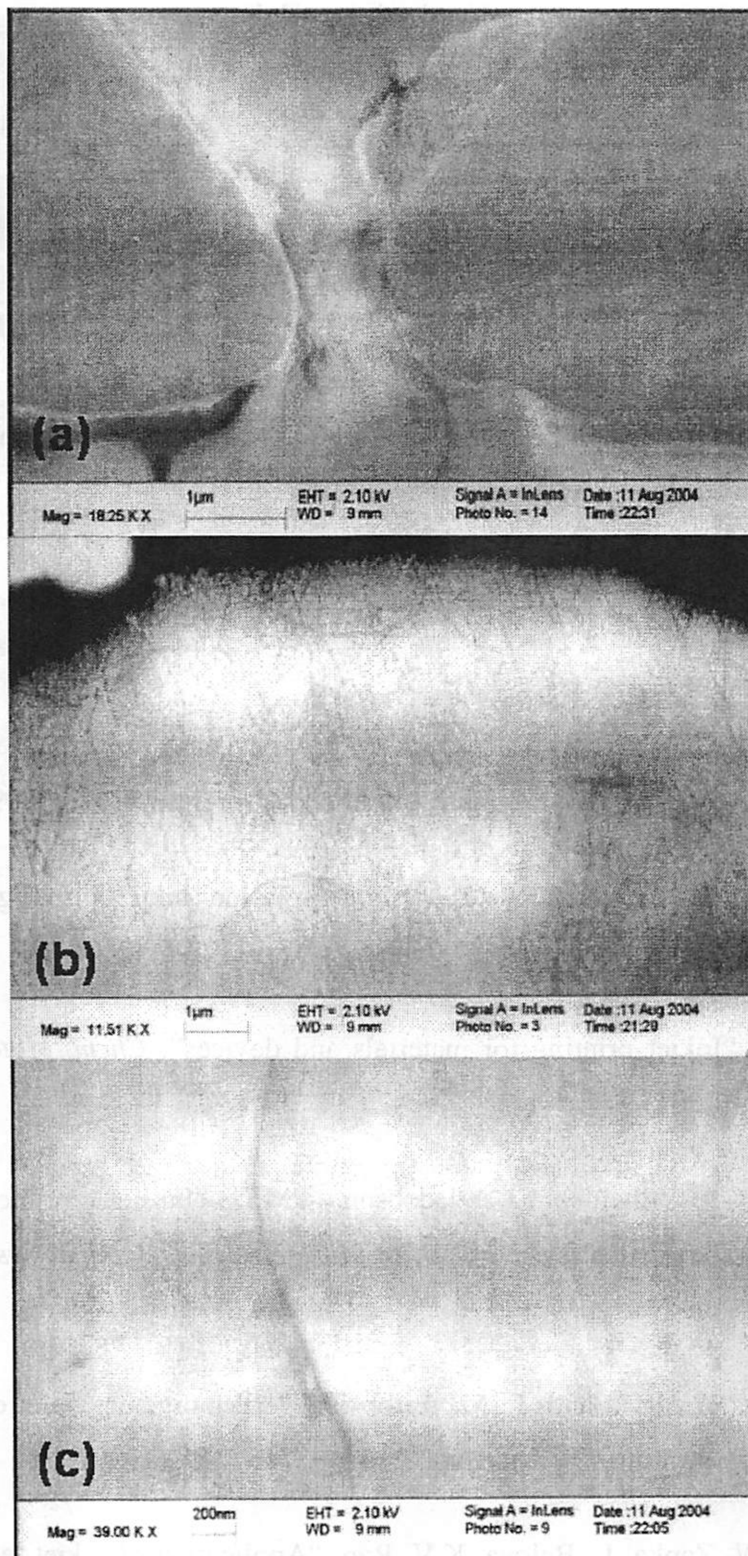

Figure 6.14: SEM pictures of (a) Carbon nanotubes printed between 2 electrodes with 1µm distance; (b) Carbon nanotubes inside a big droplet; (c) a single carbon nanotube on the substrate.

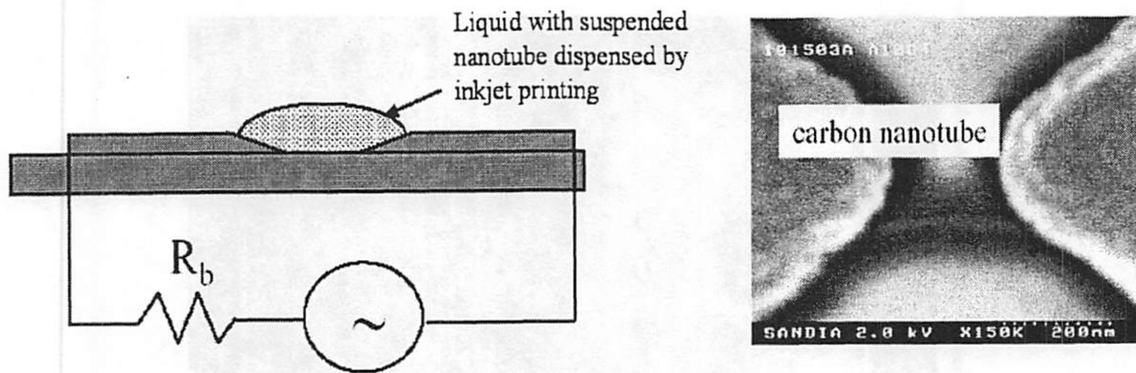

Figure 6.15: Possible nanotube alignment using inkjet printing deposition combined with alternating current dielectrophoresis method [14].

Reference

1. H. Klauk, B. D'Andrade, T. N. Jackson, "All-organic integrated emissive pixels", *IEEE 57th Annual Device Research Conference Digest,* pp.162, (1999)

2. Sirringhaus H., Kawase T. etc., "High-resolution inkjet printing of all-polymer transistor circuits", *Science*, vol.290, no.5499, pp.2123-6, (2000)

3. Calvert, P, "Inkjet printing for materials and devices", *Chem. Mater.,* Vol. 13, pp. 3299–3305, (2001)

4. Fuller SB, Wilhelm EJ, Jacobson JM., "Ink-jet printed nanoparticle microelectromechanical systems", *J. of Microelectromechanical Systems*, **11**, pp.54-60, (2002)

5. A. Ridley, B. Nivi, and J. M. Jacobson, "All-inorganic field effect transistors fabricated by printing," Science, vol. 286, pp. 746–749, (1999)

6. W. Voit, W. Zapka, L. Belova, K.V. Rao, "Application of inkjet technology for the deposition of magnetic nanoparticles to form micron-scale structures", *IEEE Proc. Sci. Meas. Technol.*, 150, pp.252-255, (2003)

7. H. Ago, K. Murata, M. Yumura, J. Yotani, S. Uemura, "Ink-jet printing of nanoparticle catalyst for site-selective carbon nanotube growth," *Appl. Phy. Lett.*, 82, pp.811-133, (2001)

8. M.C. Daniel and D. Astruc, "Gold Nanoparticles: Assembly, Supramolecular Chemistry, Quantum-Size-Related Properties, and Applications toward Biology, Catalysis and Nanotechnology", *Chem. Rev.* Vol. 104, 293-346, (2004)

9. Huang, F. Liao, S. Molesa, D. Redinger, V. Subramanian, "Plastic compatible low resistance printable gold nanoparticle conductors for flexible electronica", *Journal of The Electrochemical Society*, Vol. 150, ppG412-417, (2003)

10. S. Molesa, D. R. Redinger, D. C. Huang, V. Subramanian, "High-quality inkjet-printed multilevel interconnects and inductive components on plastic for ultra-low-cost RFID applications", *Mat. Res. Soc. Symp. Proc.* Vol. 769, H8.3.1-8.3.6, (2003)

11. S. Schiaffino. and A.A. Sonin, "Molten droplet deposition and solidification at low Weber numbers", *Phys. Fluids* , Vol. 9. PP3172-3187, (1997)

12. M. S. Dresselhaus and H. Dai, ""Carbon nanotubes: Continued innovations and ... "Recent advances in methods of forming carbon nanotubes", *MRS Bulletin,* 29, pp237 (2004)

13. Ural, Y. Li, and H. Dai, "Electric-field-aligned growth of single-walled carbon nanotubes on surfaces", *Appl., Phys. Lett.* 81, pp3463-6, (2002)

14. A. Talin, P. M. Dentinger, F. E. Jones, S. Pathak, L. Hunter, F. Léonard, and A. M. Morales. "Assembly and Electrical Characterization of DNA-Wrapped Carbon Nanotube Devices", *Journal of Vacuum Science & Technology B.* Vol.22, pp3107-3111, (2004)

15. J. Lewenstein, T. P. Burgin, A. Ribayrol, L. A. Nagahara, R. Tsui," Trapping and aligning carbon nanotubes via substrate geometry engineering", *Nano Lett.* Vol. 2, pp443 (2002)

16. P. A. Smith, C. D. Nordquist, T. N. Jackson, T. S. Mayer, B. R. Martin, J. Mbindyo, and T. E. Mallouk, ""Spontaneously organized molecular assemblies ", *Appl. Phys. Lett.* 77 1399 (2002)

CHAPTER VII

CONCLUSION

7.1 Summary

In this dissertation, we proposed a maskless lithography system that could additively form device patterns using small, inkjet-printed droplets of material, instead of expensive optics and masks. To meet the challenges of pattern resolution and printing throughput facing this micro-fabrication approach, we have focused our research on reducing the size of droplets produced by DOD inkjet devices and designing and fabricating a monolithic inkjet print head capable of accommodating a dense DOD device array. Our primary research achievements include:

1) We have studied the DOD inkjet device operation mechanism and investigated pressure conditions for micron to submicron scale droplets formation, using both scaling analysis and numerical simulation via commercial CFD software. Both methods show that the required droplet generation pressure scales inversely proportional to the nozzle dimensions. The pressure magnitude for 100nm droplet generation is found to be in 20MPa range.

2) We have studied various inkjet printing mechanisms, and chosen the thermal bubble inkjet device as the starting device to reduce droplet size, because of its high pressure and small device area. Numerical analysis shows that the droplet size limit of the

thermal bubble inkjet device is in the sub-micron scale. We have designed a robust, thermal bubble inkjet print head that could reach this resolution limit and maintain high operational frequencies and droplet generation stability, along with small device area and low energy consumption.

3) We have developed silicon micro-machining processes to fabricate the designed thermal bubble inkjet print head, including an original single-wafer process which forms the inkjet chambers and fluidic channels through a Ge sacrificial etching method; this fabrication process could form monolithic inkjet print heads with high device density and yield. Test chips with inkjet nozzles as small as 1.2μm in diameter have been fabricated by drilling with a focused ion beam system.

4) We have constructed a high resolution video image system to study the droplet generation process; droplets as small as 2.8μm have been observed from the test chips. The droplets are 5 times smaller than those produced by typical inkjet cartridges, and are the smallest that have ever been reported for compact inkjet printing devices. The droplet generation process is stable, with small droplet trajectory distribution at short droplet flying distances; we have also identified the single droplet formation window.

5) Gold nano-particles suspensions have been used as printing material. Au lines as small as 8um have been printed, the smallest features ever reported as fabricated by inkjet printing methods. Installing our print head into an automatic patterning system allowed us to investigate many pattern-formation related issues for building an inkjet printing maskless lithography system. Our print head also realizes direct deposition of Carbon nano-tubes.

7.2 Future research directions

7.2.1 Further reducing droplet size

Our experimental results indicate that our thermal bubble inkjet devices have a minimum droplet dimension of approximately 2.8μm, and a minimum pattern size around 5μm, through control of the substrate material and the liquid contact angle. This printing resolution would be sufficient for building low-cost organic transistor circuits (5-10μm channel length) for flat panel displays, electronic tags, etc., as well as for fabrication of MEMS structures. This new inkjet print head technology could also be applied to commercial inkjet printing industry, which is desperately seeking improved resolution for the fast-growing market of digital photographic image printing. However, our achieved droplet dimension is still one order of magnitude larger than the largest feature sizes found in today's semiconductor industry. To use the inkjet printing maskless lithography system for IC fabrication, further droplet size reduction approaches should be investigated. Based on our theoretical and experimental study, the following approaches seem most promising:

7.2.2: Building a piezoelectric actuation system

Piezoelectric inkjet print heads have better material compatibility than thermal bubble inkjet print heads, since they involve no high temperature process. Piezoelectric print heads also consume much less energy than thermal bubble heads, which is especially important in large device arrays. However, the difficulty in implementing a piezoelectric inkjet printing system for maskless lithography purposes lies in the fabrication of high quality piezoelectric thin films (less than 20μm thick) on a large area.

As we have discussed in chapter I, fulfilling the throughput requirements of maskless lithography applications demands a dense device array, and hence miniaturization of the inkjet device. This would require integrated fabrication of thin film piezoelectric actuators. Several piezoelectric thin film deposition methods such as sol-gel [1], CVD [2], pulsed laser ablation [3], sputtering [4], etc. have been reported. However, the deposited thin film material typically has unstable film properties [5, 6], and their piezoelectric constants are much smaller than their bulk counterparts. The life cycle of a typical piezoelectric thin film, which is in the range of 1e6 firings, is also too low for production-level applications. These are the reasons we chose not to design our inkjet print head based on piezoelectric actuation mechanism in the first place. However, once a reliable technology to fabricate piezoelectric thin films is available, the piezoelectric-based inkjet system would be able to achieve droplet resolutions in the sub-micron scale, according to our theoretical analysis of pressure and timing conditions for droplet generation in chapter II. The details will be discussed below.

The typical piezoelectric inkjet device utilizes either bending of a piezoelectric bi-membrane (d_{31} mode) structure or extension of a piezoelectric disc (d_{33} mode) for actuation. In our research, the material constants of thin film $Pb(Zr_xTi_{1-x})O_3$ (PZT, with piezoelectric constants of d_{31}=50pm/V, and d_{33}=100pm/V [5]) are used to estimate the performance of the PZT actuators. When estimating fluid pressure that can be generated from volume change of a piezoelectric actuator, the typical approach treats the liquid as an incompressible media, and calculates the pressure magnitude that can cause the same amount of liquid to move through an inkjet nozzle or a fluid channel [7, 8]. This approach, however, will not be feasible for designing a high resolution inkjet device,

because with the high pressure magnitudes (MPa) and the short time scale (ns range), compressibility of the fluid needs to be considered. Therefore, we used the formula of shock wave pressure generated from a piston movement [9, 10],

$$P(t) = \rho \cdot c \cdot V(t) \qquad [7.1]$$

to calculate the acoustic pressure magnitude in the fluid due to the actuator movement. Here, ρ is the fluid density, c is the sound wave speed in the fluid, and V(t) is the average velocity of the actuator. The true pressure field should be a solution to the wave equations inside the inkjet chamber, considering all the boundary conditions. This formula is just a rough scaling estimation with the assumption that a plane wave is generated in a DOD inkjet device.

For a round-shaped bi-membrane PZT actuator with PZT film thickness of t_p ($h=2*t_p$) and radius of r, as shown in Figure 7.1 (this bimorph design gives the maximum PZT displacement), we can treat it as a spring system with a spring constant [11, 12]:

$$k_{eff} = \frac{12\pi \cdot D}{\ln 2^2 r^2} \text{ , and } D = \frac{E \cdot h^3}{12(1-\nu^2)} \qquad [7.2]$$

where E is the Young's modules of the membrane, and v is Poisson ratio. The coupled liquid system can be taken as a media with damping coefficient:

$$b = \frac{\pi \cdot r^2 \cdot \rho \cdot c}{2} \qquad [7.3]$$

and the piezoelectric actuation force is:

$$F = \frac{2\pi \cdot M}{2\ln 2} \text{ , and } M = d_{31} \cdot E_{11} \cdot E_{max} \cdot t_p{}^2 \qquad [7.4]$$

where E_{max} is the maximum allowed electric field for piezoelectric response of the thin film PZT material, typically around 150kV/cm [5]. The movement of the membrane can then be calculated from equation:

$$m\ddot{x} + b\dot{x} + k_{eff}x = F \qquad [7.5]$$

Our numerical simulations show that thick membranes with higher spring constants grant the system fast response speeds, and hence shorter pressure pulse widths. However, rigid membranes also have smaller displacements under their maximum stress conditions. Decreasing the membrane area will also increase response speed at the expense of displacement. By combining different membrane radii and thicknesses, we estimate that the maximum acoustic pressure magnitude that such a piezoelectric bi-membrane actuator can generate is in 0.6MPa range. A 2μm scale water droplet could then be ejected according to table 2.2. The simulated volume displacement and pressure pulse shape of a PZT bi-membrane actuator with radius of 30μm and thickness of 4μm, driven with a 1e-7s long square-shaped electric signal, is shown in Figure 7.2. Unlike that generated by a thermal bubble inkjet device, the pressure pulse has a dual-polarized shape and its width can be optimized to realize the predicted droplet size.

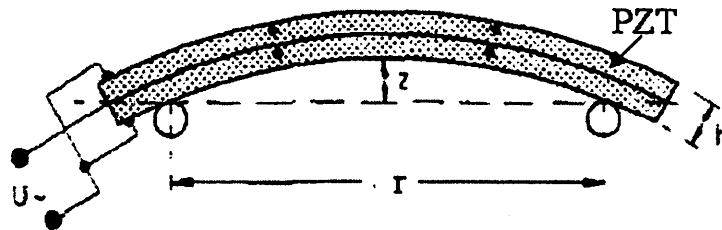

Figure 7.1: Schematics of a bimorph piezoelectric actuator [11]

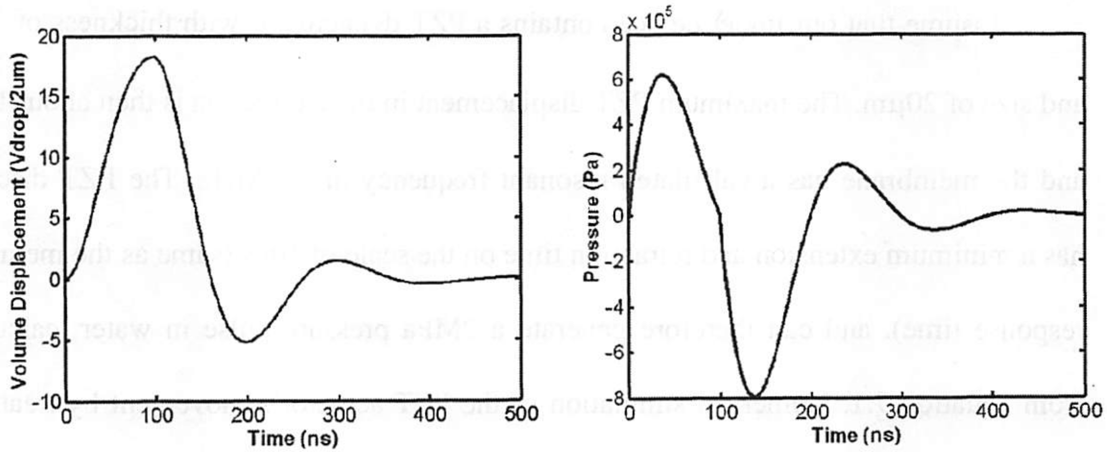

Figure 7.2: The simulated volume displacement and pressure pulse shape of a PZT bi-membrane actuator with radius of 30μm and thickness of 4μm. The input electric signal is 0.1μs long with a square shape

A higher actuation pressure, and hence better droplet resolution, may be achieved using a d_{33} mode PZT actuator. The schematic of such an actuator is shown in Figure 7.3. Its maximum DC displacement in the z direction can be expressed as: $\delta = d_{33} \cdot E_{\max} \cdot t$, while the resonant frequency of the PZT disk with one end attached to the substrate is equal to $f_r = \frac{N}{2t}$, where N is the frequency constant of the PZT material and generally about 2000Hz.m. The maximum PZT actuation velocity, which is on the scale of $2 \cdot f_r \cdot \delta$ (the factor 2 comes from PZT overshoot when applying an electric pulse), is decoupled from the dimensions of the actuator, and can be expressed as: $V_{\max} = d_{33} \cdot E_{\max} \cdot N$.

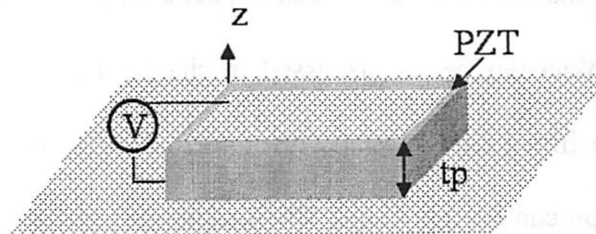

Figure 7.3: Schematics of a d33 mode piezoelectric actuator

Assume that our inkjet device contains a PZT d_{33} actuator with thickness of 10μm and size of 20μm. The maximum PZT displacement in the z direction is then about 15nm, and the membrane has a calculated resonant frequency of 100MHz. The PZT disc then has a minimum extension and retraction time on the scale of 10ns (same as the membrane response time), and can therefore generate a 2MPa pressure pulse in water, calculated from equation 7.1. Numerical simulation of the PZT actuator's movement by treating it as a spring system confirms this analysis, as shown in Figure 7.4. The device could then eject a water droplet around 1μm from a nozzle, according to table 2.2. The volume change of the actuator is about 35 times of the targeted droplet volume, which is necessary due to the compressibility of the fluid. I also want to give an estimation of the blocking pressure P_b of the device, which is the pressure magnitude that would push back the actuator movement caused by the piezoelectric effect. Its value can be easily calculated from equation: $P_b = d_{33} \cdot E_{max} / S_{33}$, and estimated to be in 40MPa range. Some publications use this value as the maximum fluid pressure available from the PZT actuator, but it is difficult to obtain inside an inkjet chamber, due to the acoustic nature of the pressure pulse.

The calculations above use water as the printing media. Typical solvents of nano-particle suspensions, such as methanol and toluene, have surface tension coefficients about one half of that of water, so we can expect a 0.5μm-scale droplet resolution for the d_{33} mode PZT inkjet device, as discussed in chapter II. Even smaller droplet sizes are possible if a thin film PZT material with a piezoelectric constant higher than the value used in calculation can be fabricated. The droplet dimensions may be further reduced if liquid evaporation is considered.

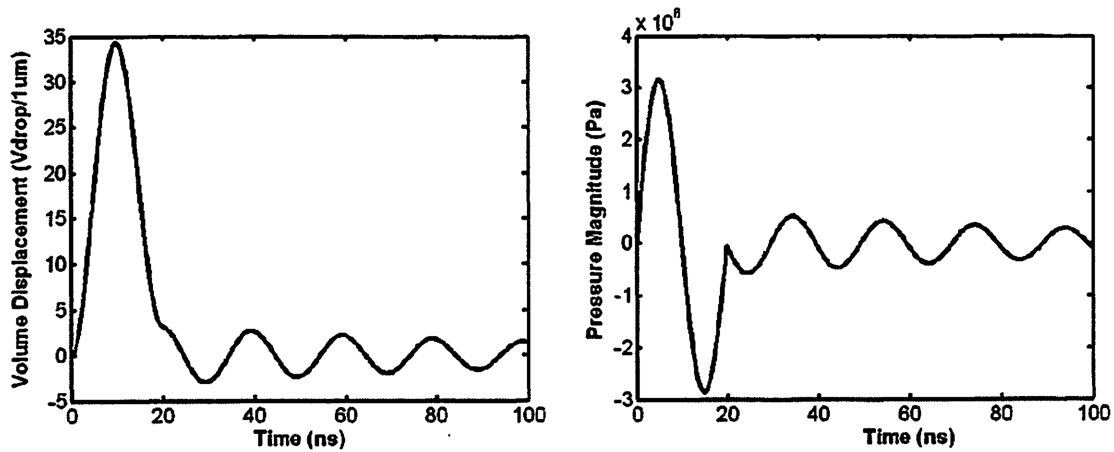

Figure 7.4: The simulated volume displacement and pressure pulse shape of a PZT d_{33} mode actuator with radius of 20μm and thickness of 10μm. The input electric signal is 20ns long with a square shape.

7.2.3: Utilize liquid evaporation

As discussed in section 5.3, the printed droplet dimensions can be reduced by liquid evaporation. However, the droplet positions become totally random before significant droplet size reduction can be observed due to air molecule collisions. Installing the inkjet printing system into a vacuum environment, therefore minimizing these collisions, could help to increase the droplet flying time before significant droplet trajectory deviation occurs. The droplet evaporation rate also depends strongly on the material and the ambient temperature. According to the Maxwell's equation, the droplet evaporation rate is proportional to the saturated vapor concentration of the fluid at the droplet surface, which increases exponentially with the ambient temperature. At temperatures around 80°C, the water droplets can evaporate 20 times more quickly than in room temperature, as shown in Figure 7.5. Moreover, organic solvents, such as acetone and toluene (toluene is a common solvent for particulate suspensions), have evaporation rates 10 to 20 times greater than water's, as shown in Table 7.1. Therefore, through appropriate solvent

choices, increases in ambient temperature and reductions in ambient pressure, droplet could shrink significantly before hitting a substrate.

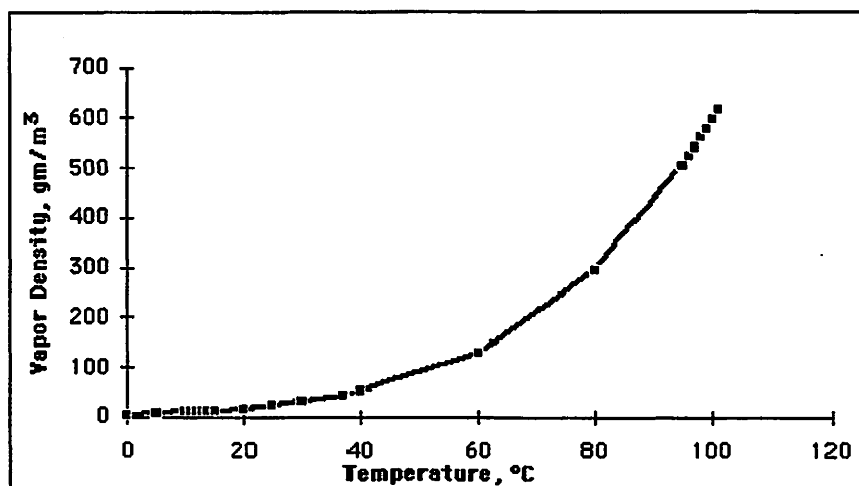

Figure 7.5: Water vapor density vs. ambient temperature

Material	Water	Acetone	Toluene	Hexane
Relative evaporation rate	0.3	5.3	2.4	8.3

Table 7.1: Relative evaporation rate of typical organic solvents and water [13]

However, concerns of the printed pattern quality will still limit the practical ratio of droplet size reduction by liquid evaporation. If the droplet is reduced to, say, ¼ of its original diameter, then its volume reduction is cubed, and is 1/64 in this case. Small variances of the original droplet volume caused by heating history, nucleation probability, or un-damped liquid oscillation etc. could result in large differences in the final droplet dimension, causing poor uniformity of printed pattern size. Our experiments

have already shown the sensitivity of droplet size to different heating conditions for a thermal bubble inkjet device, as discussed in section 5.3.

Moreover, according to the Maxwell's equation, the droplet evaporation rate is inversely proportional to its radius. Since droplet size changes quickly at the final droplet evaporation stage, minimizing the final CD variance requires precise control of liquid evaporation time. However, the ejected droplet velocity distribution makes this a difficult task. If we target to reduce the droplet size to ¼ of its original radius, then with a 5% change in droplet velocity (which has been observed in our research), the final droplets could vary in size between 1/3 and 1/10 of the original droplet radius.

In addition, decreasing droplet sizes requires tighter bounds of displacement errors on a substrate. Even though the droplet random walk can be totally eliminated by operating the inkjet device in a vacuum environment, imperfect nozzle shapes still cause some variation in droplet angular velocity. At finite droplet flying distances, this could result in deviations of droplet trajectory comparable or even bigger than the targeted droplet size. Because of all the above issues, the practical ratio of droplet size reduction by liquid evaporation method will be determined by the droplet generation stability and could be in 1/2 to 1/4 range.

In conclusion, a sub-micron to deep sub-micron scale inkjet patterning system could feasibly be created by developing a high performance PZT inkjet print head and installing the printing system into a vacuum environment to take advantage of liquid evaporation. Such a maskless lithography system could be a valuable tool to replace the high cost optical lithography systems, hence reducing the expense of semiconductor chips

fabrication and building original devices using various fluid materials for display, imaging, sensor and actuator applications.

Reference

1. S.K. Dey, K.D. Budd and D.A. Payne "Thin film ferroelectrics of PZT by sol-gel processing", *IEEE Trans.* Vol. 35 , pp80–1, 1988

2. B.S. Kwak, E.P. Boyd and A. Erbil, "MOCVD of PbTiO3thin films", *Appl. Phys. Lett.* Vol. 53, pp1702–4, 1988

3. S.B. Krupanidhi, "RF planar magnetron sputtering and characterization of ferroelectric PZT films", *J. Appl. Phys.* Vol. 54. pp6601–9, 1983

4. S. Otsubo, "Preparation of PZT films by laser ablation" *Japan. J. Appl. Phys.* Vol. 29 ppL133–6, 1990

5. P. Muralt, "Ferroelectric thin films for micro-sensors and actuators: a review", *J. Micromech. Microeng.* Vol. 10, pp136–146, 2000

6. L. Tsakalakosa and T. Sands, "Epitaxial ferroelectric ÑPb,LaÖÑZr, TiÖO3 thin films on stainless steel by excimer laser liftoff", *Appl. Phys. Lett.*, Vol. 76. pp227, 2000

7. Van Lintel HTG, Van De Pol FCM, Bouwstra S. "A piezoelectric micropump based on micromachining of silicon", *Sensors & Actuators A,* vol.15, no.2, Oct. 1988, pp.153-67. Switzerland

8. E. L. Kyser, L. F. Collins, and N. Herbert, "Design of impulse ink jet", *Journal of Applied Photographic Engineering*, Vol. 7, pp73-79, 1981

9. M. Makiguchi, H. Kawada, "An experimental study on shock waves in liquid", *JSME*, Vol. 20, pp57-62, 1977

10. I.I. Glass, L.E. Heukroth, "Hydrodynamic Shock Tube", *The Physc. Fluids*, Vol. 6, pp543, 1963

11. J.G. Smits, S.I. Dalke, T.K. Cooney, "The constituent equations of piezoelectric bimorphs", *Sensors & Actuators A*, Vol. 28, pp 41, 1991

12. P. Muralt, A. Kholkin et al, "Piezoelectric actuation of PZT thin film diaphragms at static and resonant conditions", *Sensors and Actuators A*, Vol. 53, pp398-404, 1996

13. Online material safety data sheet (MSDS)